

Gaia Focused Product Release: A catalogue of sources around quasars to search for strongly lensed quasars.

Gaia Collaboration, A. Krone-Martins^{1,2}, C. Ducourant³, L. Galluccio⁴, L. Delchambre⁵, I. Oreshina-Slezak⁴, R. Teixeira⁶, J. Braine³, J.-F. Le Campion³, F. Mignard⁴, W. Roux⁷, A. Blazere⁸, L. Pegoraro⁷, A.G.A. Brown⁹, A. Vallenari¹⁰, T. Prusti¹¹, J.H.J. de Bruijne¹¹, F. Arenou¹², C. Babusiaux¹³, A. Barbier⁷, M. Biermann¹⁴, O.L. Creevey⁴, D.W. Evans¹⁵, L. Eyer¹⁶, R. Guerra¹⁷, A. Hutton¹⁸, C. Jordi^{19,20,21}, S.A. Klioner²², U. Lammers¹⁷, L. Lindegren²³, X. Luri^{19,20,21}, S. Randich²⁴, P. Sartoretti¹², R. Smiljanic²⁵, P. Tanga⁴, N.A. Walton¹⁵, C.A.L. Bailer-Jones²⁶, U. Bastian¹⁴, M. Cropper²⁷, R. Drimmel²⁸, D. Katz¹², C. Soubiran³, F. van Leeuwen¹⁵, M. Audard^{16,29}, J. Bakker¹⁷, R. Blomme³⁰, J. Castañeda^{31,19,21}, F. De Angeli¹⁵, C. Fabricius^{21,19,20}, M. Fouesneau²⁶, Y. Frémat³⁰, A. Guerrier⁷, E. Masana^{21,19,20}, R. Messineo³², C. Nicolas⁷, K. Nienartowicz^{33,29}, F. Pailler⁷, P. Panuzzo¹², F. Riclet⁷, G.M. Seabroke²⁷, R. Sordo¹⁰, F. Thévenin⁴, G. Gracia-Abril^{34,14}, J. Portell^{19,20,21}, D. Teyssier³⁵, M. Altmann^{14,36}, K. Benson²⁷, J. Berthier³⁷, P.W. Burgess¹⁵, D. Busonero²⁸, G. Busso¹⁵, H. Cánovas³⁵, B. Carry⁴, N. Cheek³⁸, G. Clementini³⁹, Y. Damerdjji^{5,40}, M. Davidson⁴¹, P. de Teodoro¹⁷, A. Dell’Oro²⁴, E. Fraile Garcia⁴², D. Garabato⁴³, P. García-Lario¹⁷, N. Garralda Torres⁴⁴, P. Gavras⁴², R. Haigron¹², N.C. Hambly⁴¹, D.L. Harrison^{15,45}, D. Hatzidimitriou⁴⁶, J. Hernández¹⁷, S.T. Hodgkin¹⁵, B. Holl^{16,29}, S. Jamal²⁶, S. Jordan¹⁴, A.C. Lanzafame^{47,48}, W. Löffler¹⁴, A. Lorca¹⁸, O. Marchal⁴⁹, P.M. Marrese^{50,51}, A. Moitinho², K. Muinonen^{52,53}, M. Nuñez Campos¹⁸, P. Osborne¹⁵, E. Pancino^{24,51}, T. Pauwels³⁰, A. Recio-Blanco⁴, M. Riello¹⁵, L. Rimoldini²⁹, A.C. Robin⁵⁴, T. Roegiers⁵⁵, L.M. Sarro⁵⁶, M. Schultheis⁴, C. Siopis⁵⁷, M. Smith²⁷, A. Sozzetti²⁸, E. Utrilla¹⁸, M. van Leeuwen¹⁵, K. Weingrill⁵⁸, U. Abbas²⁸, P. Abraham^{59,60}, A. Abreu Aramburu⁴⁴, C. Aerts^{61,62,26}, G. Altavilla^{50,51}, M.A. Álvarez⁴³, J. Alves⁶³, R.I. Anderson⁶⁴, T. Antoja^{19,20,21}, D. Baines⁶⁵, S.G. Baker²⁷, Z. Balog^{14,26}, C. Barache³⁶, D. Barbato^{16,28}, M. Barros⁶⁶, M.A. Barstow⁶⁷, S. Bartolomé^{21,19,20}, D. Bashi^{68,69}, N. Bauchet¹², N. Baudeau⁷⁰, U. Becciani⁴⁷, L.R. Bedin¹⁰, I. Bellas-Velidis⁷¹, M. Bellazzini³⁹, W. Beordo^{28,72}, A. Berihuete⁷³, M. Bernet^{19,20,21}, C. Bertolotto³², S. Bertone²⁸, L. Bianchi⁷⁴, A. Binnenfeld⁷⁵, T. Boch⁴⁹, A. Bombrun⁷⁶, S. Bouquillon^{36,77}, A. Bragaglia³⁹, L. Bramante³², E. Breedt¹⁵, A. Bressan⁷⁸, N. Brouillet³, E. Brugaletta⁴⁷, B. Bucciarelli^{28,72}, A.G. Butkevich²⁸, R. Buzzi²⁸, E. Caffau¹², R. Cancelliere⁷⁹, S. Cannizzo⁸⁰, R. Carballo⁸¹, T. Carlucci³⁶, M.I. Carnerero²⁸, J.M. Carrasco^{21,19,20}, J. Carretero^{82,83}, S. Carton⁸⁰, L. Casamiquela^{3,12}, M. Castellani⁵⁰, A. Castro-Ginard⁹, V. Cesare⁴⁷, P. Charlot³, L. Chemin⁸⁴, V. Chiaramida³², A. Chiavassa⁴, N. Chornay^{15,29}, R. Collins⁴¹, G. Contursi⁴, W.J. Cooper^{85,28}, T. Cornez⁸⁰, M. Crosta^{28,86}, C. Crowley⁷⁶, C. Dafonte⁴³, P. de Laverny⁴, F. De Luise⁸⁷, R. De March³², R. de Souza⁶, A. de Torres⁷⁶, E.F. del Peloso¹⁴, M. Delbo⁴, A. Delgado⁴², T.E. Dharmawardena²⁶, S. Diakite⁸⁸, C. Diener¹⁵, E. Distefano⁴⁷, C. Dolding²⁷, K. Dsilva⁵⁷, J. Durán⁴², H. Enke⁵⁸, P. Esquej⁴², C. Fabre⁸, M. Fabrizio^{50,51}, S. Faigler⁶⁸, M. Fatović⁸⁹, G. Fedorets^{52,90}, J. Fernández-Hernández⁴², P. Fernique⁴⁹, F. Figueras^{19,20,21}, Y. Fournier⁵⁸, C. Fournon⁷⁰, M. Gai²⁸, M. Galinier⁴, A. Garcia-Gutierrez^{21,19,20}, M. García-Torres⁹¹, A. Garofalo³⁹, E. Gerlach²², R. Geyer²², P. Giacobbe²⁸, G. Gilmore^{15,92}, S. Girona⁹³, G. Giuffrida⁵⁰, R. Gomel⁶⁸, A. Gomez⁴³, J. González-Núñez⁹⁴, I. González-Santamaría⁴³, E. Gosset^{5,95}, M. Granvik^{52,96}, V. Gregori Barrera^{21,19,20}, R. Gutiérrez-Sánchez³⁵, M. Haywood¹², A. Helmer⁸⁰, A. Helmi⁹⁷, K. Henares⁶⁵, S.L. Hidalgo^{98,99}, T. Hilger²², D. Hobbs²³, C. Hottier¹², H.E. Huckle²⁷, M. Jabłońska^{100,101}, F. Jansen¹⁰², Ó. Jiménez-Arranz^{19,20,21}, J. Juaristi Campillo¹⁴, S. Khanna^{28,97}, G. Kordopatis⁴, Á. Kóspál^{59,26,60}, Z. Kostrzewa-Rutkowska⁹, M. Kun⁵⁹, S. Lambert³⁶, A.F. Lanza⁴⁷, Y. Lebreton^{103,104}, T. Lebzelter⁶³, S. Leccia¹⁰⁵, I. Lecoeur-Taibi²⁹, G. Lecoutre⁵⁴, S. Liao^{106,28,107}, L. Liberato^{4,108}, E. Licata²⁸, H.E.P. Lindstrøm^{28,109,110}, T.A. Lister¹¹¹, E. Livanou⁴⁶, A. Lobel³⁰, C. Loup⁴⁹, L. Mahy³⁰, R.G. Mann⁴¹, M. Manteiga¹¹², J.M. Marchant¹¹³, M. Marconi¹⁰⁵, D. Marín Pina^{19,20,21}, S. Marinoni^{50,51}, D.J. Marshall¹¹⁴, J. Martín Lozano³⁸, J.M. Martín-Fleitas¹⁸, G. Marton⁵⁹, N. Mary⁸⁰, A. Masip^{21,19,20}, D. Massari³⁹, A. Mastrobuono-Battisti¹², T. Mazeh⁶⁸, P.J. McMillan²³, J. Meichsner²², S. Messina⁴⁷, D. Michalik¹¹, N.R. Millar¹⁵, A. Mints⁵⁸, D. Molina^{20,19,21}, R. Molinaro¹⁰⁵, L. Molnár^{59,115,60}, G. Monari⁴⁹, M. Monguió^{19,20,21}, P. Montegriffo

arXiv:2310.06295v1 [astro-ph.GA] 10 Oct 2023

³⁹, A. Montero³⁸, R. Mor^{116,20,21}, A. Mora¹⁸, R. Morbidelli²⁸, T. Morel⁵, D. Morris⁴¹, N. Mowlavi¹⁶,
 D. Munoz⁸⁰, T. Muraveva³⁹, C.P. Murphy¹⁷, I. Musella¹⁰⁵, Z. Nagy⁵⁹, S. Nieto⁴², L. Noval⁸⁰, A. Ogden¹⁵,
 C. Ordenovic⁴, C. Pagani¹¹⁷, I. Pagano⁴⁷, L. Palaversa⁸⁹, P.A. Palicio⁴, L. Pallas-Quintela⁴³, A. Panahi⁶⁸,
 C. Panem⁷, S. Payne-Wardenaar¹⁴, A. Penttilä⁵², P. Pesciullesi⁴², A.M. Piersimoni⁸⁷, M. Pinamonti²⁸,
 F.-X. Pineau⁴⁹, E. Plachy^{59,115,60}, G. Plum¹², E. Poggio^{4,28}, D. Pourbaix[†]^{57,95}, A. Prša¹¹⁸, L. Pulone⁵⁰,
 E. Racero^{38,119}, M. Rainer^{24,120}, C.M. Raiteri²⁸, P. Ramos^{121,19,21}, M. Ramos-Lerate³⁵, M.
 Ratajczak¹⁰⁰, P. Re Fiorentin²⁸, S. Regibo⁶¹, C. Reylé⁵⁴, V. Ripepi¹⁰⁵, A. Riva²⁸, H.-W. Rix²⁶, G.
 Rixon¹⁵, N. Robichon¹², C. Robin⁸⁰, M. Romero-Gómez^{19,20,21}, N. Rowell⁴¹, F. Royer¹², D. Ruz
 Mieres¹⁵, K.A. Rybicki¹²², G. Sadowski⁵⁷, A. Sáez Núñez^{21,19,20}, A. Sagristà Sellés¹⁴, J. Sahlmann⁴²,
 V. Sanchez Gimenez^{21,19,20}, N. Sanna²⁴, R. Santoveña⁴³, M. Sarasso²⁸, C. Sarrate Riera^{31,19,21}, E.
 Sciacca⁴⁷, J.C. Segovia³⁸, D. Ségransan¹⁶, S. Shahaf¹²², A. Siebert^{49,123}, L. Siltala⁵², E. Slezak⁴, R.L.
 Smart^{28,85}, O.N. Snaith^{12,124}, E. Solano¹²⁵, F. Solitro³², D. Souami^{103,126}, J. Souchay³⁶, L. Spina¹⁰, E.
 Spitoni^{4,127}, F. Spoto¹²⁸, L.A. Squillante³², I.A. Steele¹¹³, H. Steidelmüller²², J. Surdej⁵, L. Szabados⁵⁹,
 F. Taris³⁶, M.B. Taylor¹²⁹, K. Tisanić⁸⁹, L. Tolomei³², F. Torra^{31,19,21}, G. Torralba Elipe^{43,130,131},
 M. Trabucchi^{132,16}, M. Tsantaki²⁴, A. Ulla^{133,134}, N. Unger¹⁶, O. Vanel¹², A. Vecchiato²⁸, D.
 Vicente⁹³, S. Voutsinas⁴¹, M. Weiler^{21,19,20}, Ł. Wyrzykowski¹⁰⁰, H. Zhao^{4,135}, J. Zorec¹³⁶, T. Zwitter¹³⁷,
 L. Balaguer-Núñez^{21,19,20}, N. Leclerc¹², S. Morgenthaler¹³⁸, G. Robert⁸⁰, and S. Zucker⁷⁵

(Affiliations can be found after the references)

Received 23 June 2023 / Accepted 09 October 2023

ABSTRACT

Context. Strongly lensed quasars are fundamental sources for cosmology. The *Gaia* space mission covers the entire sky with the unprecedented resolution of 0.18" in the optical, making it an ideal instrument to search for gravitational lenses down to the limiting magnitude of 21. Nevertheless, the previous *Gaia* Data Releases are known to be incomplete for small angular separations such as those expected for most lenses.

Aims. We present the Data Processing and Analysis Consortium GravLens pipeline, which was built to analyse all *Gaia* detections around quasars and to cluster them into sources, thus producing a catalogue of secondary sources around each quasar. We analysed the resulting catalogue to produce scores that indicate source configurations that are compatible with strongly lensed quasars.

Methods. GravLens uses the DBSCAN unsupervised clustering algorithm to detect sources around quasars. The resulting catalogue of multiplets is then analysed with several methods to identify potential gravitational lenses. We developed and applied an outlier scoring method, a comparison between the average BP and RP spectra of the components, and we also used an extremely randomised tree algorithm. These methods produce scores to identify the most probable configurations and to establish a list of lens candidates.

Results. We analysed the environment of 3 760 032 quasars. A total of 4 760 920 sources, including the quasars, were found within 6" of the quasar positions. This list is given in the *Gaia* archive. In 87% of cases, the quasar remains a single source, and in 501 385 cases neighbouring sources were detected. We propose a list of 381 lensed candidates, of which we identified 49 as the most promising. Beyond these candidates, the associate tables in this Focused Product Release allow the entire community to explore the unique *Gaia* data for strong lensing studies further.

Key words. gravitational lensing: strong, quasars: general, methods: data analysis, catalogues, surveys

1. Introduction

An extensive census of quasars (QSOs) is fundamental to many cosmological studies. Specifically, in cases where these quasars exhibit multiple images, strongly lensed quasars enable the estimation of the Hubble constant H_0 directly from time delay measurements (e.g. Refsdal 1964; Courbin et al. 2005; Millon et al. 2020; Suyu et al. 2017; Chen et al. 2019; Wong et al. 2020). In addition to many other astrophysical and cosmological applications, these sources are also used for detailed studies of dark matter halos and their substructures (e.g. Nierenberg et al. 2017; Li et al. 2017; Diaz Rivero et al. 2018; Gilman et al. 2020b; Nierenberg et al. 2020; Gilman et al. 2020a, 2021; Minor et al. 2021), and for constraining the dark energy equation of state (e.g. Linder 2004, 2011; Oguri et al. 2012; Xia et al. 2017; Liu et al. 2019; Wang et al. 2022). All lensed quasars discussed in this work are strongly lensed by definition.

Detecting lenses has been historically challenging because (i) most lensed quasars are distant and hence faint and (ii) broad sky coverage and high angular resolution are required as the angular separations between the lensed images are small. More-

over, chance projection can create astrometric configurations and even broad-band photometry similar to those expected from lensed quasars such that a reliable confirmation requires spectroscopic measurements of the quasar images and the lensing galaxy. Due to these difficulties, the number of confirmed lensed quasars has been low for decades. The ESA/*Gaia* mission (Gaia Collaboration et al. 2016) and its data releases, particularly since Data Release 2 (Gaia Collaboration et al. 2018, 2021, 2023b), have been dramatically improving this situation.

Although *Gaia* was primarily designed to study the Milky Way through astrometry at the micro-arcsecond level, it produces an all-sky survey including millions of galaxies and QSOs (Robin et al. 2012; Krone-Martins et al. 2013; de Souza et al. 2014; de Bruijne et al. 2015; Gaia Collaboration et al. 2023a; Ducourant et al. 2023; Krone-Martins et al. 2022). In their work, de Souza et al. (2014) and de Bruijne et al. (2015) define downlink criteria. The sources can be used to create a homogeneous, magnitude-limited survey of lensed quasars down to image separations of $\sim 0.18''$. This is comparable to the angular resolution of the NASA/ESA Hubble Space Telescope, but *Gaia* measurements have all-sky coverage. During this decade,

the recently launched ESA/NASA Euclid space mission (Lau-reijs et al. 2011) will also be surveying $\sim 14\,000$ square degrees at comparable angular resolutions, providing deep and high-resolution images in multiple bands for the first time at such large scales (Euclid Collaboration et al. 2022). This is expected to revolutionise strong lensing studies by enabling almost direct confirmation of thousands of lensed quasars (e.g. Treu et al. 2022), and complementing *Gaia*'s μas astrometry with deep and precise photometry.

Conservative estimates of the number of lensed QSOs detectable by *Gaia* in standard ΛCDM (Λ cold dark matter) cosmology ($\Lambda = 0.7$, $\Omega_m = 0.3$) suggest that $\sim 3\,000$ multiply imaged QSOs could be detected by *Gaia* of which > 250 would have ≥ 3 images and the rest doubles (Surdej et al. 2002; Finet & Surdej 2016). *Gaia* could then lead to a ten-fold increase in the number of lensed QSOs resulting in a homogeneous survey providing precise astrometry for all lensed images. Such a census is being built by the astronomical community, which continuously scans the *Gaia* data releases for follow-up spectroscopic confirmation (e.g. Krone-Martins et al. 2018; Ducourant et al. 2018; Agnello et al. 2018; Lemon et al. 2018; Delchambre et al. 2019; Krone-Martins et al. 2019; Lemon et al. 2019; Stern et al. 2021; Lemon et al. 2023; Desira et al. 2022). This endeavour is already resulting in a unique and statistically significant sample of lenses that will be used to study the evolution of the population of the deflecting galaxies and to constrain cosmological parameters, including the value of H_0 that is currently under significant tension (e.g. Verde et al. 2019; Di Valentino et al. 2021).

Current *Gaia* Data Releases are still incomplete at the lowest angular separations (e.g. Arenou et al. 2017, 2018; Fabricius et al. 2021; Torra et al. 2021), as expected for early mission products. This has led some known lensed images to lack *Gaia* counterparts (see, e.g. Ducourant et al. 2018). And this has slowed the identification of new lenses since most lensed QSOs that have yet to be discovered are probably angularly small. Thus, within the *Gaia* Data Processing and Analysis Consortium, we developed a dedicated processing chain to analyse the environment of quasars and produce a catalogue of sources and clusters, including new lens candidates for further studies and confirmation by the community. The major goals of this work are to make this focused *Gaia* data available to the community, to present the new data, and to call the attention of the community to the possibility of using this data to study currently known lensed quasars and to discover new lensed quasars while also providing a first, non-exhaustive, candidate list.

Finally, new astrophysical cases can emerge from the large lens samples expected. For instance, because the quasar is unique and point-like, but the images are seen through different parts of the lensing object, we can use the colors and magnitudes to study the obscuring dust in the line of sight. Cosmic dust reddens light but not always in the same way. Let A_v designate the V band absorption and $B - V$ the color of an object. When there is reddening, we define the excess $B - V$ as $E(B - V) = (B - V) - (B - V)_0$ where $(B - V)_0$ is the intrinsic color of the object. Milky Way dust shows a pattern where $A_v \approx 3.1E(B - V)$ but the dust absorption spectrum is not identical for all galaxies (e.g. Gordon et al. 2003). *Gaia* provides much of this information, so using a large sample, as should come out of this work, we can reconstruct and study dust at cosmological distances via the $A_v/E(B - V)$ ratio, possibly inferring the existence of major dust features in the Universe (e.g. as done in Lallement et al. 2018; Green et al. 2019; Leike et al. 2021, 2022, for features in our galaxy), a new method to the best of our knowledge.

This paper is organized as follows. Sect. 2 presents the list of quasars and quasar candidates used as inputs to GravLens. Sect. 3 describes how the GravLens algorithm clusters transits (individual detections) mapping transits to sources along with some remaining issues. Sect. 4 describes the resulting catalog, the field contents, and the new sources. Afterward, in Sect. 5, we present the methods developed to create lens scores and a list of candidates. Finally, we present our conclusions in Sect. 6.

2. The list of quasars

Our processing starts from an input list of quasars. Since gravitational lenses are rare, with less than ~ 80 lensed quasars with 4 images –*quads* hereafter– known today (Stern et al. 2021), we want to make this input list of quasars for the GravLens processing as complete as possible to maximise our chances of detecting new lenses. Therefore we tolerate moderate stellar or galaxy contamination in this input list.

We merged some major catalogues of quasars and candidate AGNs published before 2022. These include the data releases 6.4, 7.0, 7.1b, 7.4c, 7.5, 7.5b of the Milliquas catalogue (Flesch 2021, 2019), the R90 and C75 selections of the AllWISE catalogue (Assef et al. 2018), the catalogue of AGN candidates from (Shu et al. 2019), a selection of sources from Klioner et al. 2021 (private communication), a subset of the *Gaia* DR3 quasar_candidates table (Gaia Collaboration et al. 2023a), and additional quasars whose morphology was analysed by Ducourant et al. (2023). Most of these catalogues contain stellar contaminants.

The catalogues were cross-matched using a search radius of $3''$ and we only kept a single entry. The data priority follows the order listed above such that if a source is found in Milliquas 7.4c and 7.1b, only Milliquas 7.4c will be recorded. The compilation contains ~ 24 million total sources, of which ~ 5 million are matched to a *Gaia* DR3 source.

Sources that are clearly stellar were eliminated by applying a weak astrometric filter rejecting proper motions larger than 14 mas/yr or parallaxes larger than 6 mas. This filter was derived from the astrometric properties of the multiply imaged quasars by gravitational lensing (Ducourant et al. 2018) and is intentionally not severe because most quasars are in the faint luminosity regime of *Gaia* where the astrometry is less accurate and the potential presence of a surrounding host galaxy can perturb the astrometry of the central nucleus. We also filtered out objects brighter than $G = 14$ magnitudes and excluded sources with colours compatible with stellar sources: $(G_{\text{BP}} - G) > 1$ & $(G - G_{\text{RP}}) > 0.8$ & $G < 20$ (see Gaia Collaboration et al. 2023a, Fig. 37). We thus discarded $\sim 21\,000$ sources judged stellar. The small number of discarded sources indicates that possibly some sort of astrometric filtering had already been performed in the construction of the original catalogues. Finally, sources in the direction of the Magellanic clouds, of other large galaxies, or of major globular clusters (Harris 2010) were removed.

The final list of quasars and candidates contains 3 760 480 sources with an entry in *Gaia* DR3 and we refer to the list as the quasars or the quasar catalogue. The original catalogue name (e.g. Milliquas 7.4c) for each source is stored in `lens_catalogue_name`.

The sky distribution of the quasars in our input list is shown in Fig. 1 in galactic coordinates. The sky coverage of each of the merged catalogues is heterogeneous, as is the resulting compiled list. Most (81%) of the sources have a G magnitude fainter than 19.5 mag, as seen in Fig. 2. Fig. 2 also shows the *Gaia* colour $G_{\text{BP}} - G_{\text{RP}}$, the W1-W2 colour from catWISE (Eisenhardt

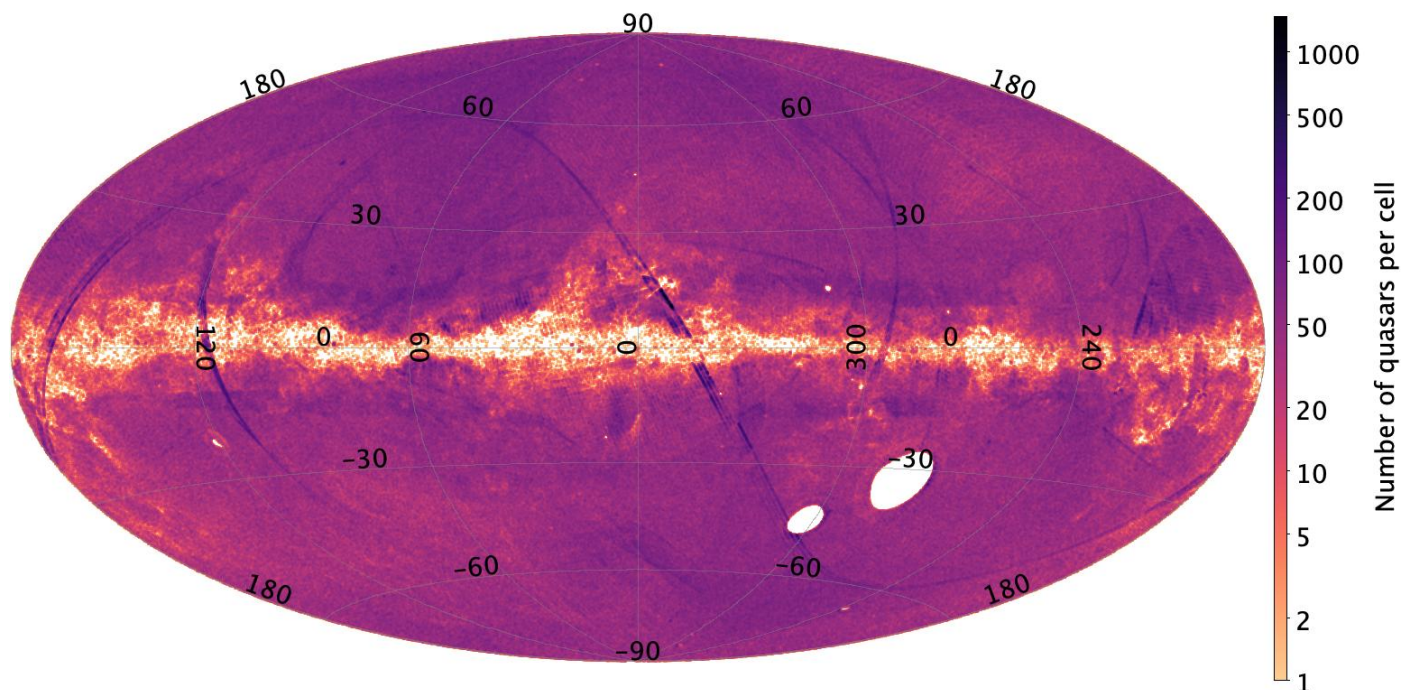


Fig. 1. Sky distribution in galactic coordinates of the quasars included in the input list. The cell of this map is approximately 0.2 deg^2 , and the colour indicates the number of sources in each cell on a logarithmic scale.

et al. 2020), and the redshift distribution when available from MilliQuas ($\sim 900\,000$ sources). The redshift distribution peaks at $z \sim 1.4$ and extends to $z \sim 6$ for a small number of sources.

3. How GravLens searches for sources near quasars

The all-sky coverage and ~ 180 mas angular resolution make *Gaia* an exceptional instrument to search for lenses. Most currently known lenses have image separations $\gg 1''$ (e.g. Ducourant et al. 2018)¹. Nevertheless, the expected distribution of lenses should peak at smaller separations, $\lesssim 1''$, making most of them quasi-undetectable from the ground (e.g. Finet & Surdej 2016). Unfortunately, the *Gaia* DR2 and *Gaia* DR3 are incomplete at separations $\leq 2''$ (e.g. Arenou et al. 2017, 2018; Fabricius et al. 2021; Torra et al. 2021). This results from a severe selection on the astrometric and photometric quality indicators of the sources that are published in these Data Releases.

The primary goal of GravLens is to detect secondary sources near QSOs and QSO candidates, and derive their mean astrometry and raw photometry. In this context, each source that is detected in a field centred in the coordinates of a quasar is named *component*. The ensemble of all the components in a field is named *multiplets*. The field centred on a quasar is designated by *quasar*.

3.1. The adopted *Gaia* data

The instruments and focal plane of the satellite are well-described in (Gaia Collaboration et al. 2016). Unlike most *Gaia* data processing chains that assign transits to a single source exploiting the *Gaia* cross-match (Torra et al. 2021), GravLens manipulates upstream data and allows a finer clustering to separate adjacent sources. The data adopted by GravLens comes from the

pre-processing step of *Gaia* treatment which is referred to as Image Parameter Determination (IPD, Fabricius et al. 2016). The purpose of IPD is to transform the raw spacecraft telemetry into basic astrometric and photometric measures for the Sky Mapper (SM) and Astrometric Fields (AF) windows. Our input data is the *Gaia* DR3 IPD outputs (flux and positions). These epoch positions are not the high-precision one-dimensional *Gaia* astrometry, but approximate 2D positions with a resolution of about one CCD pixel. GravLens uses the positions (right ascension and declination) of each transit, the fluxes in the *G*-band measured in SM and AF windows, and a rough on-board estimation of the *G* magnitude done in the *Gaia* Video Processing Unit (VPU, de Bruijne et al. 2015; Fabricius et al. 2016)². GravLens identifies by itself all *Gaia* transits within $6''$ of each quasar, without relying on the *Gaia* standard cross-matching since at this stage of the data processing, the *Gaia* cross-match is not yet known. The *Gaia* cross-match might subsequently identify more additional sources in the field at the later processing stages, but this is not included in GravLens.

3.2. The GravLens clustering algorithm

GravLens uses the Density-Based Spatial Clustering of Applications with Noise (DBSCAN) algorithm (Ester et al. 1996) for unsupervised clustering³. Without indicating the number of clusters, as required, for example, for K-Means algorithms, it identifies groups of connected points and outliers. The principle of DBSCAN is to build a neighbourhood graph by connecting points (which here are individual detections in right ascension and declination) if their distance is smaller than a certain ϵ . Here, adopt $\epsilon = 100$ mas, a value chosen empirically that is within the

² The resolution of the onboard estimation of the *G* magnitude is 0.015625 mag.

³ We used the software implementation from the Apache Commons Math library v.3.6.1.

¹ See also <https://research.ast.cam.ac.uk/lensedquasars/>

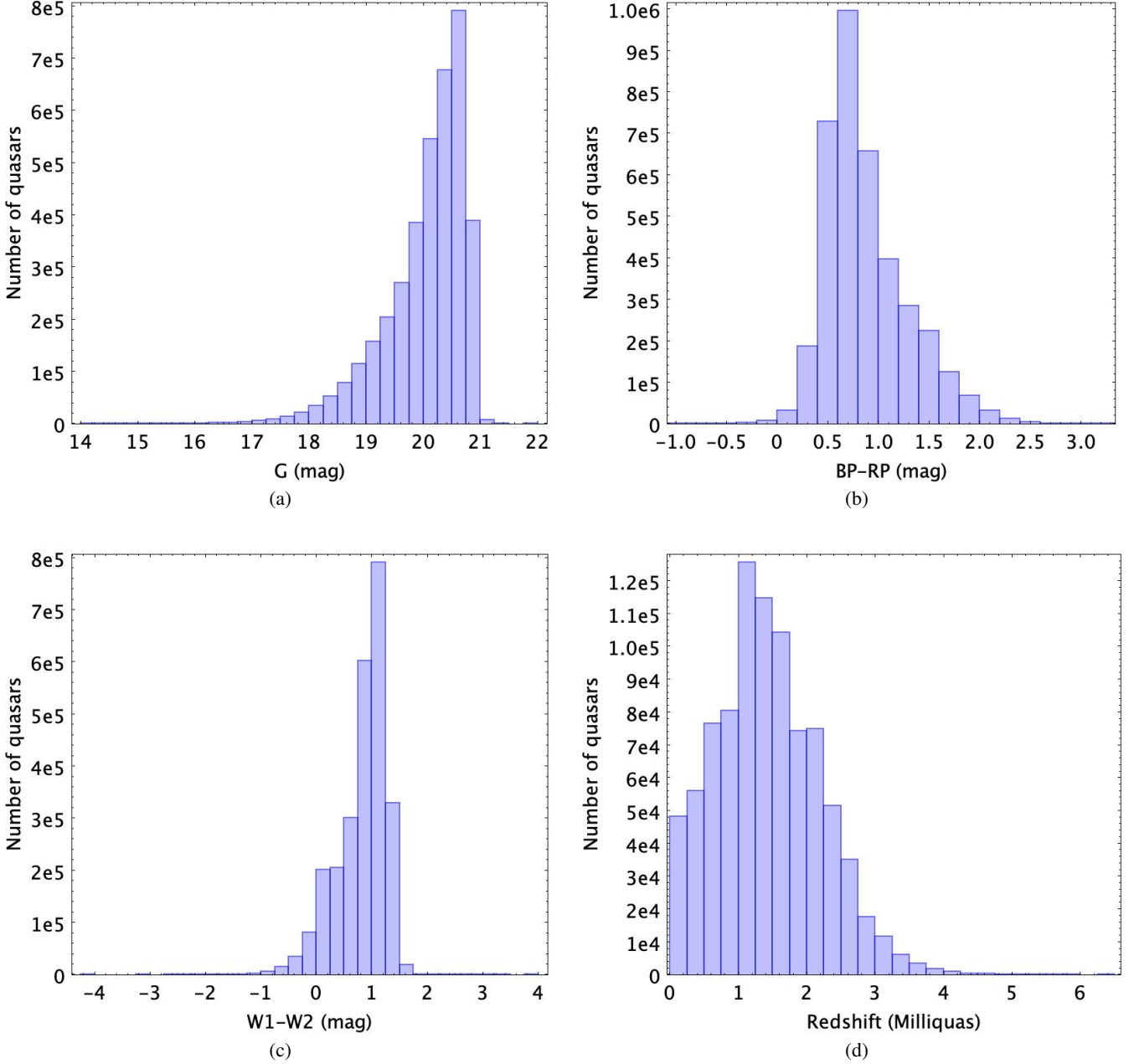


Fig. 2. Distributions of (a): *Gaia* G magnitudes (phot_g_mean_mag) from the *Gaia* DR3 gaia_source table, (b): $G_{\text{BP}} - G_{\text{RP}}$ colours ($\text{phot_bp_mean_mag} - \text{phot_rp_mean_mag}$), (c): W1-W2 colours (from catWISE), (d): redshifts (from MilliQuas) of the quasars and candidates from the input list.

PSF width of *Gaia*, thus corresponding to an angular distance that the instrument cannot physically resolve individual sources. The angular distances between the points are calculated using the haversine formula (e.g. de Mendoza y Ríos 1795).

While there are non-connected points within ϵ , the algorithm tries to connect them, and thus the graph grows. Otherwise, the set of connected points remains as is. When at least $\text{minPts} = 3$ (empirically chosen) points are connected, a cluster is formed (called a component); otherwise, the points are considered outliers. All *Gaia* transits associated with an entry of the quasar catalogue are then either outliers or within components (clusters). Once the clustering is complete, a sigma-clipping filter based on the positions and the magnitude is applied to the components, using 3σ as the threshold. The GravLens processing of the quasars has produced a catalogue of ~ 4.7 million components.

As an example of GravLens results, Fig. 3 illustrates the application of the clustering algorithm on the well-known lens Einstein cross G2237+0305 (Huchra et al. 1985). Five components are found by GravLens, corresponding to the four images of the quasar, and to the lensing galaxy that is also clearly detected.

3.3. Clustering issues

The GravLens algorithm is efficient and, in most lensing configurations reaches an optimal solution. However, occasionally, it converges to sub-optimal solutions. Fig. 4 illustrates some examples of known issues.

We show in Fig. 4 (a) the known quadruply imaged lens (Krone-Martins et al. 2018; Wertz et al. 2019), that corresponds to the multiplet DR3Gaia113100.075-441959.69. *Gaia* DR3

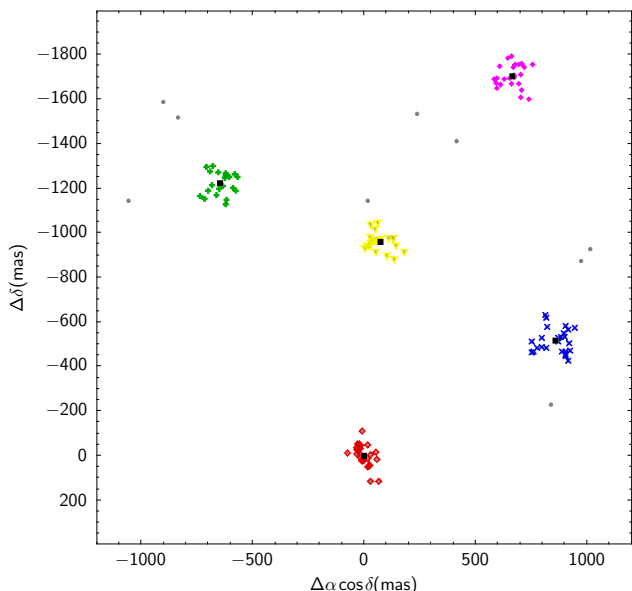


Fig. 3. GravLens results for the Einstein cross G2237+0305 (DR3Gaia224030.229+032130.03 in our output). The black dots represent the five components and the blue crosses, red diamonds, green crosses, and pink dots represent the four images of the quasar. The yellow triangles show the *Gaia* transits on the deflecting galaxy. The information is in the `ra_obs`, `dec_obs` fields of the `lens_candidates` and `lens_outlier` tables.

identifies four distinct sources with their own `source_id`. In the figure, all *Gaia* detections are plotted, and the two known components in the top left were merged by GravLens, which only outputs three components. The two components are connected by detections closer than 100 mas which causes the method to group the two sources; this is a major drawback of the DBSCAN algorithm. The central point, identified as an outlier, could even bring some physical information about the lens. The end user of the tables of this FPR should be aware that useful information may be present in the outliers table.

We show another example of a clustering issue in Fig 4 (b). This figure corresponds to the source DR3Gaia235007.548+365434.45. This source is a known doubly image quasar, but GravLens identified only one of its components. The component is 2.9'' away from the quasar and the individual detections at the quasar position were labeled as outliers. Therefore, the information is not completely lost, but present in the `lens_outlier` table. Five transits are near the quasar but the distance between the transits is $> \epsilon = 100$ mas so they are not considered to be a component. The astrometry may have been perturbed by the deflecting galaxy and the *Gaia* DR3 astrometry is unreliable, presenting errors of ~ 17 mas.

We illustrate the case of a large planetary nebula (IC 351) decomposed into many components in Fig. 4 (c). This figure represents the source DR3Gaia034732.982+350248.6. There are 3 508 *Gaia* observations in this field. GravLens found 120 components with 2 768 detections, and 740 outliers. This example highlights one of the causes of the large number of components in certain fields when an extended object is decomposed.

Figure 4 (d) shows another odd example of a large number of detections (DR3Gaia082523.532+241524.53). In this case, the central source is a very bright object (magnitude ~ 9.7). GravLens detects 136 components in radial spokes from the central source, based on 2 481 observations, of which 1 424 are considered outliers. A halo of outliers is present around this source.

3.4. Post-processing

After the GravLens processing, we perform a post-processing stage. The post-processing can handle specific situations and flag problematic sources or sources to be discarded. In particular, we observed an excess of doublets separated by less than 300 mas and with ≤ 5 observations of one of the components. A small fraction of these are probably real sources but the majority of them result from the excessive decomposition of single sources into doublets by the clustering algorithm. The post-processing gathered these nearby components into single sources for $\sim 200\,000$ doublets.

The post-processing aims at raising flags to indicate problematic multiplets or multiplets which are clearly not lensed quasars. The flags are raised at the quasar level `flag` and/or at the component level `component_flag`.

The `flag` is a two-bit binary flag. The first bit is set to 1 if the maximum difference of magnitude within the multiplet is larger than 5 mag which indicates that it is very improbable that this is a lensed quasar. The second bit is set to 1 if there are more outliers than clustered observations, such as could be the case for a galaxy and other extended objects, see, e.g. Fig. 4 (c).

The `component_flag` is also a two-bit binary flag. The first bit is set to 1 if the standard deviation in right ascension or declination of a component is larger than 100 mas. A point source should yield $\sigma_{RA,Dec} \approx 60$ mas, at the order of the uncertainty of the RA/Dec of the SM position. The second bit is set to 1 if the standard deviation of the raw mean magnitude is larger than 0.4 mag. In both cases, `component_flag` points to unusually high measurement uncertainty, possibly resulting from a bright nearby source or several very nearby sources which are considered a single component. There are 4 444 145 components with both flags set to 00, indicating no alert is raised. This represents 93% of all components.

4. The catalogue of sources around quasars

GravLens has analysed 183 368 062 transits matched to the 3 760 480 quasars from our list during the first three years of *Gaia* operations. It attributed 171 545 519 transits to components and rejected 11 822 543 as outliers. GravLens did not converge in 448 cases. Within 6'' of the 3 760 032 quasars, 4 760 920 sources were found (see Table 1), including the quasars.

These results are included in the `lens_candidates` table. The data model of the catalogue is presented in appendix A. Additional information can be found in the table `lens_catalogue_name` (see Sect. 2). The individual observations of each component and the outliers are found in the `lens_observation` and `lens_outlier` tables (see [link to the FPR documentation](#) for a detailed description of all tables and fields).

4.1. General properties

The distribution of the main properties of the components published in the `lens_candidates` table is given in Fig. 5 and the number of sources detected in the fields of the quasars along with the number of components in the fields is given in Table 1.

The vast majority of the quasars (87%) have no neighbour within 6'' and 9% are doublets. There are $\sim 159\,000$ multiplets with more than 2 components (4%). The search for quadruply imaged quasars will therefore focus on this sample of multiplets. There are $\sim 9\,000$ multiplets containing a large number of com-

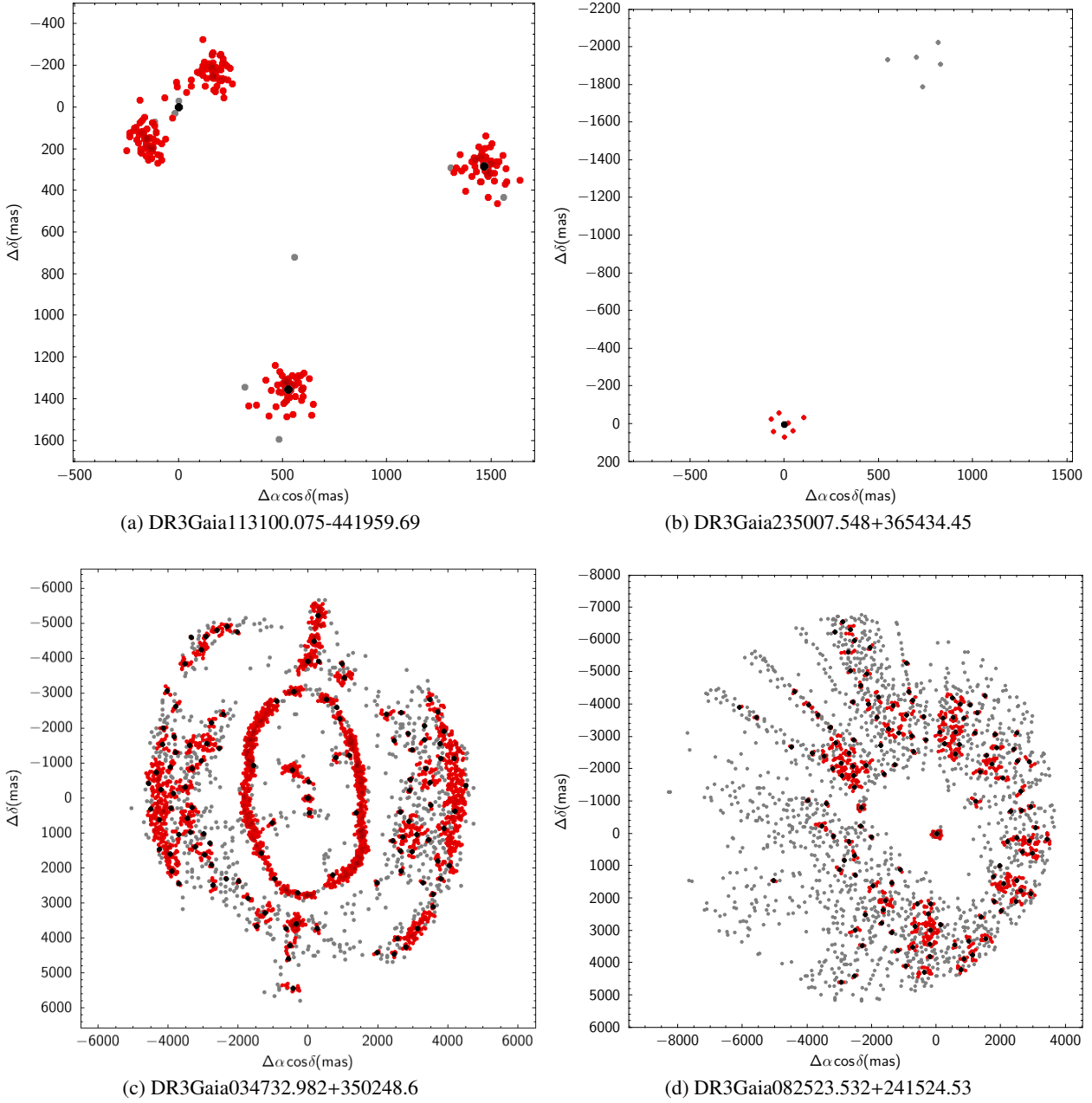


Fig. 4. Examples of known issues. Black dots are the mean positions of the components, red points correspond to individual observations no matter the component and gray dots are outliers. In (d) a planetary nebula (IC 351) that unduly entered in the quasar catalogue is decomposed by the algorithm into numerous sources, as well as in (d) for the halo of a bright star.

Table 1. Source counts in the `lens_candidates` table according to the number of components in the field.

Selection	Nb of quasars	Nb of components
All	3 760 032	4 760 920
1 component	3 258 647	3 258 647
2 components	341 551	683 102
3-10 components	149 953	618 838
11+ components	9 881	200 333

ponents (> 10). They generally correspond to large galaxies decomposed in many sources as seen in Sect. 3.3.

The distribution of magnitudes follows that of the quasars in the input list (see Fig. 2), reflecting the fact that the majority of the sources in our catalogue are not multiply-imaged.

Components have a median of 36 observations, ranging from three to 630 observations, and are time-resolved. Sources with a very low number of observations should be considered with caution and generally correspond to the faintest sources detected.

4.2. Astrometry and photometry

GravLens astrometry and photometry are meant to complement the information from the current *Gaia* Data Releases, especially for the sources that are not present in the latter. GravLens magnitudes and fluxes use uncalibrated onboard magnitudes, for instance. For many GravLens sources not published in *Gaia* DR3 the measurements are poor, as these sources are usually faint. The mean standard deviations are 62 mas and 57 mas, respec-

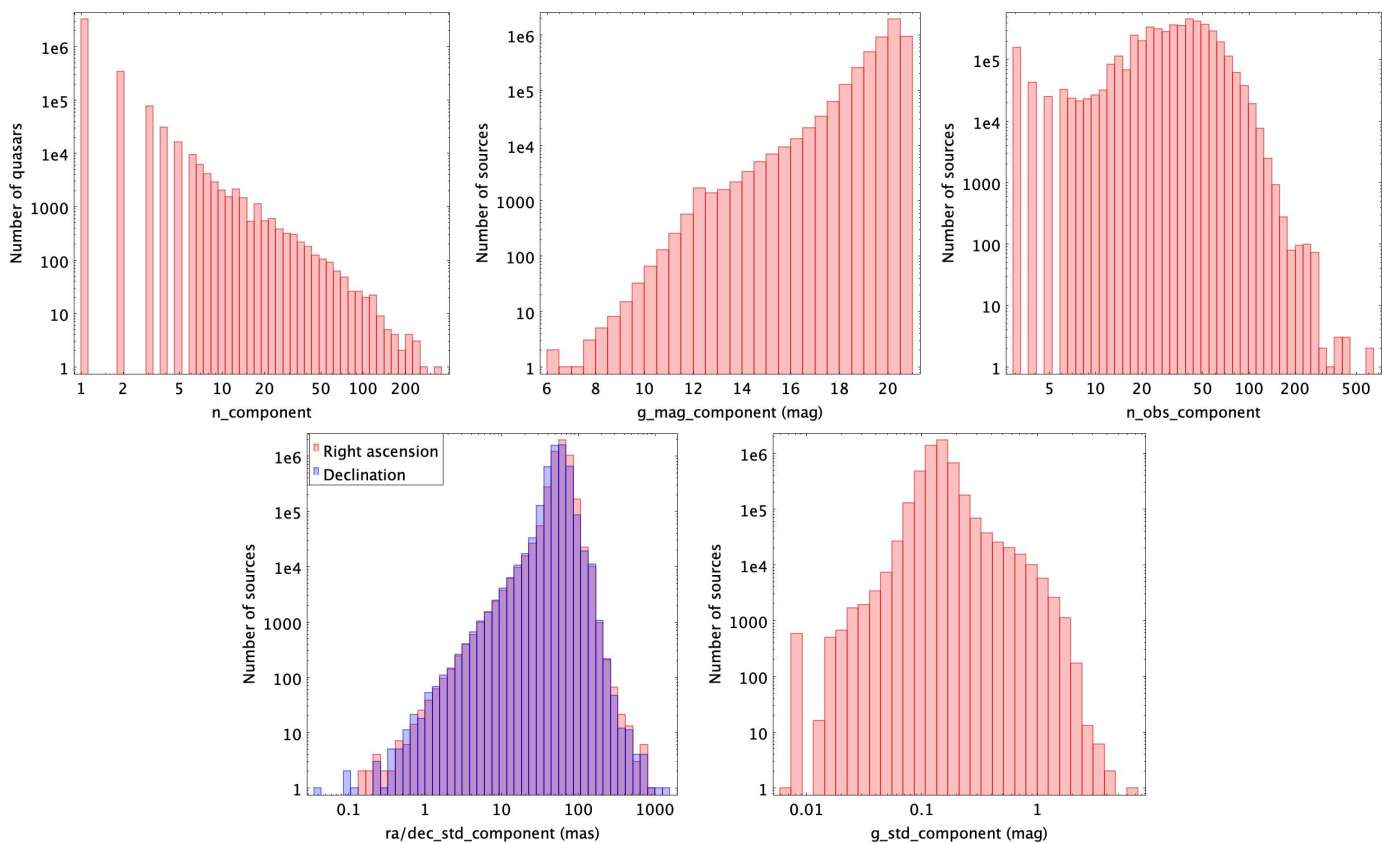


Fig. 5. Distributions of components' main features provided in the `lens_candidates` table - (a): number of components found in the fields analysed, (b): mean G magnitude of the components of all fields. (c): number of observations of the components. (d): standard deviation of mean coordinates (`ra_component`, `dec_component`) and (e): standard deviation of mean G magnitude.

tively, for right ascension and declination and 0.15 mag for the magnitudes.

The GravLens and *Gaia* DR3 positions and magnitudes for common sources are compared in Fig. 6. A slight asymmetry is present in RA and Dec, with $(RA_{GL} - RA_{DR3}) \approx -1.33\text{mas}$ and $Dec_{GL} - Dec_{DR3} \approx -5.4\text{mas}$, with dispersions of $\sim 13\text{mas}$.

The GravLens magnitudes agree well with *Gaia* magnitudes with a mean difference of -0.06 mag and a standard deviation of 0.15 mag. Around $G = 12 \pm 0.5$ mag, the GravLens magnitudes are slightly higher. This is a well-known effect of the uncalibrated onboard magnitudes (Riello et al. 2018), and for *Gaia* DR3 magnitudes ≥ 21 , the GravLens magnitudes are quite dispersed and generally lower (i.e. the magnitudes can be overestimating the true brightness of the source).

The astrometry and photometry of the GravLens components are based on the *Gaia* onboard detections, and should be much improved in the future Data Releases solutions when the individual components are properly handled.

4.3. New sources not in *Gaia* DR3

There are $\sim 10\,500$ *Gaia* DR3 sources in the vicinity of analysed quasars ($6''$) that are not among the GravLens components, representing less than 0.2% of all GravLens components. Meanwhile, there are 306 970 new sources that are not in *Gaia* DR3 among the 4 760 920 GravLens components. About $\sim 200\,000$ new sources are either bright with `g_mag_component` < 17.5 mag or in crowded fields with `n_components` > 20 (Fig. 7). The bright new sources correspond to problems illustrated in Fig. 4 (c and d). They are generally flagged either at the *quasar* level

(`flag`) or at the *component* level (`component_flag`) (see Sect. 3.4 for a description of the flags). After this process, $\sim 103\,000$ new sources remain which are not flagged and believed to be bona-fide sources.

4.4. Known lenses

We first compare the GravLens results to known lenses. The GravLens catalogue includes ~ 450 known or candidate lenses published in the literature, 76 with 4 images (quads) and the rest being doublets. For 67 quads out of the 76 quads, GravLens complements the existing measures from *Gaia* DR3 by measuring one or more additional components or the deflecting galaxy. In total GravLens measured 1 293 components in the fields of known lenses while 1 207 are present in *Gaia* DR3. The 86 newly detected components in the fields of known lenses are mostly faint real components lying around lenses with a previously small number of *Gaia* DR3 counterparts.

We show two examples in Fig. 8. This figure shows Pan-STARRS images (Chambers et al. 2016) of two known lenses: the Einstein cross G2237+0305 (Huchra et al. 1985) where GravLens detects all 4 images of the quasar and the deflecting galaxy while *Gaia* DR3 only contains two entries, and 2MASSJ13102005-1714579 (Lucy et al. 2018) where GravLens detects the four images of the quasar and two central deflecting galaxies that had no entry in *Gaia* DR3.

Some of the presently known lensed quasars have been targeted by the Hubble Space Telescope (HST), and new structures can be found in the HST source catalogue version 3 (Whitmore

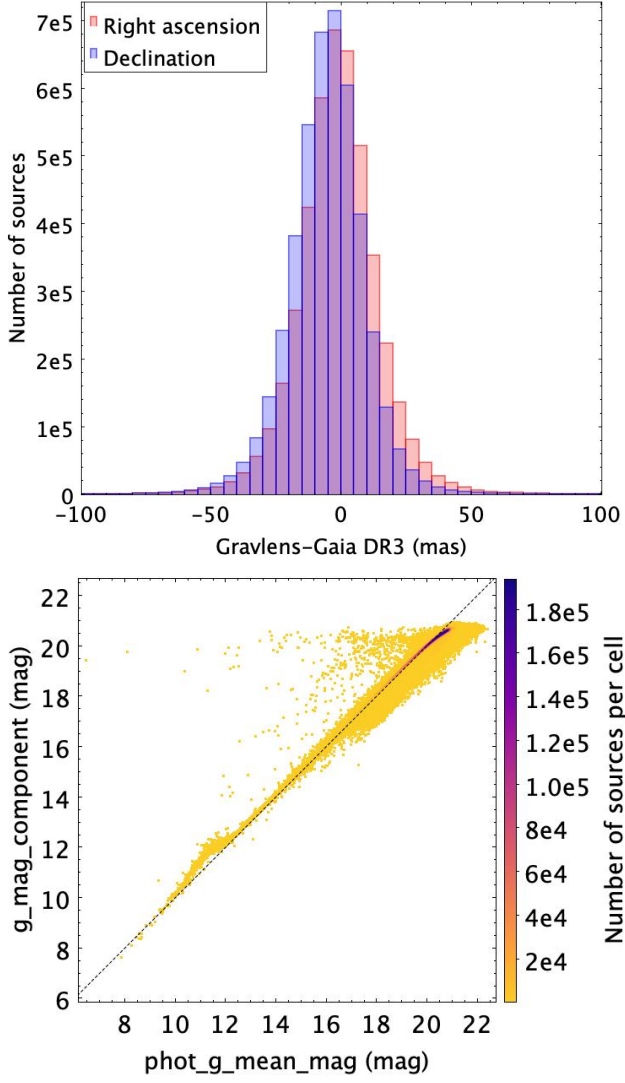


Fig. 6. Comparison between coordinates and magnitudes from GravLens and *Gaia* DR3. (Top) Comparison of the coordinates (ra, dec) derived by GravLens and by *Gaia* DR3. Δ ra includes the $\cos(\text{dec})$ factor. (Bottom) Comparison of GravLens magnitudes (table lens_candidates field g_mag_component) with *Gaia* DR3 magnitudes (table gaiadr3.gaiadr3 field phot_g_mean_mag).

et al. 2016). However, of the 476 known lenses, only 69 have space-borne measurements from the HST catalogue.

5. Search for new lenses

To look for new lenses and help guiding the users of this FPR, we developed two methods using artificial intelligence: an outlier scoring algorithm (Sect. 5.1) and the application of Extremely Randomised Trees (Delchambre et al. 2019, and Sect. 5.2). When *Gaia* spectra are available, we also make use of this information, and in Sect. 5.3 we explain the method that compares the mean BP and RP-spectra using chi-squares and Wasserstein distances. High-scoring multiplets are then visually inspected.

5.1. The Hesiod score for the input list of quasars

Only a small fraction of components near quasars are expected to be quasar images. So, analysing the quasars from the list presented in Sect. 2 to identify good lens candidates can be seen

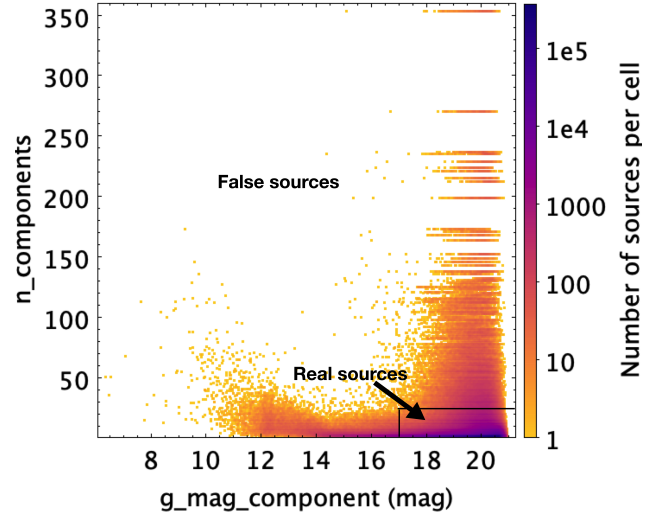


Fig. 7. Density plot of the magnitudes of the GravLens components not present in *Gaia* DR3 along with the number of components in the multiplet. Colour scale is logarithmic.

as an outlier detection or a one-class classification problem. Accordingly, we can use these techniques to produce a lens score.

In these methods, distances, densities, and, in some instances, labeled data are used to train to identify a class called the positive class (see, e.g. Elkan & Noto 2008). The supervised or semi-supervised training assumes (a) that the learning method has access to a reliable subset of positive examples such as spectroscopically confirmed lenses and (b) that the data contains positive and unknown examples (i.e. new lenses and other objects).

To increase the reliability of the scores, photometric and astrometric indicators from the *Gaia* DR3 data (Gaia Collaboration et al. 2023a) and public unWISE data (Lang 2014) were calculated based on sources within $6''$ of each quasar. Missing data patterns appear when sources lack *Gaia* DR3 or unWISE data or when there is no unWISE counterpart for a *Gaia* source. Missing data is a serious problem that prevents the adoption of many approaches readily available in the literature (e.g. Bekker & Davis 2020). So, to produce a score in this situation, we developed a simple heuristic method that we call HESIOD for Heuristical Ensemble Splitting Imputation and Organization of Data that can be applied to large datasets as it is embarrassingly parallel.

HESIOD assumes that the dataset can be described by a single matrix \mathbf{D} of n rows by d columns. Each row corresponds to an astronomical source, and each column corresponds to a physical parameter (e.g. astrometric and photometric measurements from *Gaia* and unWISE, maximum and minimum angular distances and color differences between sources, etc.). \mathbf{D} can be incomplete in that not all elements D_{ij} are filled (i.e. data for one or more column j can be missing in any row i). The binary vector $\mathbf{c} \in \{0, 1\}^n$ encodes the class of the i -th row (i -th source); $c_i = 1$ if the source belongs to the *positive* class, here equivalent to a known lens, and $c_i = 0$ if the class is unknown. Only k components of the vector \mathbf{c} are equal to one, with $k \ll n$. HESIOD is a method \mathcal{H} to estimate a vector $\mathbf{o} \in R^n | 0 \leq o_i \leq 1, \forall i \in [1, n]$, from \mathbf{D} and \mathbf{c} (i.e. $\mathcal{H}(\mathbf{D}, \mathbf{c}) \rightarrow \mathbf{o}$), such that \mathbf{o} contains a score o_i for all n rows (sources) of \mathbf{D} to indicate if the i -th source can belong to a different class than the *positive* class (the lenses). HESIOD thus starts with the known lenses \mathbf{c} and ends with a new real-valued vector \mathbf{o} . The vector \mathbf{o} is initially an outlier score, that is, a score for the source not being a lens, which we complement (i.e. $1 - \mathbf{o}$) to obtain a lens score.

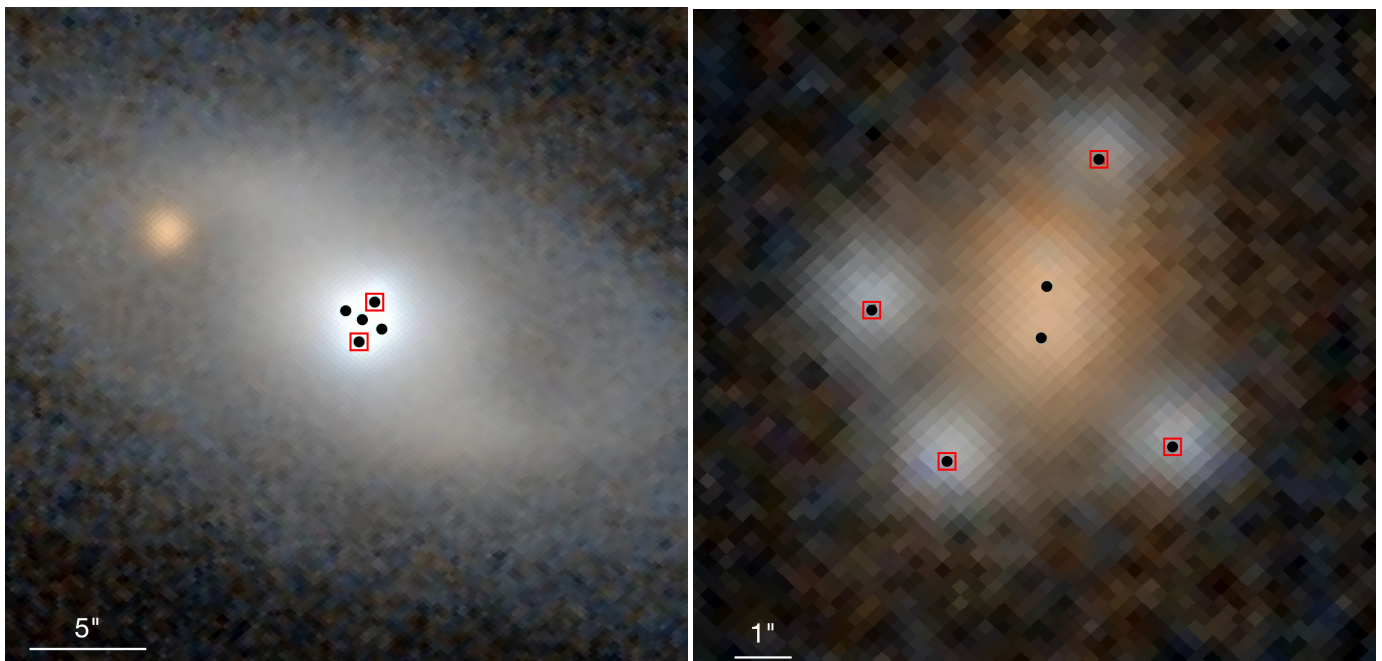


Fig. 8. Pan-STARRS images (Chambers et al. 2016) of two known gravitational lenses with an indication of GravLens components in black (filled circles) and entry in *Gaia* DR3 in red (squares). Left: the Einstein cross (G2237+0305). Right: 2MASSJ13102005-1714579. The central sources in 2MASSJ13102005-1714579 encompasses two lensing galaxies recovered as GravLens components.

Informally, HESIOD solves this problem by creating ensembles of smaller problems that are easier to solve. It has two steps, an initial ‘inner’ phase followed by an ‘outer’ phase, as in UPMASK (Krone-Martins & Moitinho 2014). The inner phase randomly splits the matrix \mathbf{D} into a set of m smaller $p \times d$ sub-matrices $\{\mathbf{S}_j | \forall j \in [1, m]\}$, without replacement. This corresponds to random partitions of the catalogue into random samplings of sources (keeping all the associated data). Then, an imputation method \mathcal{I} solves the less complex imputation problem for each sub-matrix ($\mathcal{I}(\mathbf{S}_j) \rightarrow \tilde{\mathbf{S}}_j$). Afterward, a $\tilde{\mathbf{D}}$ matrix is reassembled from the results of the imputations on the \mathbf{S} sub-matrices, and multiple outlier or one-class classification methods \mathcal{C} produce scores from $\tilde{\mathbf{D}}$ and the vector \mathbf{c} , resulting in the matrix $\tilde{\mathbf{O}}$ containing the scores for each source (i.e. $\mathcal{C}(\tilde{\mathbf{D}}, \mathbf{c}) \rightarrow \tilde{\mathbf{O}}$).

The outer phase of HESIOD executes the inner phase q times, resulting in a set of matrices $\{\tilde{\mathbf{O}}_l | \forall l \in [1, q]\}$. This ensures diversity in the imputation process due to the random splitting of \mathbf{D} . Then it runs the final scoring method \mathcal{O} over the matrix \mathbf{O} , where $\mathbf{O} = \tilde{\mathbf{O}}_1 | \dots | \tilde{\mathbf{O}}_l$ (i.e. this matrix is the concatenation of the individual matrices resulting from the q runs of the inner phase), producing a final score for each source (i.e. $\mathcal{O}(\mathbf{O}) \rightarrow \mathbf{o}$), where \mathbf{o} is a score for the source to be an outlier (i.e. not a lens), and $1 - \mathbf{o}$ is the HESIOD score.

Since here the *positive class* is composed of lenses, which correspond to a small number of rows of the total dataset \mathbf{D} , all known lenses are concatenated with each sub-matrix \mathbf{S} . This is important to avoid significantly biasing the imputation process against the lenses.

The HESIOD results depend on the choice of the ensembles of methods used for imputation \mathcal{I} and classifications \mathcal{C} and \mathcal{O} . In this work, we adopted different methods based on ensembles of decision trees. We adopted miceRanger (Wilson 2021) for the imputation \mathcal{I} . This is a version of the Multiple Imputation by Chained Equations method (van Buuren 2007) that uses a random forest regression for individual imputations (Stekhoven & Bühlmann 2011), as in Ducourant et al. (2017). For the outlier

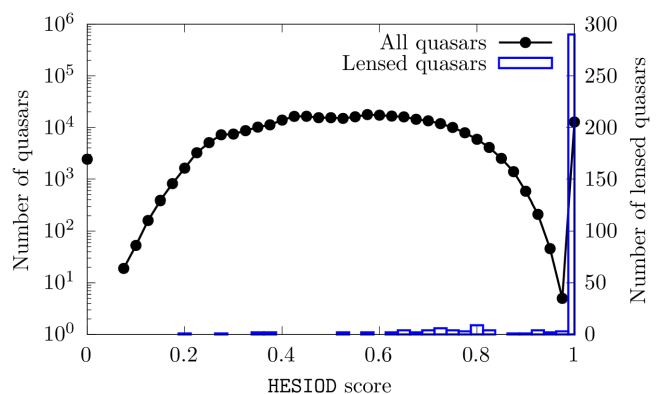


Fig. 9. Distribution of the HESIOD score for the 319 296 quasars for which it was computed. We note that the left axis corresponds to all the quasars and is represented in logarithmic scale, while the right axis corresponds to the known lenses and is represented in linear scale.

scoring \mathcal{C} we use three types of ensembles of decision trees as there is usually no optimal method for all problems (e.g. Wolpert 1996; Wolpert & Macready 1997; Cortes 2021): the classic Isolation Forest method (Liu et al. 2008), SciForests (Liu et al. 2010), and Fair-Cut Forests (Cortes 2019). The final outlier score \mathcal{O} also uses Fair-Cut Forests. The resulting distribution of the HESIOD scores is presented in Fig. 9. Known lenses were iteratively used during the training, so it is expected that their scores would peak at high values, which indeed happens. The results on all 319 296 sources for which the method produced results show a central peak indicating more uncertain sources and two sharp peaks at the low and high score extremes.

The HESIOD method seems effective in the present lens candidate scoring application since it was designed to deal with large datasets with missing data and, moreover, to consider a parameter space constructed from combinations of the measurements of all sources around the analysed quasar. The param-

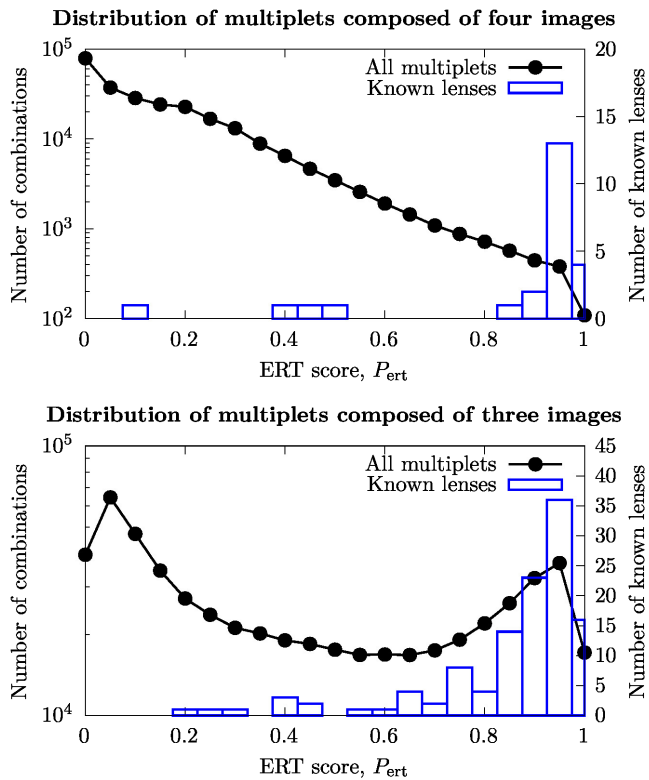


Fig. 10. Distribution of the ERT scores for the 56 398 multiplets (24 known lenses) composed of at least four components (top) and 134 656 multiplets (45 known lenses) composed of at least three components (bottom). If multiplets are composed of more than three or four components, respectively, then all combinations of three and four components are considered for computing the ERT scores.

eter space (i.e. columns of the matrix \mathbf{D}) is constructed from summary information about distributions of the measurements of all sources around the quasar, such as minimum and maximum differences in color in all possible *Gaia* DR3, unWISE, *Gaia*-unWISE W1 and W2 bands, astrometric errors, angular distances, between the images, as well as global properties of the parameter distributions as the minimum, mean and maximum astrometric and photometric errors, astrometric excess noise, RUWE, BPRP excesses and signal to noise ratios (e.g. fluxes, positions, proper motions and parallaxes over their errors) for all sources. As such, the HESIOD score is assigned for the entire candidate system, composed of multiple *Gaia* DR3 sources. This parameter space also enables HESIOD to deal with more challenging lensing cases. For instance, although gravitational lenses are achromatic, one or more of the quasar images can be superposed with parts of the lensing galaxy, and in the most extreme cases, the lensing galaxy can be completely unresolved and mixed with one or more images due to finite spatial resolution. In such cases, property gradients (such as color, and astrometry) could be expected to exist within the candidate system, and HESIOD can deal with such non-textbook lensing cases as long as there are similar examples among the *positive* class sample in \mathbf{D} .

5.2. Extremely Randomised Trees

Another technique for identifying strong gravitational lenses assumes that multiplets whose positions and magnitudes can be modelled by a singular isothermal ellipsoid in the presence of an external shear (Kormann et al. 1994, hereafter SIE γ lens model)

are good lens candidates. Whereas doublets do not yield a sufficient number of constraints to properly assess if their component positions and magnitudes can be reproduced through a SIE γ lens model, those composed of three or four images do. Classical lens modelling tools, such as those from Keeton (2001) or Birrer et al. (2015), are based on a sampling of log-posterior distributions, which efficiently provide estimates of the lens model parameters along with a thorough estimate of their uncertainties. As we are not interested in those parameters but only in the ability to reproduce the multiplet positions and fluxes, we choose to simulate the relative positions and magnitudes of quadruple lenses using a SIE γ lens model, then simulate random multiplets and train a supervised machine learning model to identify the simulated lenses from the random multiplets.

For this purpose, we use an updated version of the method described in Delchambre et al. (2019), which is based on Extremely Randomised Trees (Geurts et al. 2006, hereafter ERT). The training used 112 784 simulated quadruple lenses drawn from a SIE γ model. The simulations use random values of the ellipticity and shear drawn from the distributions provided in Petit et al. (2023) and in Holder & Schechter (2003), respectively. A Gaussian noise with a standard deviation of 0.3 mag was also added to the simulated magnitudes in order to deal with the imperfection of the SIE γ lens model (galaxy substructures, micro-lensing, time delays, ...), see (Delchambre et al. 2019, Section 3.2) for details. We also simulated a similar number of random multiplets using *G* magnitudes drawn from the empirical *Gaia* DR3 distribution. Cross-validation tests, where 20% of our simulations are kept as a test set and 80% of our simulations are used for training, show that 90.4% of our simulated lenses are recovered by the method if four images are present while 0.7% of the random multiplets are falsely classified as lenses. These numbers become 90.3% and 12.5% if triplets are considered⁴. When only three out of the four lensed images are observed, we do not know – a priori – which lensed image is not detected (not necessarily the faintest). We test the four possibilities and keep the highest score. Similarly, if a multiplet is composed of more than 3 components, we consider all combinations of 3 and 4 components out of this multiplet. This allows us to identify quadruply imaged quasars having a contaminating star or (lensing) galaxy in their vicinity.

Figure 10 shows the ERT scores, P_{ert} , for all combinations of three and four images of the GravLens multiplets. We can see that 20/24 (83%) of the known lenses have $P_{\text{ert}} > 0.8$ if four components are available, while only 0.75% of the combinations of four components from the GravLens multiplets have $P_{\text{ert}} > 0.8$.

Regarding the combinations of three components, 91/117 (78%) of the combinations from known lenses have $P_{\text{ert}} > 0.8$ compared to 22.7% of all multiplets. This is in good agreement with the identification performance estimated from cross-validation tests. The differences for three components are mostly explained by the fact that we keep the maximal score out of the four ERT models (and explains the peak at $P_{\text{ert}} \approx 0.95$ in the bottom panel of Fig. 10). Misclassified lenses can either be due to the inability of the SIE γ model to reproduce the observed fluxes or positions of the lens (e.g. if two lensing galaxies are present), to extreme values of the eccentricity or shear (i.e. not covered by our simulations) or to microlensing (see Delchambre et al. 2019, for further discussions).

⁴ The areas under the receiver operating characteristic curve are equal to 0.9958 and 0.9554 for the cases of four images and three images, respectively.

5.3. Comparison of mean BP/RP spectra

The most secure way of identifying strong gravitational lenses is to compare the spectral energy distributions (SEDs) of their images. Indeed, as the background quasar is unique and the lensing phenomenon achromatic, all of the lensed images should have similar SEDs (except for any absorption by the deflecting galaxy; intervening gas and lens time delays). *Gaia* provides epoch spectro-photometry in the blue (300–700 nm, resp. BP) and in the red (600–1100 nm, resp. RP) part of the optical domain (Gaia Collaboration et al. 2016), and hence should be a very powerful tool to identify lenses. *Gaia*'s spectral resolution of $R = \lambda/\Delta\lambda \leq 100$ with a full width at half maximum between 10 nm and 40 nm (Montegriffo et al. 2023), can however hardly differentiate strongly lensed quasars from quasar pairs, although both have important applications in cosmology (see Mannucci et al. 2022, for examples).

To compare components of a GravLens multiplet, we use the *Gaia* epoch BP/RP spectra associated with each of the components since we cluster components at the transit level. Each of these epoch spectra has 60 fluxes, associated uncertainties, and pixel positions in the along-scan (AL) direction. Pixel positions are converted into wavelength positions using dedicated dispersion functions⁵. The spectra are not sampled on the same pixel scale due to the geometric and flux calibrations that minimise the discrepancies between otherwise similar spectra but acquired over different CCD rows, CCD columns, or TDI gates (see De Angeli et al. 2023, for details). We resample the epoch spectra on a uniform pixel grid with $\mathbf{x}_{\text{BP}} = \{13, 13.5, \dots, 36\}$ in BP and $\mathbf{x}_{\text{RP}} = \{13, 13.5, \dots, 49\}$ in RP. These cover the wavelength regions 394–690 nm in BP and 638–1022 nm in RP. For each $x \in \mathbf{x}_{\text{BP}}$ or $x \in \mathbf{x}_{\text{RP}}$, we first isolate epoch BP or RP fluxes falling in the pixel range $[x - 0.5, x + 0.5[$ and reject those for which the distance to the median flux in this range is larger than 7.5σ . We then fitted a line to the remaining fluxes and take its value at x as the value of the resampled flux, along with its associated uncertainty. Since the resampling bins overlap, correlations exist between the noise on the resampled fluxes that should be taken in account. During resampling, we estimate the total fluxes of each component, F_{BP} and F_{RP} ; their signal-to-noise ratio, S/N_{BP} and S/N_{RP} ; and a mean chi-square for the fit of the lines to the epoch fluxes in each of the resampling bin, χ_{BP}^2 and χ_{RP}^2 . High χ_{BP}^2 or χ_{RP}^2 are indicative of the inability of our resampling to fully model the variance seen in the epoch spectra. This could be due to multiple effects, such as blended sources, unfiltered cosmic rays, border effects, and high intrinsic variability of the sources, to cite a few examples. The procedure is illustrated in Fig. 11 for the case of the known lens GrAL J065904.1+162909 (Delchambre et al. 2019; Stern et al. 2021).

The resampled spectra of N components are compared using the method described in the appendices of Gaia Collaboration et al. (2023a)⁶. If \mathbf{f}_i is the resampled BP or RP spectrum of the i th component of the multiplet, then we aim to find a mean vector, \mathbf{m} , and linear coefficients, s_i , that minimise the reduced chi-square defined by

$$\chi_\nu^2 = \frac{1}{\nu} \sum_{i=1}^N \|\mathbf{W}_i [\mathbf{f}_i - \mathbf{m} s_i]\|^2 \quad (1)$$

where ν are degrees of freedom of the problem and \mathbf{W}_i is the inverse of the Cholesky decomposition of the covariance matrix

⁵ Available at the [GaiaXPpy github](#).

⁶ The Octave/Matlab source code is publicly available at https://github.com/lidelchambre/gls_mean.

associated with \mathbf{f}_i , \mathbf{C}_i , such that $\mathbf{W}_i^T \mathbf{W}_i = \mathbf{C}_i^{-1}$. Absorption of quasar light by the lens affects the colour of the lensed images so Equation 1 was evaluated separately for BP and RP before producing a single reduced chi-square. Multiplets composed of components having similar spectra thus have $\chi_\nu^2 \approx 1$. Finally, to ease the comparison of the χ_ν^2 , we use the well-known cubic root transformation (Wilson & Hilferty 1931),

$$\text{gof} = \sqrt{\frac{9\nu}{2}} \left(\sqrt[3]{\chi_\nu^2} + \frac{2}{9\nu} - 1 \right), \quad (2)$$

which approximately follows a standard Gaussian distribution that is independent of the degrees of freedom, ν , once ν is large (here the mode of ν is equal to 118).

We complement this chi-square approach by a comparison based on the Wasserstein distance (Kantorovich 1942, 2006), which is potentially more robust to outliers. Intuitively, the Wasserstein distance corresponds to the minimal ‘effort’, or optimal transport cost (e.g. Villani 2003, 2016; Peyré & Cuturi 2019), that is needed in order to convert a pile of earth into another pile, hence the reason why it is often called the earth mover’s distance. Given two set of epoch spectra, \mathbf{f} and \mathbf{g} , and their linear interpolations in pixel space, $f(x)$ and $g(x)$, we define the 1-Wasserstein distance between \mathbf{f} and \mathbf{g} as

$$W_d = \int_{\mathbb{R}} \left| \frac{F_z}{F_\infty} - \frac{G_z}{G_\infty} \right| dz \quad (3)$$

where $F_z = \int_{-\infty}^z f(x) dx$ and $G_z = \int_{-\infty}^z g(x) dx$. Two components with similar SEDs then have $W_d \ll 1$. No resampling is needed here and we do not use the uncertainties on the epoch spectra as the comparison is done on the overall shape of the epoch spectra only.

5.4. Selection of the lens candidates

Focusing on providing a first non-exhaustive list of lens candidates based on the *Gaia* FPR data, we applied the methods described above to the 491 504 multiplets with less than 7 components (Table 1) to provide scores quantifying if a multiplet is likely to be a strongly lensed quasar. As the scoring methods have different limitations, not all scores are available for all multiplets. The selection of the most promising candidates is done by isolating regions in the space defined by the parameters: P_{ert} score; minimal HESIOD score (\mathcal{O}_{min}); χ_ν^2 ; gof and W_d , with the addition of the galactic latitude, b ; maximal separation between pair of components; G magnitudes; S/N_{XP} ; integrated flux F_{XP} and mean resampling chi-square, χ_{XP}^2 . Instead of performing cuts manually, we use machine learning to compute a combined score, S_{comb} , that reflects the similarities between the multiplets and the set of known lenses. To do so, we use a cross-validation procedure where we split the set of 1 957 559 combinations of 2–6 components from the 491 504 multiplets into 100 subsets of approximately equal size. For each subset, we run a Random Forest classifier (Breiman 2001) built on the set of known lenses and on the combinations from the 99 other subsets. The combinations from these 99 subsets that are closer than $10''$ from one of the combinations in the selected subset are discarded, as the combinations from multiplets share input parameters (e.g. G magnitudes, S/N_{XP} , ...). Fig. 12 shows the distribution of the combined score for all the 1 957 559 combinations. The 869 combinations at $S_{\text{comb}} > 0.9$ correspond to combinations from known lenses. As the known lenses are always included in the Random Forest training sample, these will automatically have

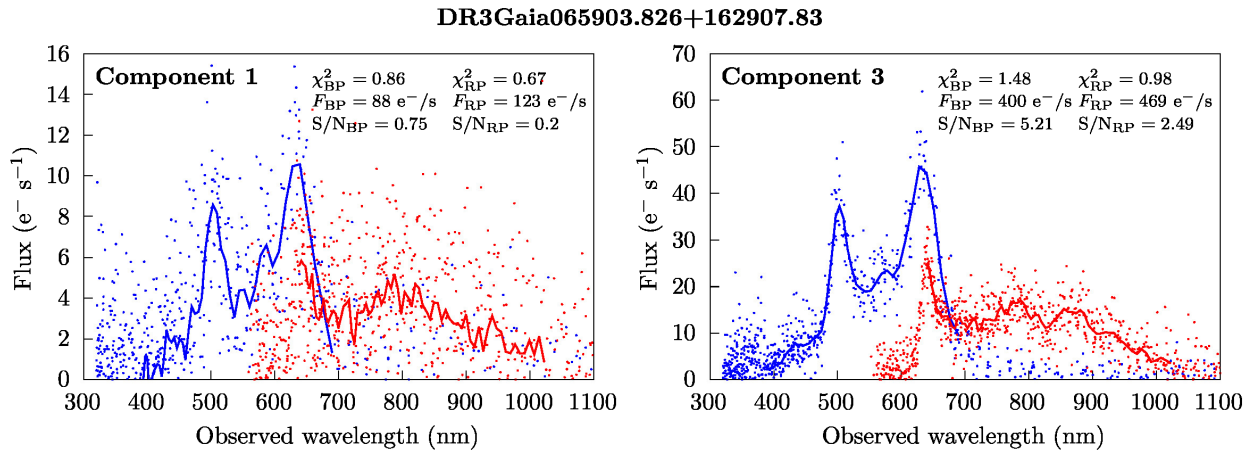


Fig. 11. Epoch and resampled BP and RP spectra of the first and third components of quadruple lens system GraL J065904.1+162909 (Delchambre et al. 2019; Stern et al. 2021), corresponding to the GravLens multiplet DR3Gaia065903.826+162907.83. Points are the epoch BP/RP spectra of each of the components (blue for BP, red for RP) while solid lines are the resampled BP/RP spectra, as described in Sect. 5.3. We also provide the additional parameters derived during the resampling phase: mean resampling chi-square (χ_{XP}^2), integrated flux (F_{XP}) and signal-to-noise ratio (S/N_{XP}) where XP stands for BP and RP. Both component spectra show strong Ly α and C IV emission lines that allow us to unambiguously identify this multiplet as a lensed quasar.

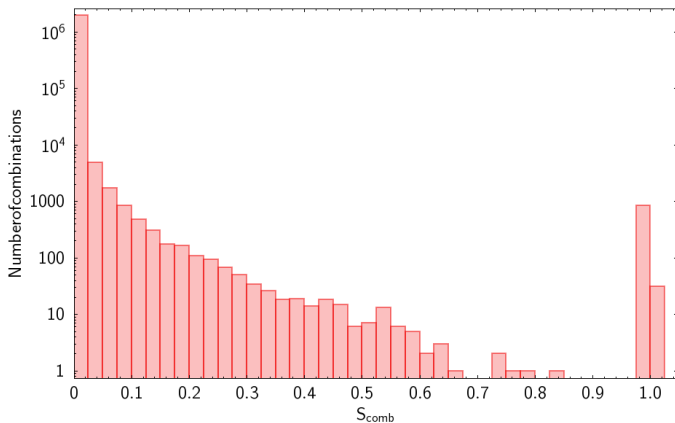


Fig. 12. Distribution of the combined score, S_{comb} .

$S_{\text{comb}} \approx 1$. Most of the combinations, however, have $S_{\text{comb}} \ll 1$, and sorting by this score can drastically reduce the number of combinations the user has to explore. The set of known lenses is limited in number, and thus the score combination is naturally biased due to the lack of coverage of the parameter space. Thus, it is expected that some yet-to-be-discovered lenses may have low S_{comb} values. We hence encourage users of this FPR to explore alternative selections.

The scores and discriminators we use to isolate the lens candidates are provided in Table 2. We concentrate our search on multiplets having $S_{\text{comb}} > 0.01$ but also consider each of the discriminators from Table 2 separately. Finally, for deeper cleaning, we cross-match the GravLens components with the *Gaia* DR3 in order to obtain information on proper motions, parallaxes, redshifts, and source classification; and with the CatWISE2020 catalogue (Marocco et al. 2021) to obtain W1-W2 colours. The use of these two public catalogues allows us to discard some obvious contaminants with large proper motions, large parallaxes, or low W1-W2 colours as well, as to select interesting candidates based on components with nearly equal redshifts or magnification biases (Turner 1980).

We finally selected 1 307 candidates from Table 2 using loose cuts on our discriminators so as to favour completeness. This selection consists in a compilation of various subsets that were independently drawn by the main authors of this paper and is consequently very heterogeneous. These candidates however share some common characteristics: $|b| > 5^\circ$, $W1-W2 > 0.275$, maximal component separation $< 6.5''$, $\text{gof} < 3$, $W_d < 6$ and $S_{\text{comb}} > 0.01$; although not all candidates satisfy all these characteristics at the same time. These candidates were then visually ranked from A to D, where A corresponds to the most promising candidates, where the lensing hypothesis is the most probable. Out of these candidates, 621 were ruled out (ranked D) because of one or more components exhibiting very large proper motions, large parallaxes, low W1-W2 WISE colours, or because they are spectroscopically confirmed as stars, nearby galaxies, or AGN. 305 candidates are given a rank of C, because the visual inspection tends to support the stars, QSO+star or QSO+galaxy hypothesis, or fortuitous alignment of QSOs. 332 candidates have interesting lens-like features and are classified as plausible candidates (rank B). Rank A is further subdivided into two subcategories: A+ if all components have similar spectra, image(s) that support the lensing hypothesis while exhibiting a potential deflector and are ranked A- otherwise. Rank B candidates are similarly split into B+ and B-, depending of the degree of confidence we put on the observed lens-like features. The 381 candidates A and B are presented in Table 3 (available online), highlighting the 49 candidates ranked A (see also Appendix B). The rank A candidates have angular sizes from $1.03''$ to $5.97''$, reaching minimal image separations of $0.41''$.

We note that depending on the involved redshifts, lensing galaxies, and image separations, the lensing galaxies can be hard to detect from the currently available ground-based imaging surveys. Thus, good candidates for lensed quasars can present no detectable lensing galaxy based on stamps from current ground-based survey archives, such as PS1. However, the lensing galaxy can later be identified in higher resolution and/or deeper images or via absorption lines directly in spatially unresolved, slit-based, follow-up spectra. Moreover, some effects can effectively bias the eye-detection of the lensing galaxy: first, we use a default color scale to display the DESI and PanSTARRS images in

Appendix B, while sharper cuts or a more detailed inspection of the individual g , r , i , z , y images can reveal hints of a lensing galaxy in several cases (e.g. DR3Gaia014718.509-465709.04 or DR3Gaia020209.884-431922.09). Secondly, for more compact lenses, the lensing galaxy is often blended with the lensed images, and the HESIOD method then reports a high score, likely due to a blue-red color gradient in the system that does not appear immediately by the eye (e.g. DR3Gaia115352.588-252027.70).

6. Conclusions

The *Gaia* satellite has all-sky coverage with an angular resolution of $\sim 0.18''$. This is unprecedented for an astronomical survey operating in optical wavelengths. In this article we describe the *Gaia* Focused Product Release (FPR) aimed at detecting strongly lensed quasars and the results of the DPAC *GravLens* processing. We developed novel methods to analyse the *Gaia* detections near quasars and produce a list of secondary sources that complement the current *Gaia* Data Releases. The methods produce a series of scores that can guide the user in the selection of promising new lensed quasar candidates.

A list of 3 760 480 quasar candidates from well-known catalogues (Sect. 2) was input to our *GravLens* pipeline. *GravLens* uses the DBSCAN unsupervised clustering algorithm to produce a list of sources within a $6''$ radius of each quasar. It identifies clusters of *Gaia* detections, referred to as components, around the quasar and labels anomalous ones as outliers. A list of point sources with mean positions, fluxes, and magnitudes of the components are computed and stored in the table `lens_candidates`. *GravLens* has analysed 183 368 062 transits around quasars obtained during the first three years of *Gaia* operations, and produced a catalogue of 4 760 920 sources of which $\sim 103\,000$ are new sources complementing those from *Gaia* DR3. 87% of the quasars were identified as single sources, while 501 385 resulted in multiplets (doublets or more).

We developed scoring methods to guide the selection of the best candidates for new lenses of different types, quads, and doubles. Two of these are the HESIOD score (Sect. 5.1), an outlier detection algorithm, and an Extremely Randomised Tree algorithm (ERT, Sect. 5.2). These methods use astrometric and photometric data. When available, *Gaia* spectrophotometry was used to ascertain whether a component was a probable image of the quasar (Sect. 5.3). The outlier detection methods were trained on real data from a set of known lenses, while the ERT method was trained on a large number ($\sim 10^5$) of simulated lenses. The methods are complementary as the ERT score works best for quads and triplets, whereas HESIOD is particularly effective for doublets. The scores accompany this Focused Product Release.

Finally, we use our scores complemented by visual inspection to derive a refined, non-exhaustive, list of 381 lensed quasar candidates, each assigned quality grades. Among these candidates, 49 are particularly promising.

The spatial resolution and all-sky coverage make *Gaia* data a treasure for lensing studies. This Focused Product Release provides a first list of new lens candidates and data beyond the *Gaia* DR3 to establish an all-sky catalogue of multiply-imaged quasars at the full *Gaia* angular resolution. We anticipate that the data products from this FPR and the upcoming *Gaia* Data Releases can contribute to various realms of cosmology. After identification and confirmation of lensed quasars through spectroscopic analysis, these lenses can help to progress on the elusive topics of dark matter and dark energy, and potentially offer

insights into the tension surrounding the determination of the Hubble constant.

Acknowledgements. We thank the anonymous referee for providing valuable comments that helped improve this paper. This work is part of the reduction of the *Gaia* satellite observations (<https://www.cosmos.esa.int/gaia>). The *Gaia* space mission is operated by the European Space Agency, and the data are being processed by the *Gaia* Data Processing and Analysis Consortium (DPAC, <https://www.cosmos.esa.int/web/gaia/dpac/consortium>). The *Gaia* archive website is <https://archives.esac.esa.int/gaia>. Funding for the DPAC is provided by national institutions, in particular, the institutions participating in the *Gaia* Multi-Lateral Agreement (MLA). We acknowledge the French "Centre National d'Etudes Spatiales" (CNES), the French national program PN-GRAM, and Action Spécifique *Gaia* as well as Observatoire Aquitain des Sciences de l'Univers (OASU) for financial support along the years. We also acknowledge funding from the Brazilian Fapesp institution as well as from the Brazilian-French co-operation institution CAPES/COFECUB. Our work was eased by the use of the data handling and visualisation software TOPCAT (Taylor 2005). This research has made use of the "Aladin sky atlas" developed at CDS, Strasbourg Observatory, France (Boch & Fernique 2014; Bonnarel et al. 2000). This research has made use of the VizieR catalogue access tool, CDS, Strasbourg, France. This research was eased by the use of The Pan-STARRS1 Surveys (PS1) and the Dark Energy Survey for a visual check of lens candidates.

References

- Agnello, A., Lin, H., Kuropatkin, N., et al. 2018, MNRAS, 479, 4345
 Arenou, F., Luri, X., Babusiaux, C., et al. 2018, A&A, 616, A17
 Arenou, F., Luri, X., Babusiaux, C., et al. 2017, A&A, 599, A50
 Assef, R. J., Stern, D., Noirot, G., et al. 2018, ApJS, 234, 23
 Bekker, J. & Davis, J. 2020, Mach. Learn., 109, 719–760
 Birrer, S., Amara, A., & Refregier, A. 2015, ApJ, 813, 102
 Boch, T. & Fernique, P. 2014, in Astronomical Society of the Pacific Conference Series, Vol. 485, Astronomical Data Analysis Software and Systems XXIII, ed. N. Manset & P. Forshay, 277
 Bonnarel, F., Fernique, P., Bienaymé, O., et al. 2000, A&AS, 143, 33
 Breiman, L. 2001, Machine Learning, 45, 5–32
 Chambers, K. C., Magnier, E. A., Metcalfe, N., et al. 2016, arXiv e-prints, arXiv:1612.05560
 Chen, G. C. F., Fassnacht, C. D., Suyu, S. H., et al. 2019, MNRAS, 490, 1743
 Cortes, D. 2019, arXiv e-prints, arXiv:1911.06646
 Cortes, D. 2021, arXiv e-prints, arXiv:2110.13402
 Courbin, F., Eigenbrod, A., Vuissoz, C., Meylan, G., & Magain, P. 2005, in Gravitational Lensing Impact on Cosmology, ed. Y. Mellier & G. Meylan, Vol. 225, 297–303
 De Angeli, F., Weiler, M., Montegriffo, P., et al. 2023, A&A, 674, A2
 de Bruijne, J. H. J., Allen, M., Azaz, S., et al. 2015, A&A, 576, A74
 de Mendoza y Ríos, J. 1795, Memoria sobre algunos metodos nuevos de calcular la longitud por las distancias lunares y explicaciones prácticas de una teoría para la solución de otros problemas de navegación (Imp. Real de Madrid)
 de Souza, R. E., Krone-Martins, A., dos Anjos, S., Ducourant, C., & Teixeira, R. 2014, A&A, 568, A124
 Delchambre, L., Krone-Martins, A., Wertz, O., et al. 2019, A&A, 622, A165
 Desira, C., Shu, Y., Auger, M. W., et al. 2022, MNRAS, 509, 738
 Dey, A., Schlegel, D. J., Lang, D., et al. 2019, AJ, 157, 168
 Di Valentino, E., Mena, O., Pan, S., et al. 2021, Classical and Quantum Gravity, 38, 153001
 Diaz Rivero, A., Cyr-Racine, F.-Y., & Dvorkin, C. 2018, Phys. Rev. D, 97, 023001
 Ducourant, C., Krone-Martins, A., Galluccio, L., et al. 2023, A&A, 674, A11
 Ducourant, C., Teixeira, R., Krone-Martins, A., et al. 2017, A&A, 597, A90
 Ducourant, C., Wertz, O., Krone-Martins, A., et al. 2018, A&A, 618, A56
 Eisenhardt, P. R. M., Marocco, F., Fowler, J. W., et al. 2020, ApJS, 247, 69
 Elkan, C. & Noto, K. 2008, in Proceedings of the 14th ACM SIGKDD International Conference on Knowledge Discovery and Data Mining, KDD '08 (New York, NY, USA: Association for Computing Machinery), 213–220
 Ester, M., Kriegel, H.-P., Sander, J., & Xu, X. 1996, in Proceedings of the Second International Conference on Knowledge Discovery and Data Mining, KDD'96 (AAAI Press), 226–231
 Euclid Collaboration, Scaramella, R., Amiaux, J., et al. 2022, A&A, 662, A112
 Fabricius, C., Bastian, U., Portell, J., et al. 2016, A&A, 595, A3
 Fabricius, C., Luri, X., Arenou, F., et al. 2021, A&A, 649, A5
 Finet, F. & Surdej, J. 2016, A&A, 590, A42
 Flesch, E. W. 2019, arXiv e-prints, arXiv:1912.05614
 Flesch, E. W. 2021, arXiv e-prints, arXiv:2105.12985
 Gaia Collaboration, Bailer-Jones, C. A. L., Teysier, D., et al. 2023a, A&A, 674, A41

Table 2. Extract of the table containing 1 957 559 combinations of 2–6 components out of the 491 504 multiplets including the scores calculated in this work. All combinations of components from the multiplets are considered here to enable the detection of cases consisting of multiple images of a lens system, plus contaminants (e.g. deflecting galaxy or nearby star). Comp. are the component_id's (from Table A.1) of the components in each combination.

#	name	Comp.	α	δ	P_{ert}	θ_{min}	gof	W_d	S_{comb}
1	DR3Gaia052025.426+331443.46	1/2	80.1057322	33.2448383		0.615	-2.770	2.448	0.000
2	DR3Gaia084114.124+223614.72	1/2	130.3082652	22.6042005		0.521	-3.070	3.035	0.000
3	DR3Gaia102800.048+803922.91	1/2	157.0020369	80.6567414		0.628	0.577	4.126	0.000
4	DR3Gaia235819.841+482027.63	1/2	359.5817555	48.3413855			0.597	5.803	0.000
5	DR3Gaia192635.516+405005.98	1/2	291.6473954	40.8348653		0.642	1.247	4.707	0.000
6	DR3Gaia062751.407-253223.83	1/2	96.9646288	-25.5393739		0.374	6.391	4.224	0.000
7	DR3Gaia062751.407-253223.83	1/3	96.9642328	-25.5398715			5.097	4.224	0.000
8	DR3Gaia062751.407-253223.83	2/3	96.9638001	-25.5404539		0.374	1.278	4.224	0.000
9	DR3Gaia062751.407-253223.83	1/2/3	96.9642205	-25.5398998	0.060	0.374	5.646	4.224	0.000
10	DR3Gaia191906.417-110304.27	1/2	289.7765560	-11.0504709			0.377	21.999	0.000
⋮	⋮	⋮	⋮	⋮	⋮	⋮	⋮	⋮	⋮
1957557	DR3Gaia190225.249-311341.45	2/3/4	285.6043694	-31.2287627	0.580	0.705	-3.967	2.688	0.000
1957558	DR3Gaia190225.249-311341.45	1/2/3/4	285.6046004	-31.2289471	0.000	0.705	5.939	131.139	0.000
1957559	DR3Gaia201938.091-142206.89	1/2	304.9092924	-14.3684893		0.759	3.843	1.984	0.000

Notes. The full table is available at the CDS in electronic form via anonymous ftp to [cdsarc.u-strasbg.fr](ftp://cdsarc.u-strasbg.fr) (130.79.128.5) or via <http://cdsarc.u-strasbg.fr/viz-bin/qcat?J/A+A/???/???>.

- Gaia Collaboration, Brown, A. G. A., Vallenari, A., et al. 2018, *A&A*, 616, A1
Gaia Collaboration, Brown, A. G. A., Vallenari, A., et al. 2021, *A&A*, 649, A1
Gaia Collaboration, Prusti, T., de Bruijne, J. H. J., et al. 2016, *A&A*, 595, A1
Gaia Collaboration, Vallenari, A., Brown, A. G. A., et al. 2023b, *A&A*, 674, A1
Geurts, P., Ernst, D., & Wehenkel, L. 2006, *Machine Learning*, 63, 3
Gilman, D., Birrer, S., Nierenberg, A., et al. 2020a, *MNRAS*, 491, 6077
Gilman, D., Bovy, J., Treu, T., et al. 2021, *MNRAS*, 507, 2432
Gilman, D., Du, X., Benson, A., et al. 2020b, *MNRAS*, 492, L12
Gordon, K. D., Clayton, G. C., Misselt, K. A., Landolt, A. U., & Wolff, M. J. 2003, *ApJ*, 594, 279
Green, G. M., Schlafly, E., Zucker, C., Speagle, J. S., & Finkbeiner, D. 2019, *ApJ*, 887, 93
Harris, W. E. 2010, arXiv e-prints, arXiv:1012.3224
Holder, G. P. & Schechter, P. L. 2003, *ApJ*, 589, 688
Huchra, J., Gorenstein, M., Kent, S., et al. 1985, *AJ*, 90, 691
Kantorovich, L. V. 1942, *Doklady Akademii Nauk SSSR*, 37, 227–229
Kantorovich, L. V. 2006, *Journal of Mathematical Sciences (English translation)*, 133, 1381
Keeton, C. R. 2001, arXiv e-prints [arXiv:astro-ph/0102341]
Kormann, R., Schneider, P., & Bartelmann, M. 1994, *A&A*, 284, 285
Krone-Martins, A., Delchambre, L., Wertz, O., et al. 2018, *A&A*, 616, L11
Krone-Martins, A., Ducourant, C., Teixeira, R., et al. 2013, *A&A*, 556, A102
Krone-Martins, A., Graham, M. J., Stern, D., et al. 2019, arXiv e-prints, arXiv:1912.08977
Krone-Martins, A., Gravras, P., Ducourant, C., et al. 2022, submitted to *Astronomy&Astrophysics*
Krone-Martins, A. & Moitinho, A. 2014, *A&A*, 561, A57
Lallement, R., Capitanio, L., Ruiz-Dern, L., et al. 2018, *A&A*, 616, A132
Lang, D. 2014, *AJ*, 147, 108
Laureijs, R., Amiaux, J., Arduini, S., et al. 2011, arXiv e-prints, arXiv:1110.3193
Leike, R., Celli, S., Krone-Martins, A., et al. 2021, *Nature Astronomy*, 5, 832
Leike, R. H., Edenhofer, G., Knollmüller, J., et al. 2022, arXiv e-prints, arXiv:2204.11715
Lemon, C., Anguita, T., Auger-Williams, M. W., et al. 2023, *MNRAS*, 520, 3305
Lemon, C. A., Auger, M. W., & McMahon, R. G. 2019, *MNRAS*, 483, 4242
Lemon, C. A., Auger, M. W., McMahon, R. G., & Ostrovski, F. 2018, *MNRAS*, 479, 5060
Li, R., Frenk, C. S., Cole, S., Wang, Q., & Gao, L. 2017, *MNRAS*, 468, 1426
Linder, E. V. 2004, *Phys. Rev. D*, 70, 043534
Linder, E. V. 2011, *Phys. Rev. D*, 84, 123529
Liu, B., Li, Z., & Zhu, Z.-H. 2019, *MNRAS*, 487, 1980
Liu, F. T., Ting, K. M., & Zhou, Z.-H. 2008, in 2008 Eighth IEEE International Conference on Data Mining, 413–422
Liu, F. T., Ting, K. M., & Zhou, Z.-H. 2010, in *Machine Learning and Knowledge Discovery in Databases*, ed. J. L. Balcázar, F. Bonchi, A. Gionis, & M. Sebag (Berlin, Heidelberg: Springer Berlin Heidelberg), 274–290
Lucey, J. R., Schechter, P. L., Smith, R. J., & Anguita, T. 2018, *MNRAS*, 476, 927
Mannucci, F., Pancino, E., Belfiore, F., et al. 2022, *Nature Astronomy*, 6, 1185
Marocco, F., Eisenhardt, P. R. M., Fowler, J. W., et al. 2021, *ApJS*, 253, 8
Millon, M., Courbin, F., Bonvin, V., et al. 2020, *A&A*, 640, A105
Minor, Q., Kaplinghat, M., Chan, T. H., & Simon, E. 2021, *MNRAS*, 507, 1202
Montegriffo, P., De Angeli, F., Andrae, R., et al. 2023, *A&A*, 674, A3
Nierenberg, A. M., Gilman, D., Treu, T., et al. 2020, *MNRAS*, 492, 5314
Nierenberg, A. M., Treu, T., Brammer, G., et al. 2017, *MNRAS*, 471, 2224
Oguri, M., Inada, N., Strauss, M. A., et al. 2012, *AJ*, 143, 120
Petit, Q., Ducourant, C., Slezak, E., Sluse, D., & Delchambre, L. 2023, *A&A*, 669, A132
Peyré, G. & Cuturi, M. 2019, *Foundations and Trends in Machine Learning*, 51, 1
Refsdal, S. 1964, *MNRAS*, 128, 307
Riello, M., De Angeli, F., Evans, D. W., et al. 2018, *A&A*, 616, A3
Robin, A. C., Luri, X., Reylé, C., et al. 2012, *A&A*, 543, A100
Shu, Y., Kposov, S. E., Evans, N. W., et al. 2019, *MNRAS*, 489, 4741
Stekhoven, D. J. & Bühlmann, P. 2011, *Bioinformatics*, 28, 112
Stern, D., Djorgovski, S. G., Krone-Martins, A., et al. 2021, *ApJ*, 921, 42
Surdej, J., Claeskens, J.-F., & Smette, A. 2002, *GAIA Relativity and Reference Frame WG meeting*
Suyu, S. H., Bonvin, V., Courbin, F., et al. 2017, *MNRAS*, 468, 2590
Taylor, M. B. 2005, in *Astronomical Society of the Pacific Conference Series*, Vol. 347, *Astronomical Data Analysis Software and Systems XIV*, ed. P. Shopbell, M. Britton, & R. Ebert, 29
Torra, F., Castañeda, J., Fabricius, C., et al. 2021, *A&A*, 649, A10
Treu, T., Suyu, S. H., & Marshall, P. J. 2022, *A&A Rev.*, 30, 8
Turner, E. L. 1980, *ApJ*, 242, L135
van Buuren, S. 2007, *Statistical Methods in Medical Research*, 16, 219, PMID: 17621469
Verde, L., Treu, T., & Riess, A. G. 2019, *Nature Astronomy*, 3, 891
Villani, C. 2003, *Topics in Optimal Transportation*, *Graduate Studies in Mathematics Series* (American Mathematical Society)
Villani, C. 2016, *Optimal Transport: Old and New*, *Grundlehren der mathematischen Wissenschaften* (Springer Berlin Heidelberg)
Wang, L.-F., Zhang, J.-H., He, D.-Z., Zhang, J.-F., & Zhang, X. 2022, *MNRAS*, 514, 1433
Wertz, O., Stern, D., Krone-Martins, A., et al. 2019, *A&A*, 628, A17
Whitmore, B. C., Allam, S. S., Budavári, T., et al. 2016, *AJ*, 151, 134
Wilson, E. B. & Hilferty, M. M. 1931, *Proceedings of the National Academy of Sciences*, 17, 684
Wilson, S. 2021, miceRanger: Multiple Imputation by Chained Equations with Random Forests, r package version 1.5.0
Wolpert, D. & Macready, W. 1997, *IEEE Transactions on Evolutionary Computation*, 1, 67
Wolpert, D. H. 1996, *Neural Computation*, 8, 1341
Wong, K. C., Suyu, S. H., Chen, G. C. F., et al. 2020, *MNRAS*, 498, 1420
Xia, J.-Q., Yu, H., Wang, G.-J., et al. 2017, *ApJ*, 834, 75

Table 3. List of the most promising 49 lens candidates out of the 381 selected in this work (the full is available online). Candidates with P_{ert} are quad candidates, others are double candidates. The resampled spectra and Dark Energy Survey or Pan-STARRS1 images for this selection can be found in Appendix B. The candidate identifier (#) corresponds to the row identifier from Table 2.

#	name	grade	α	δ	P_{ert}	\mathcal{O}_{min}	gof	W_d	S_{comb}
1186594	DR3Gaia010120.807-494324.36	A+	15.3367775	-49.7228775		0.739	1.062	1.194	0.000
1410355	DR3Gaia015426.227-440213.66	A+	28.6086993	-44.0372670		0.844	-1.701	1.501	0.003
1209020	DR3Gaia015739.213-683707.60	A+	29.4137683	-68.6187615		1.000	-1.220	2.797	0.178
482036	DR3Gaia020209.884-431922.09	A+	30.5410743	-43.3235545			-0.477	0.540	0.000
400875	DR3Gaia020501.994-323348.59	A+	31.2589438	-32.5640445			-1.904	0.189	0.000
506340	DR3Gaia044652.260-310219.85	A+	71.7179854	-31.0383946		1.000	-0.963	2.369	0.003
748543	DR3Gaia050613.596-253047.45	A+	76.5561851	-25.5134752		0.621	-0.623	0.955	0.000
1879078	DR3Gaia060216.151-433540.97	A+	90.5670711	-43.5945222		0.866	5.328	3.712	0.004
50830	DR3Gaia105221.613-195238.39	A+	163.0900708	-19.8771667		0.754	8.572	7.774	0.088
1572115	DR3Gaia121504.295-200556.84	A+	183.7681509	-20.0992440		0.997	-0.912	4.616	0.153
48388	DR3Gaia151030.678-791857.87	A+	227.6266420	-79.3157777		0.521	-3.740	1.952	0.000
1734022	DR3Gaia151723.117-241848.13	A+	229.3462903	-24.3139543		0.796	-2.028	4.264	0.002
147896	DR3Gaia170842.333+064614.31	A+	257.1758007	6.7705216		0.679	-2.583	4.762	0.000
1654705	DR3Gaia172201.867+201920.75	A+	260.5075498	20.3222709	0.740	0.391	-2.150 ^a	5.784 ^a	0.000
294425	DR3Gaia193647.137-320217.79	A+	294.1957241	-32.0385626		0.833	-2.110	1.282	0.000
602038	DR3Gaia210752.320-161131.67	A+	316.9684944	-16.1922981	0.880	0.782	1.747 ^b	4.827 ^b	0.003
1466139	DR3Gaia221540.110-520404.66	A+	333.9167767	-52.0676474		0.998	0.143	0.877	0.176
700931	DR3Gaia230405.819-802805.72	A+	346.0281735	-80.4686247			-0.419	1.415	0.000
141767	DR3Gaia014718.509-465709.04	A-	26.8266523	-46.9530303		0.799	-0.124	1.573	0.000
884711	DR3Gaia021120.383+210749.64	A-	32.8343751	21.1299320	0.090	0.634	0.474 ^c	3.008 ^c	0.000
559412	DR3Gaia031013.747+352414.86	A-	47.5561827	35.4045044	0.320	0.278	-2.067 ^d	4.703 ^d	0.000
1002146	DR3Gaia033001.688-441335.60	A-	52.5063646	-44.2268054		0.675	1.658	1.575	0.000
9023	DR3Gaia045755.331+124238.67	A-	74.4805842	12.7104176		0.603	-2.458	1.522	0.000
1420154	DR3Gaia055409.442-234754.13	A-	88.5387470	-23.7982264		0.610	3.493	1.395	0.000
771791	DR3Gaia070020.352+132813.68	A-	105.0851179	13.4707837		0.458	-1.776	2.121	0.000
1113851	DR3Gaia092321.265-020554.21	A-	140.8399647	-2.0980878			-4.474	3.419	0.023
496839	DR3Gaia110527.117-391343.61	A-	166.3628841	-39.2284930		1.000	-2.382	1.397	0.122
287077	DR3Gaia111221.158-201111.55	A-	168.0885649	-20.1865341		0.600	-1.452	1.381	0.010
1204565	DR3Gaia114934.110-172651.95	A-	177.3923073	-17.4478355		0.709	1.989	4.780	0.036
1147299	DR3Gaia115352.588-252027.70	A-	178.4693002	-25.3410790		0.747	2.111	2.093	0.051
13466	DR3Gaia124708.184-092332.50	A-	191.7842239	-9.3921238		0.793	-0.925	6.682	0.057
399786	DR3Gaia125238.119-270906.98	A-	193.1589992	-27.1514771		0.503	1.112	1.845	0.000
1938680	DR3Gaia133741.153-132524.24	A-	204.4217226	-13.4235215		0.630	0.855	6.103	0.029
950559	DR3Gaia134839.786+002343.29	A-	207.1655325	0.3946152			-3.192	3.462	0.000
787035	DR3Gaia150826.916+670544.68	A-	227.1123665	67.0955375		0.469	-0.758	2.561	0.023
468388	DR3Gaia160508.549+024739.44	A-	241.2857807	2.7943234		0.779	-1.242	3.677	0.052
651231	DR3Gaia161135.764+515346.43	A-	242.8993897	51.8965852		0.766	0.509	12.918	0.019
726741	DR3Gaia173144.453+250232.26	A-	262.9352928	25.0424432		0.639	1.918	5.289	0.026
1741359	DR3Gaia175323.439+144702.74	A-	268.3482034	14.7845840	0.280	0.587	-2.918 ^e	3.794 ^e	0.000
675406	DR3Gaia180734.677+475943.60	A-	271.8948565	47.9953497		1.000			0.021
820377	DR3Gaia190007.256-624734.16	A-	285.0303752	-62.7924480		0.822	-0.214	22.185	0.001
1157981	DR3Gaia201951.245-062931.96	A-	304.9638007	-6.4925101		0.367	1.034	1.331	0.000
628816	DR3Gaia202042.974-265023.86	A-	305.1794142	-26.8399389		0.780	6.270	2.452	0.009
173950	DR3Gaia202627.737+161850.69	A-	306.6157010	16.3144130		0.595	-1.076	3.107	0.000
1381292	DR3Gaia202710.607+060438.30	A-	306.7943588	6.0773550		0.650	-0.260	2.325	0.033
937383	DR3Gaia204449.725-040357.87	A-	311.2067405	-4.0665789		0.441	-1.300	0.831	0.000
1401461	DR3Gaia220231.754-800425.40	A-	330.6355963	-80.0735089		0.696	0.181	0.633	0.000
1557618	DR3Gaia222638.124-521519.18	A-	336.6584846	-52.2557299		0.518	2.052	1.633	0.000
379838	DR3Gaia235506.238-455335.44	A-	358.7762969	-45.8929542		0.469	-1.552	3.957	0.001

Notes. ^(a) Taken from components 1 and 2 of DR3Gaia172201.867+201920.75 (#1654702). ^(b) Taken from components 1 and 2 of DR3Gaia210752.320-161131.67 (#602035). ^(c) Taken from components 1 and 2 of DR3Gaia021120.383+210749.64 (#884708). ^(d) Taken from components 1 and 3 of DR3Gaia031013.747+352414.86 (#559410). ^(e) Taken from components 2 and 3 of DR3Gaia175323.439+144702.74 (#1741358). The full table is available at the CDS in electronic form via anonymous ftp to [cdsarc.u-strasbg.fr](https://cdsarc.u-strasbg.fr/viz-bin/qcat?J/A+A/???/???) (130.79.128.5) or via [http://cdsarc.u-strasbg.fr/viz-bin/qcat?J/A+A/???/???.](http://cdsarc.u-strasbg.fr/viz-bin/qcat?J/A+A/???/???)

³ Laboratoire d’astrophysique de Bordeaux, Univ. Bordeaux, CNRS, B18N, allée Geoffroy Saint-Hilaire, 33615 Pessac, France

¹ Donald Bren School of Information and Computer Sciences, University of California, Irvine, CA 92697, USA

² CENTRA, Faculdade de Ciências, Universidade de Lisboa, Edif. C8, Campo Grande, 1749-016 Lisboa, Portugal

⁴ Université Côte d’Azur, Observatoire de la Côte d’Azur, CNRS, Laboratoire Lagrange, Bd de l’Observatoire, CS 34229, 06304 Nice Cedex 4, France

- 5 Institut d'Astrophysique et de Géophysique, Université de Liège, 19c, Allée du 6 Août, B-4000 Liège, Belgium
- 6 Instituto de Astronomia, Geofísica e Ciências Atmosféricas, Universidade de São Paulo, Rua do Matão, 1226, Cidade Universitária, 05508-900 São Paulo, SP, Brazil
- 7 CNES Centre Spatial de Toulouse, 18 avenue Edouard Belin, 31401 Toulouse Cedex 9, France
- 8 ATOS for CNES Centre Spatial de Toulouse, 18 avenue Edouard Belin, 31401 Toulouse Cedex 9, France
- 9 Leiden Observatory, Leiden University, Niels Bohrweg 2, 2333 CA Leiden, The Netherlands
- 10 INAF - Osservatorio astronomico di Padova, Vicolo Osservatorio 5, 35122 Padova, Italy
- 11 European Space Agency (ESA), European Space Research and Technology Centre (ESTEC), Keplerlaan 1, 2201AZ, Noordwijk, The Netherlands
- 12 GEPI, Observatoire de Paris, Université PSL, CNRS, 5 Place Jules Janssen, 92190 Meudon, France
- 13 Univ. Grenoble Alpes, CNRS, IPAG, 38000 Grenoble, France
- 14 Astronomisches Rechen-Institut, Zentrum für Astronomie der Universität Heidelberg, Mönchhofstr. 12-14, 69120 Heidelberg, Germany
- 15 Institute of Astronomy, University of Cambridge, Madingley Road, Cambridge CB3 0HA, United Kingdom
- 16 Department of Astronomy, University of Geneva, Chemin Pegasi 51, 1290 Versoix, Switzerland
- 17 European Space Agency (ESA), European Space Astronomy Centre (ESAC), Camino bajo del Castillo, s/n, Urbanización Villafranca del Castillo, Villanueva de la Cañada, 28692 Madrid, Spain
- 18 Aurora Technology for European Space Agency (ESA), Camino bajo del Castillo, s/n, Urbanización Villafranca del Castillo, Villanueva de la Cañada, 28692 Madrid, Spain
- 19 Institut de Ciències del Cosmos (ICCUB), Universitat de Barcelona (UB), Martí i Franquès 1, 08028 Barcelona, Spain
- 20 Departament de Física Quàntica i Astrofísica (FQA), Universitat de Barcelona (UB), c. Martí i Franquès 1, 08028 Barcelona, Spain
- 21 Institut d'Estudis Espacials de Catalunya (IEEC), c. Gran Capità, 2-4, 08034 Barcelona, Spain
- 22 Lohrmann Observatory, Technische Universität Dresden, Mommsenstraße 13, 01062 Dresden, Germany
- 23 Lund Observatory, Division of Astrophysics, Department of Physics, Lund University, Box 43, 22100 Lund, Sweden
- 24 INAF - Osservatorio Astrofisico di Arcetri, Largo Enrico Fermi 5, 50125 Firenze, Italy
- 25 Nicolaus Copernicus Astronomical Center, Polish Academy of Sciences, ul. Bartycka 18, 00-716 Warsaw, Poland
- 26 Max Planck Institute for Astronomy, Königstuhl 17, 69117 Heidelberg, Germany
- 27 Mullard Space Science Laboratory, University College London, Holmbury St Mary, Dorking, Surrey RH5 6NT, United Kingdom
- 28 INAF - Osservatorio Astrofisico di Torino, via Osservatorio 20, 10025 Pino Torinese (TO), Italy
- 29 Department of Astronomy, University of Geneva, Chemin d'Ecogia 16, 1290 Versoix, Switzerland
- 30 Royal Observatory of Belgium, Ringlaan 3, 1180 Brussels, Belgium
- 31 DAPCOM Data Services, c. dels Vilabella, 5-7, 80500 Vic, Barcelona, Spain
- 32 ALTEC S.p.a. Corso Marche, 79, 10146 Torino, Italy
- 33 Sednai Sàrl, Geneva, Switzerland
- 34 Gaia DPAC Project Office, ESAC, Camino bajo del Castillo, s/n, Urbanización Villafranca del Castillo, Villanueva de la Cañada, 28692 Madrid, Spain
- 35 Telespazio UK S.L. for European Space Agency (ESA), Camino bajo del Castillo, s/n, Urbanización Villafranca del Castillo, Villanueva de la Cañada, 28692 Madrid, Spain
- 36 SYRTE, Observatoire de Paris, Université PSL, CNRS, Sorbonne Université, LNE, 61 avenue de l'Observatoire 75014 Paris, France
- 37 IMCCE, Observatoire de Paris, Université PSL, CNRS, Sorbonne Université, Univ. Lille, 77 av. Denfert-Rochereau, 75014 Paris, France
- 38 Serco Gestión de Negocios for European Space Agency (ESA), Camino bajo del Castillo, s/n, Urbanización Villafranca del Castillo, Villanueva de la Cañada, 28692 Madrid, Spain
- 39 INAF - Osservatorio di Astrofisica e Scienza dello Spazio di Bologna, via Piero Gobetti 93/3, 40129 Bologna, Italy
- 40 CRAAG - Centre de Recherche en Astronomie, Astrophysique et Géophysique, Route de l'Observatoire Bp 63 Bouzareah 16340 Algiers, Algeria
- 41 Institute for Astronomy, University of Edinburgh, Royal Observatory, Blackford Hill, Edinburgh EH9 3HJ, United Kingdom
- 42 RHEA for European Space Agency (ESA), Camino bajo del Castillo, s/n, Urbanización Villafranca del Castillo, Villanueva de la Cañada, 28692 Madrid, Spain
- 43 CIGUS CITIC - Department of Computer Science and Information Technologies, University of A Coruña, Campus de Elviña s/n, A Coruña, 15071, Spain
- 44 ATG Europe for European Space Agency (ESA), Camino bajo del Castillo, s/n, Urbanización Villafranca del Castillo, Villanueva de la Cañada, 28692 Madrid, Spain
- 45 Kavli Institute for Cosmology Cambridge, Institute of Astronomy, Madingley Road, Cambridge, CB3 0HA
- 46 Department of Astrophysics, Astronomy and Mechanics, National and Kapodistrian University of Athens, Panepistimiopolis, Zografos, 15783 Athens, Greece
- 47 INAF - Osservatorio Astrofisico di Catania, via S. Sofia 78, 95123 Catania, Italy
- 48 Dipartimento di Fisica e Astronomia "Ettore Majorana", Università di Catania, Via S. Sofia 64, 95123 Catania, Italy
- 49 Université de Strasbourg, CNRS, Observatoire astronomique de Strasbourg, UMR 7550, 11 rue de l'Université, 67000 Strasbourg, France
- 50 INAF - Osservatorio Astronomico di Roma, Via Frascati 33, 00078 Monte Porzio Catone (Roma), Italy
- 51 Space Science Data Center - ASI, Via del Politecnico SNC, 00133 Roma, Italy
- 52 Department of Physics, University of Helsinki, P.O. Box 64, 00014 Helsinki, Finland
- 53 Finnish Geospatial Research Institute FGI, Vuorimiehentie 5, 02150 Espoo, Finland
- 54 Institut UTINAM CNRS UMR6213, Université de Franche-Comté, OSU THETA Franche-Comté Bourgogne, Observatoire de Besançon, BP1615, 25010 Besançon Cedex, France
- 55 HE Space Operations BV for European Space Agency (ESA), Keplerlaan 1, 2201AZ, Noordwijk, The Netherlands
- 56 Dpto. de Inteligencia Artificial, UNED, c/ Juan del Rosal 16, 28040 Madrid, Spain
- 57 Institut d'Astronomie et d'Astrophysique, Université Libre de Bruxelles CP 226, Boulevard du Triomphe, 1050 Brussels, Belgium
- 58 Leibniz Institute for Astrophysics Potsdam (AIP), An der Sternwarte 16, 14482 Potsdam, Germany
- 59 Konkoly Observatory, Research Centre for Astronomy and Earth Sciences, Eötvös Loránd Research Network (ELKH), MTA Centre of Excellence, Konkoly Thege Miklós út 15-17, 1121 Budapest, Hungary
- 60 ELTE Eötvös Loránd University, Institute of Physics, 1117, Pázmány Péter sétány 1A, Budapest, Hungary
- 61 Instituut voor Sterrenkunde, KU Leuven, Celestijnenlaan 200D, 3001 Leuven, Belgium
- 62 Department of Astrophysics/IMAPP, Radboud University, P.O.Box 9010, 6500 GL Nijmegen, The Netherlands
- 63 University of Vienna, Department of Astrophysics, Türkenschanzstraße 17, A1180 Vienna, Austria
- 64 Institute of Physics, Ecole Polytechnique Fédérale de Lausanne (EPFL), Observatoire de Sauverny, 1290 Versoix, Switzerland
- 65 Quasar Science Resources for European Space Agency (ESA), Camino bajo del Castillo, s/n, Urbanización Villafranca del Castillo, Villanueva de la Cañada, 28692 Madrid, Spain

- ⁶⁶ LASIGE, Faculdade de Ciências, Universidade de Lisboa, Edif. C6, Campo Grande, 1749-016 Lisboa, Portugal
- ⁶⁷ School of Physics and Astronomy, University of Leicester, University Road, Leicester LE1 7RH, United Kingdom
- ⁶⁸ School of Physics and Astronomy, Tel Aviv University, Tel Aviv 6997801, Israel
- ⁶⁹ Cavendish Laboratory, JJ Thomson Avenue, Cambridge CB3 0HE, United Kingdom
- ⁷⁰ Telespazio for CNES Centre Spatial de Toulouse, 18 avenue Edouard Belin, 31401 Toulouse Cedex 9, France
- ⁷¹ National Observatory of Athens, I. Metaxa and Vas. Pavlou, Palaia Penteli, 15236 Athens, Greece
- ⁷² University of Turin, Department of Physics, Via Pietro Giuria 1, 10125 Torino, Italy
- ⁷³ Depto. Estadística e Investigación Operativa. Universidad de Cádiz, Avda. República Saharaui s/n, 11510 Puerto Real, Cádiz, Spain
- ⁷⁴ EURIX S.r.l., Corso Vittorio Emanuele II 61, 10128, Torino, Italy
- ⁷⁵ Porter School of the Environment and Earth Sciences, Tel Aviv University, Tel Aviv 6997801, Israel
- ⁷⁶ HE Space Operations BV for European Space Agency (ESA), Camino bajo del Castillo, s/n, Urbanización Villafranca del Castillo, Villanueva de la Cañada, 28692 Madrid, Spain
- ⁷⁷ LFCA/DAS, Universidad de Chile, CNRS, Casilla 36-D, Santiago, Chile
- ⁷⁸ SISSA - Scuola Internazionale Superiore di Studi Avanzati, via Bonomea 265, 34136 Trieste, Italy
- ⁷⁹ University of Turin, Department of Computer Sciences, Corso Svizzera 185, 10149 Torino, Italy
- ⁸⁰ Thales Services for CNES Centre Spatial de Toulouse, 18 avenue Edouard Belin, 31401 Toulouse Cedex 9, France
- ⁸¹ Dpto. de Matemática Aplicada y Ciencias de la Computación, Univ. de Cantabria, ETS Ingenieros de Caminos, Canales y Puertos, Avda. de los Castros s/n, 39005 Santander, Spain
- ⁸² Institut de Física d'Altes Energies (IFAE), The Barcelona Institute of Science and Technology, Campus UAB, 08193 Bellaterra (Barcelona), Spain
- ⁸³ Port d'Informació Científica (PIC), Campus UAB, C. Albareda s/n, 08193 Bellaterra (Barcelona), Spain
- ⁸⁴ Instituto de Astrofísica, Universidad Andres Bello, Fernandez Concha 700, Las Condes, Santiago RM, Chile
- ⁸⁵ Centre for Astrophysics Research, University of Hertfordshire, College Lane, AL10 9AB, Hatfield, United Kingdom
- ⁸⁶ University of Turin, Mathematical Department "G. Peano", Via Carlo Alberto 10, 10123 Torino, Italy
- ⁸⁷ INAF - Osservatorio Astronomico d'Abruzzo, Via Mentore Maggini, 64100 Teramo, Italy
- ⁸⁸ Mésocentre de calcul de Franche-Comté, Université de Franche-Comté, 16 route de Gray, 25030 Besançon Cedex, France
- ⁸⁹ Ruđer Bošković Institute, Bijenička cesta 54, 10000 Zagreb, Croatia
- ⁹⁰ Astrophysics Research Centre, School of Mathematics and Physics, Queen's University Belfast, Belfast BT7 1NN, UK
- ⁹¹ Data Science and Big Data Lab, Pablo de Olavide University, 41013, Seville, Spain
- ⁹² Institute of Astrophysics, FORTH, Crete, Greece
- ⁹³ Barcelona Supercomputing Center (BSC), Plaça Eusebi Güell 1-3, 08034-Barcelona, Spain
- ⁹⁴ ETSE Telecomunicación, Universidade de Vigo, Campus Lagoas-Marcosende, 36310 Vigo, Galicia, Spain
- ⁹⁵ F.R.S.-FNRS, Rue d'Egmont 5, 1000 Brussels, Belgium
- ⁹⁶ Asteroid Engineering Laboratory, Luleå University of Technology, Box 848, S-981 28 Kiruna, Sweden
- ⁹⁷ Kapteyn Astronomical Institute, University of Groningen, Landleven 12, 9747 AD Groningen, The Netherlands
- ⁹⁸ IAC - Instituto de Astrofísica de Canarias, Via Láctea s/n, 38200 La Laguna S.C., Tenerife, Spain
- ⁹⁹ Department of Astrophysics, University of La Laguna, Via Láctea s/n, 38200 La Laguna S.C., Tenerife, Spain
- ¹⁰⁰ Astronomical Observatory, University of Warsaw, Al. Ujazdowskie 4, 00-478 Warszawa, Poland
- ¹⁰¹ Research School of Astronomy & Astrophysics, Australian National University, Cotter Road, Weston, ACT 2611, Australia
- ¹⁰² European Space Agency (ESA, retired), European Space Research and Technology Centre (ESTEC), Keplerlaan 1, 2201AZ, Noordwijk, The Netherlands
- ¹⁰³ LESIA, Observatoire de Paris, Université PSL, CNRS, Sorbonne Université, Université de Paris, 5 Place Jules Janssen, 92190 Meudon, France
- ¹⁰⁴ Université Rennes, CNRS, IPR (Institut de Physique de Rennes) - UMR 6251, 35000 Rennes, France
- ¹⁰⁵ INAF - Osservatorio Astronomico di Capodimonte, Via Moiriello 16, 80131, Napoli, Italy
- ¹⁰⁶ Shanghai Astronomical Observatory, Chinese Academy of Sciences, 80 Nandan Road, Shanghai 200030, People's Republic of China
- ¹⁰⁷ University of Chinese Academy of Sciences, No.19(A) Yuquan Road, Shijingshan District, Beijing 100049, People's Republic of China
- ¹⁰⁸ São Paulo State University, Grupo de Dinâmica Orbital e Planetologia, CEP 12516-410, Guaratinguetá, SP, Brazil
- ¹⁰⁹ Niels Bohr Institute, University of Copenhagen, Juliane Maries Vej 30, 2100 Copenhagen Ø, Denmark
- ¹¹⁰ DXC Technology, Retortvej 8, 2500 Valby, Denmark
- ¹¹¹ Las Cumbres Observatory, 6740 Cortona Drive Suite 102, Goleta, CA 93117, USA
- ¹¹² CIGUS CITIC, Department of Nautical Sciences and Marine Engineering, University of A Coruña, Paseo de Ronda 51, 15071, A Coruña, Spain
- ¹¹³ Astrophysics Research Institute, Liverpool John Moores University, 146 Brownlow Hill, Liverpool L3 5RF, United Kingdom
- ¹¹⁴ IRAP, Université de Toulouse, CNRS, UPS, CNES, 9 Av. colonel Roche, BP 44346, 31028 Toulouse Cedex 4, France
- ¹¹⁵ MTA CSFK Lendület Near-Field Cosmology Research Group, Konkoly Observatory, MTA Research Centre for Astronomy and Earth Sciences, Konkoly Thege Miklós út 15-17, 1121 Budapest, Hungary
- ¹¹⁶ Pervasive Technologies s.l., c. Saragossa 118, 08006 Barcelona, Spain
- ¹¹⁷ School of Physics and Astronomy, University of Leicester, University Road, Leicester LE1 7RH, United Kingdom
- ¹¹⁸ Villanova University, Department of Astrophysics and Planetary Science, 800 E Lancaster Avenue, Villanova PA 19085, USA
- ¹¹⁹ Departamento de Física de la Tierra y Astrofísica, Universidad Complutense de Madrid, 28040 Madrid, Spain
- ¹²⁰ INAF - Osservatorio Astronomico di Brera, via E. Bianchi, 46, 23807 Merate (LC), Italy
- ¹²¹ National Astronomical Observatory of Japan, 2-21-1 Osawa, Mitaka, Tokyo 181-8588, Japan
- ¹²² Department of Particle Physics and Astrophysics, Weizmann Institute of Science, Rehovot 7610001, Israel
- ¹²³ Centre de Données Astronomiques de Strasbourg, Strasbourg, France
- ¹²⁴ University of Exeter, School of Physics and Astronomy, Stocker Road, Exeter, EX2 7SJ, United Kingdom
- ¹²⁵ Departamento de Astrofísica, Centro de Astrobiología (CSIC-INTA), ESA-ESAC. Camino Bajo del Castillo s/n. 28692 Villanueva de la Cañada, Madrid, Spain
- ¹²⁶ naXys, Department of Mathematics, University of Namur, Rue de Bruxelles 61, 5000 Namur, Belgium
- ¹²⁷ INAF. Osservatorio Astronomico di Trieste, via G.B. Tiepolo 11, 34131, Trieste, Italy
- ¹²⁸ Harvard-Smithsonian Center for Astrophysics, 60 Garden St., MS 15, Cambridge, MA 02138, USA
- ¹²⁹ H H Wills Physics Laboratory, University of Bristol, Tyndall Avenue, Bristol BS8 1TL, United Kingdom
- ¹³⁰ Escuela de Arquitectura y Politécnica - Universidad Europea de Valencia, Spain
- ¹³¹ Escuela Superior de Ingeniería y Tecnología - Universidad Internacional de la Rioja, Spain

- ¹³² Department of Physics and Astronomy G. Galilei, University of Padova, Vicolo dell'Osservatorio 3, 35122, Padova, Italy
- ¹³³ Applied Physics Department, Universidade de Vigo, 36310 Vigo, Spain
- ¹³⁴ Instituto de Física e Ciencias Aeroespaciais (IFCAE), Universidade de Vigo, Á Campus de As Lagoas, 32004 Ourense, Spain
- ¹³⁵ Purple Mountain Observatory, Chinese Academy of Sciences, Nanjing 210023, China
- ¹³⁶ Sorbonne Université, CNRS, UMR7095, Institut d'Astrophysique de Paris, 98bis bd. Arago, 75014 Paris, France
- ¹³⁷ Faculty of Mathematics and Physics, University of Ljubljana, Jadranska ulica 19, 1000 Ljubljana, Slovenia
- ¹³⁸ Institute of Mathematics, Ecole Polytechnique Fédérale de Lausanne (EPFL), Switzerland

Appendix A: Catalogue data model

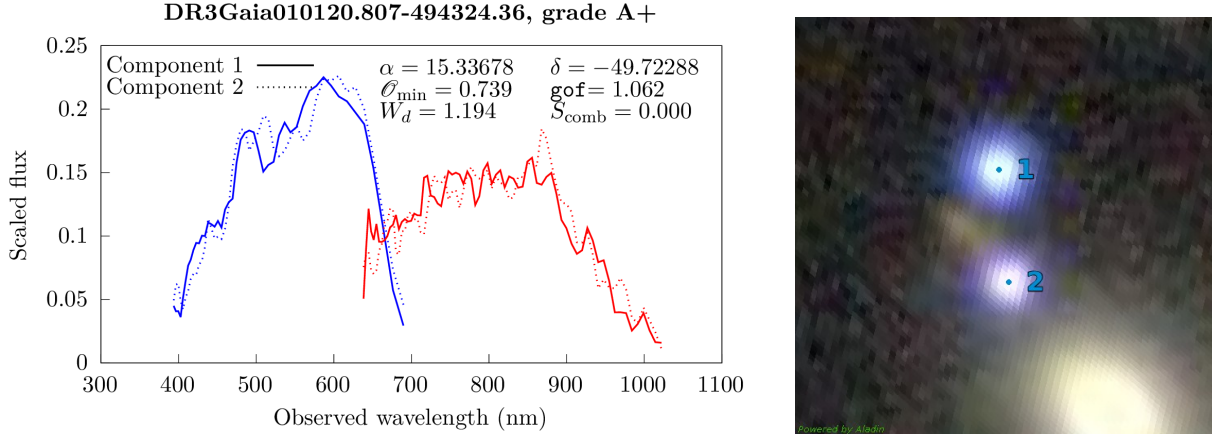
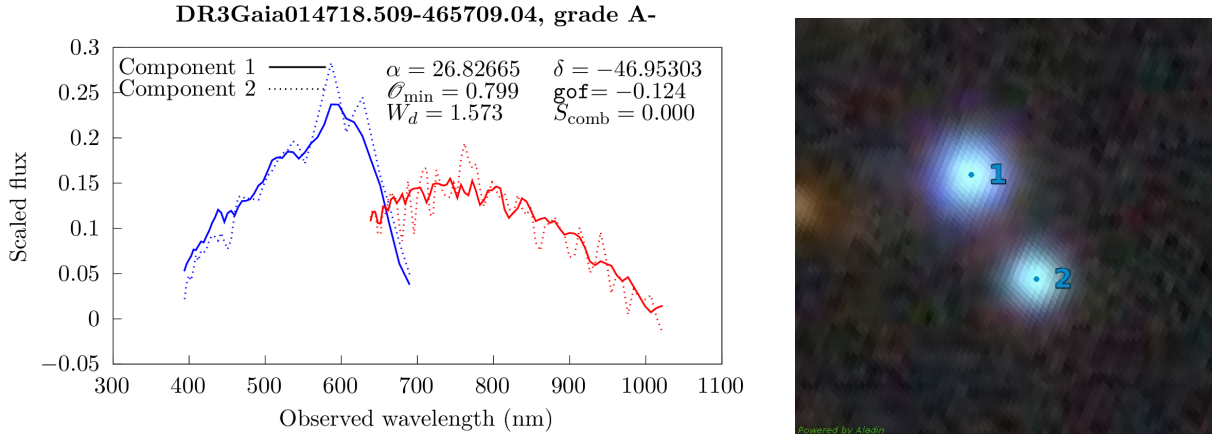
The data model of the catalogue of sources in the vicinity of quasars is described in Table [A.1](#).

Appendix B: Lens candidates

This section compares the resampled spectra of the components from some of the most promising lens candidates in Table [3](#) and displays the associated Dark Energy Survey ([Dey et al. 2019](#)) or Pan-STARRS1 ([Chambers et al. 2016](#)) images. Candidates composed of three components either have spectra for two components only (DR3Gaia021120.383+210749.64) or we decided to discard one of the spectrum for clarity purpose. The discarded spectrum is either the faintest (DR3Gaia031013.747+352414.86 and DR3Gaia210752.320-161131.67) or the most contaminated (DR3Gaia172201.867+201920.75 and DR3Gaia175323.439+144702.74). None of these discarded spectra allows to rule out the lensing hypothesis.

Table A.1. `lens_candidates` table that presents the content of the table of all sources found in the fields of the quasars analysed. For more information about the data model please refer to https://gaia.esac.esa.int/dpacsvn/DPAC/docs/ReleaseDocumentation/FPR/FPR_master.pdf

Name	Content
<code>solution_id</code>	Solution Identifier
<code>source_id</code>	Unique source identifier of the quasar analysed
<code>name</code>	Name of the multiplet corresponding to the coordinates of the quasar analysed
<code>flag</code>	Flag at the quasar level (see 3.4 for detailed description)
<code>n_components</code>	Number of components found in the field of the quasar analysed
<code>component_id</code>	Index of the component for this quasar field
<code>n_obs_component</code>	Number of valid observations used for this component
<code>component_flag</code>	flag of this component
<code>ra_component</code>	Mean right ascension of the component
<code>ra_std_component</code>	Standard deviation of the right ascension of the component
<code>dec_component</code>	Mean declination of the component
<code>dec_std_component</code>	Standard deviation of the declination of the component
<code>g_flux_component</code>	Mean <i>G</i> flux of the component
<code>g_flux_component_error</code>	Uncertainty of the mean flux value for this component
<code>g_mag_component</code>	Mean onboard <i>G</i> magnitude of the component
<code>g_mag_std_component</code>	Standard deviation of the onboard <i>G</i> magnitude of the component

**Fig. B.1.** Comparison of the resampled spectra of the DR3Gaia010120.807-494324.36 multiplet (Left) and associated Dark Energy Survey image (Right) (Dey et al. 2019). Blue dots correspond to the GravLens components. Cutout size is $15.0'' \times 15.0''$, north is up, east is left.**Fig. B.2.** Comparison of the resampled spectra of the DR3Gaia014718.509-465709.04 multiplet (Left) and associated Dark Energy Survey image (Right) (Dey et al. 2019). Blue dots correspond to the GravLens components. Cutout size is $15.0'' \times 15.0''$, north is up, east is left.

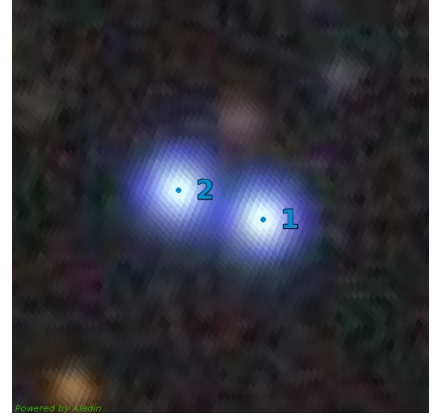
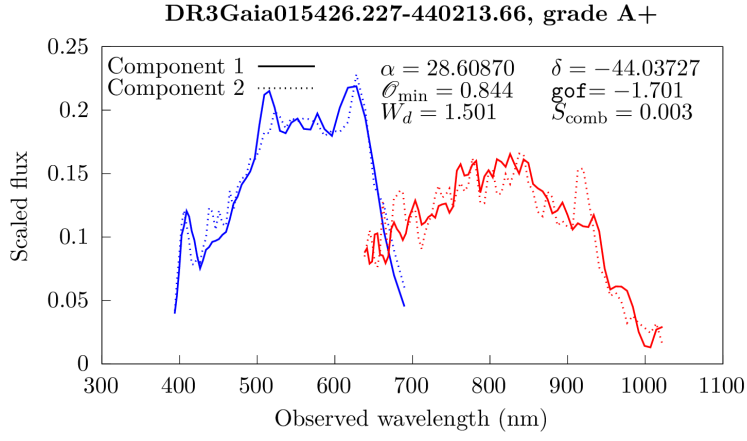


Fig. B.3. Comparison of the resampled spectra of the DR3Gaia015426.227-440213.66 multiplet (Left) and associated Dark Energy Survey image (Right) (Dey et al. 2019). Blue dots correspond to the GravLens components. Cutout size is $15.0'' \times 15.0''$, north is up, east is left.

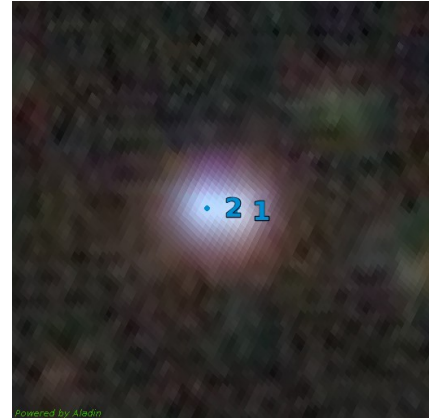
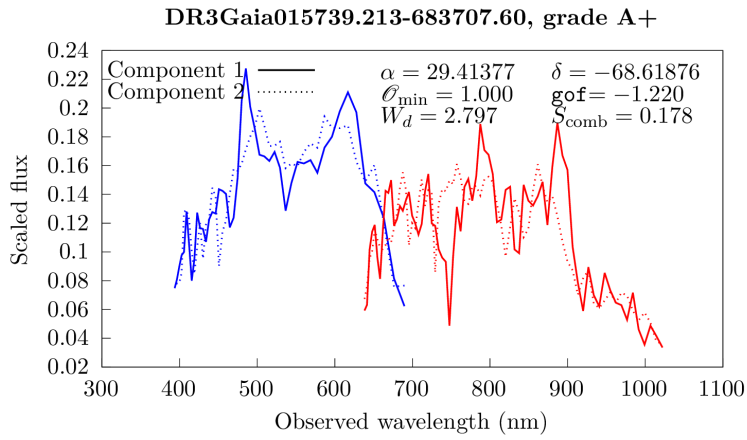


Fig. B.4. Comparison of the resampled spectra of the DR3Gaia015739.213-683707.60 multiplet (Left) and associated Dark Energy Survey image (Right) (Dey et al. 2019). Blue dots correspond to the GravLens components. Cutout size is $15.0'' \times 15.0''$, north is up, east is left.

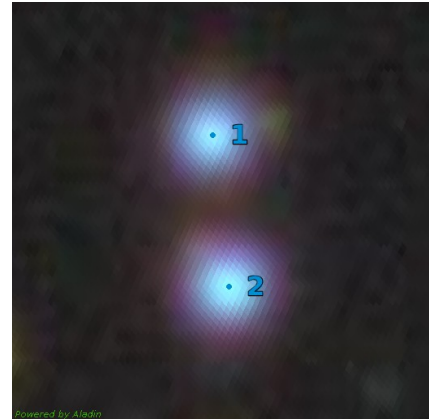
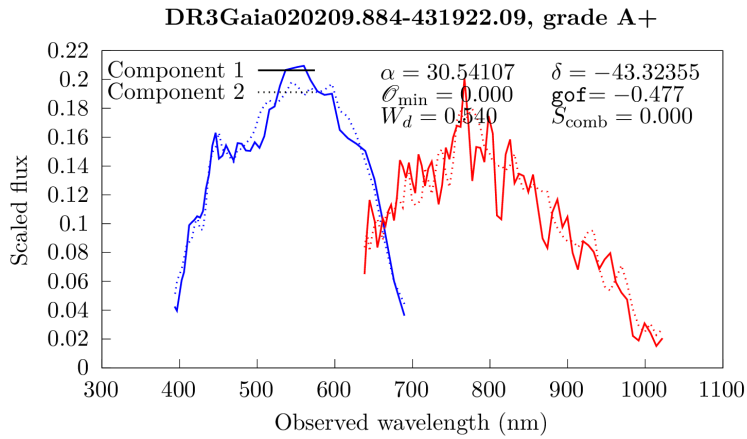


Fig. B.5. Comparison of the resampled spectra of the DR3Gaia020209.884-431922.09 multiplet (Left) and associated Dark Energy Survey image (Right) (Dey et al. 2019). Blue dots correspond to the GravLens components. Cutout size is $15.0'' \times 15.0''$, north is up, east is left.

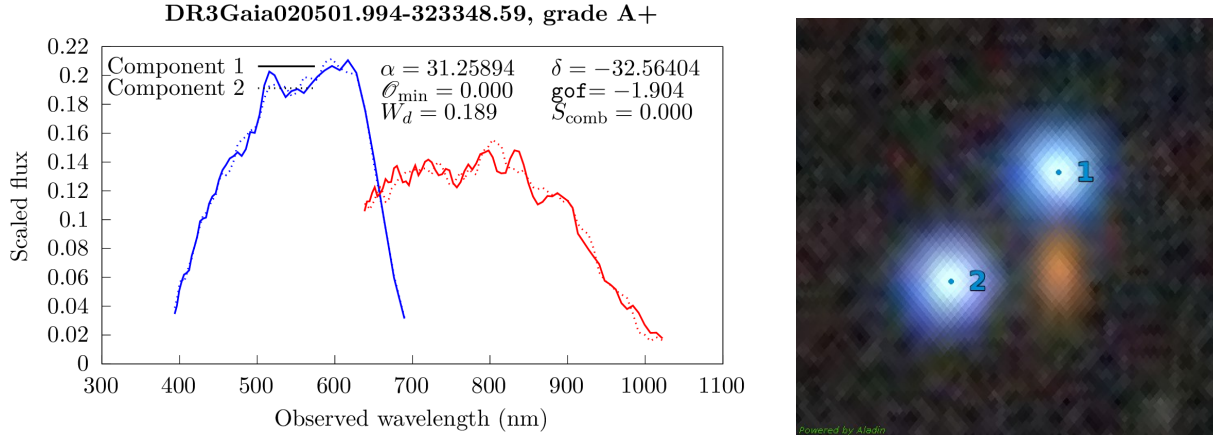


Fig. B.6. Comparison of the resampled spectra of the DR3Gaia020501.994-323348.59 multiplet (Left) and associated Dark Energy Survey image (Right) (Dey et al. 2019). Blue dots correspond to the GravLens components. Cutout size is $15.0'' \times 15.0''$, north is up, east is left.

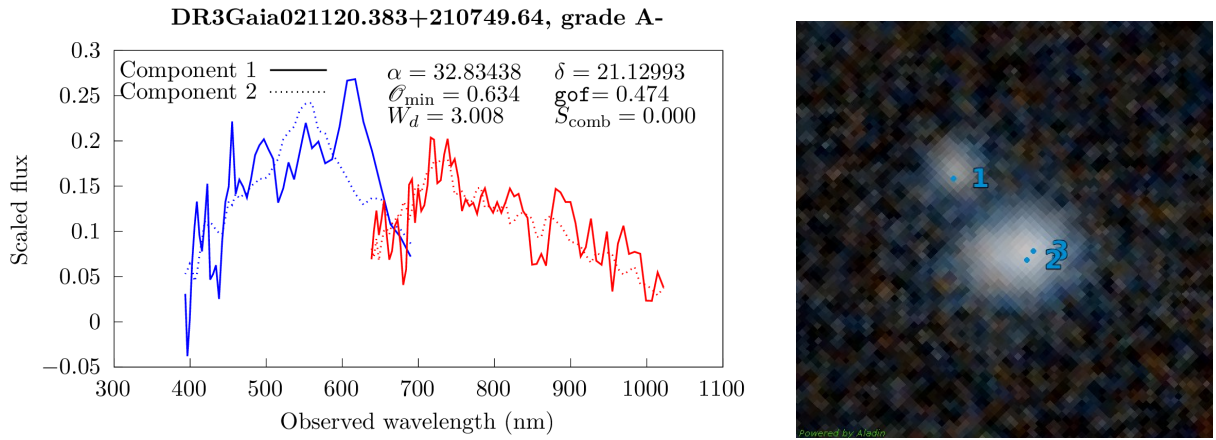


Fig. B.7. Comparison of the resampled spectra of the DR3Gaia021120.383+210749.64 multiplet (Left) and associated Pan-STARRS1 image (Right) (Chambers et al. 2016). Blue dots correspond to the GravLens components. Cutout size is $15.0'' \times 15.0''$, north is up, east is left.

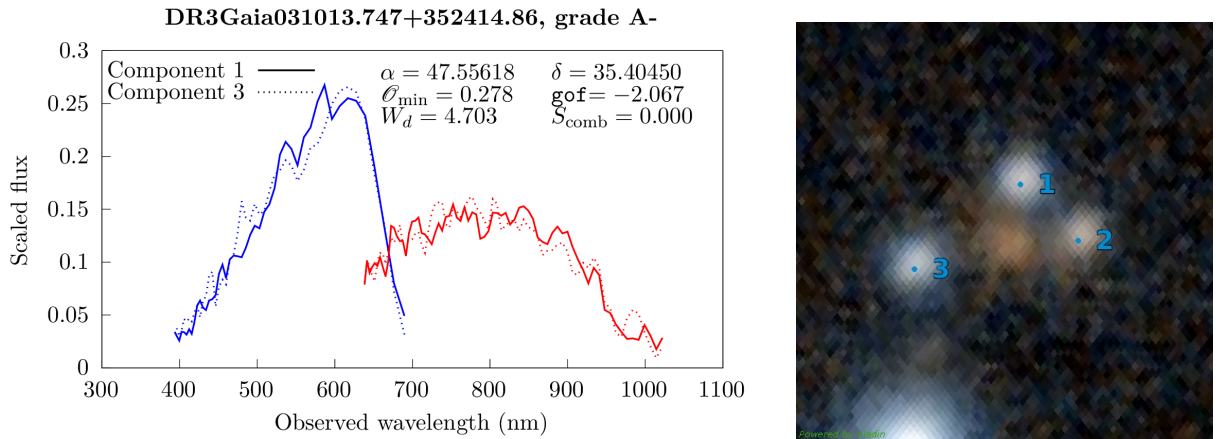


Fig. B.8. Comparison of the resampled spectra of the DR3Gaia031013.747+352414.86 multiplet (Left) and associated Pan-STARRS1 image (Right) (Chambers et al. 2016). Blue dots correspond to the GravLens components. Cutout size is $15.0'' \times 15.0''$, north is up, east is left.

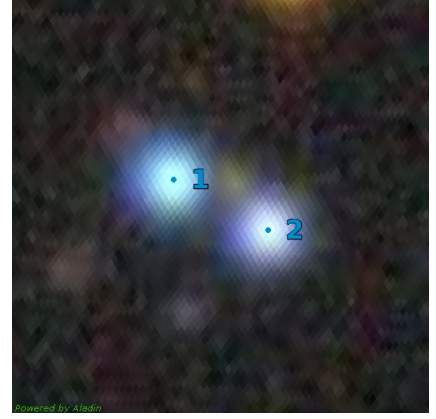
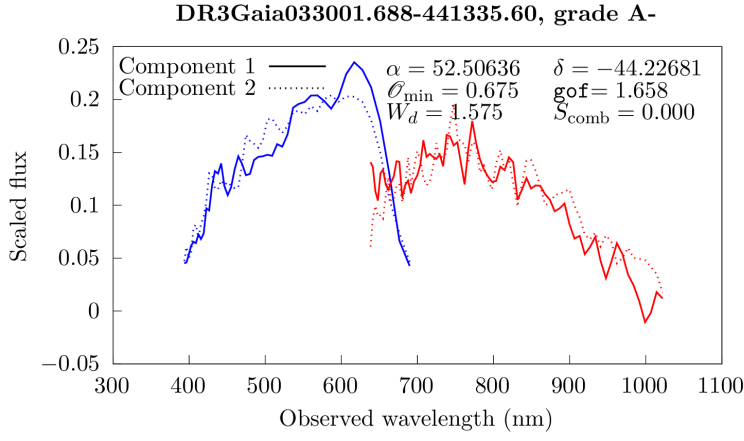


Fig. B.9. Comparison of the resampled spectra of the DR3Gaia033001.688-441335.60 multiplet (Left) and associated Dark Energy Survey image (Right) (Dey et al. 2019). Blue dots correspond to the GravLens components. Cutout size is $15.0'' \times 15.0''$, north is up, east is left.

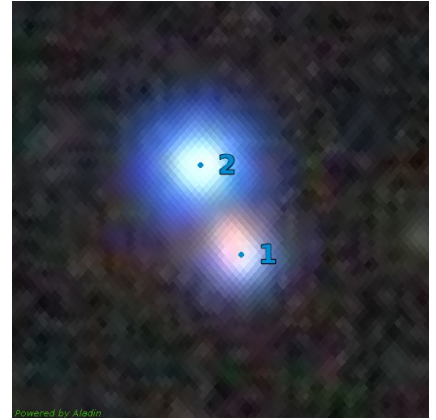
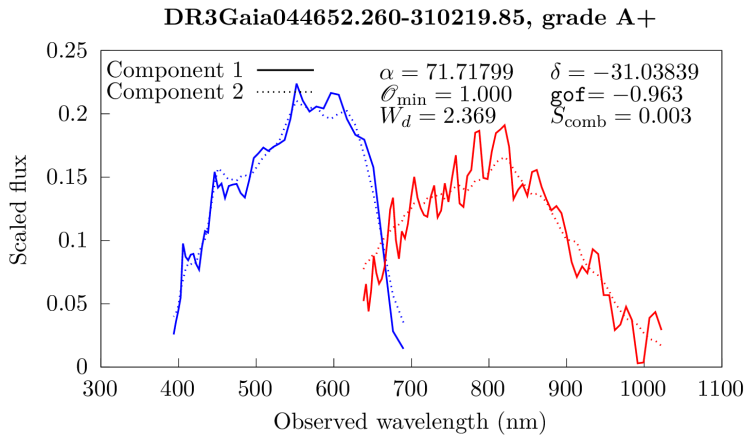


Fig. B.10. Comparison of the resampled spectra of the DR3Gaia044652.260-310219.85 multiplet (Left) and associated Dark Energy Survey image (Right) (Dey et al. 2019). Blue dots correspond to the GravLens components. Cutout size is $15.0'' \times 15.0''$, north is up, east is left.

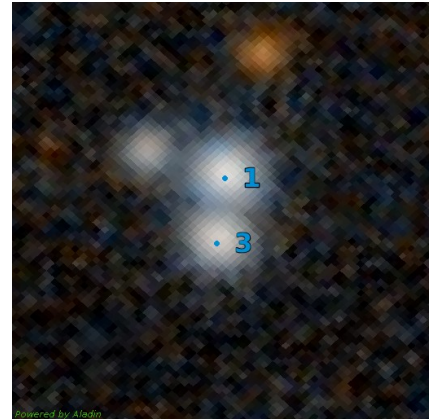
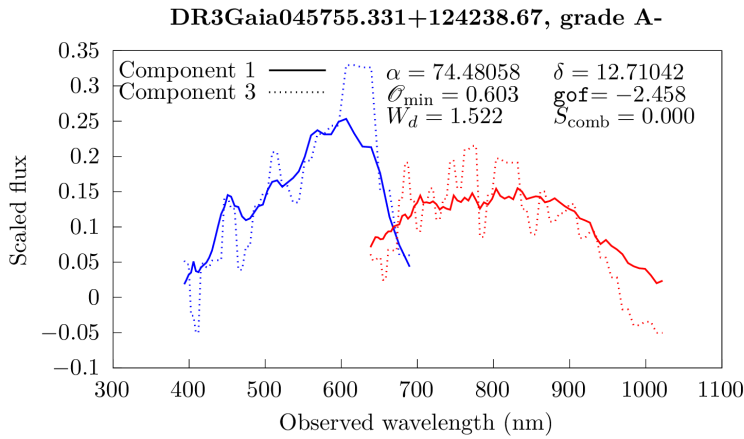


Fig. B.11. Comparison of the resampled spectra of the DR3Gaia045755.331+124238.67 multiplet (Left) and associated Pan-STARRS1 image (Right) (Chambers et al. 2016). Blue dots correspond to the GravLens components. Cutout size is $15.0'' \times 15.0''$, north is up, east is left.

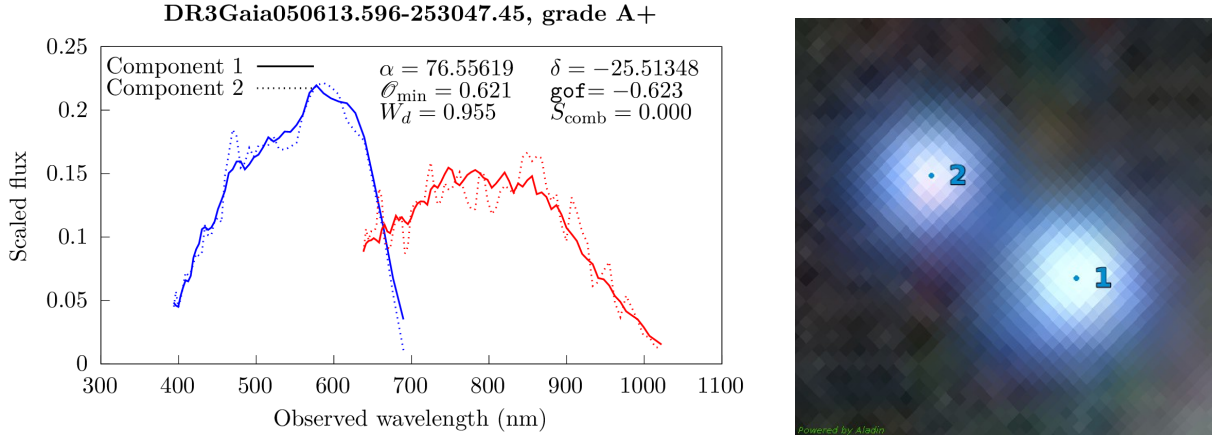


Fig. B.12. Comparison of the resampled spectra of the DR3Gaia050613.596-253047.45 multiplet (Left) and associated Dark Energy Survey image (Right) (Dey et al. 2019). Blue dots correspond to the GravLens components. Cutout size is $15.0'' \times 15.0''$, north is up, east is left.

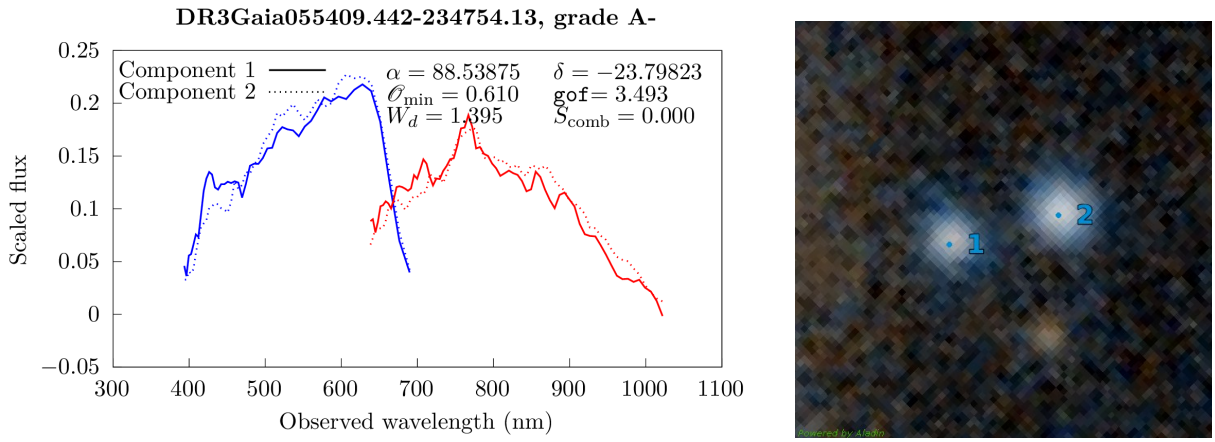


Fig. B.13. Comparison of the resampled spectra of the DR3Gaia055409.442-234754.13 multiplet (Left) and associated Pan-STARRS1 image (Right) (Chambers et al. 2016). Blue dots correspond to the GravLens components. Cutout size is $15.0'' \times 15.0''$, north is up, east is left.

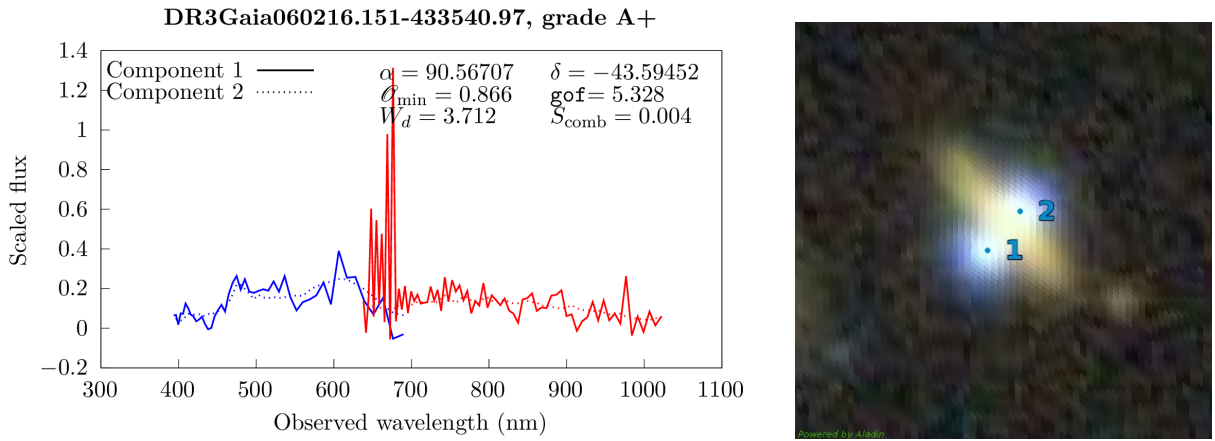


Fig. B.14. Comparison of the resampled spectra of the DR3Gaia060216.151-433540.97 multiplet (Left) and associated Dark Energy Survey image (Right) (Dey et al. 2019). Blue dots correspond to the GravLens components. Cutout size is $15.0'' \times 15.0''$, north is up, east is left.

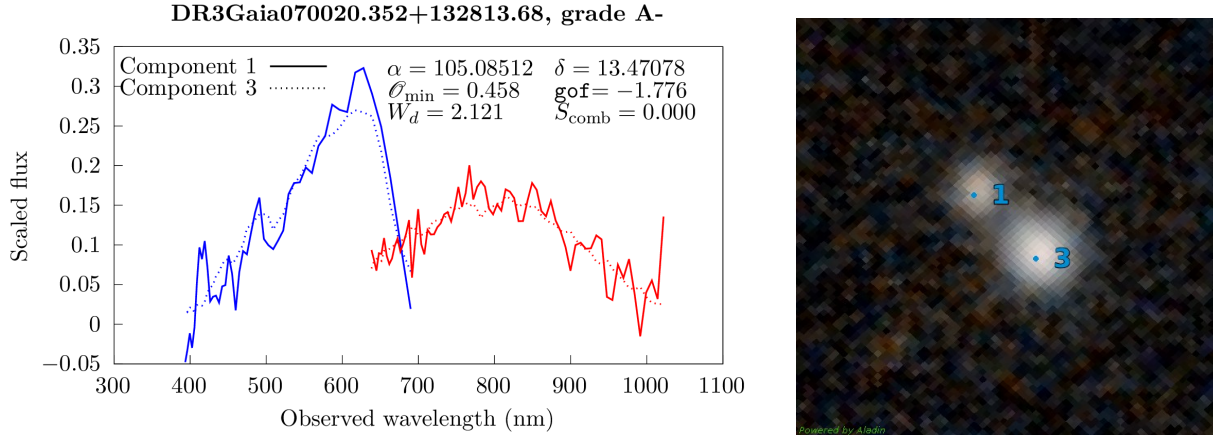


Fig. B.15. Comparison of the resampled spectra of the DR3Gaia070020.352+132813.68 multiplet (Left) and associated Pan-STARRS1 image (Right) (Chambers et al. 2016). Blue dots correspond to the GravLens components. Cutout size is $15.0'' \times 15.0''$, north is up, east is left.

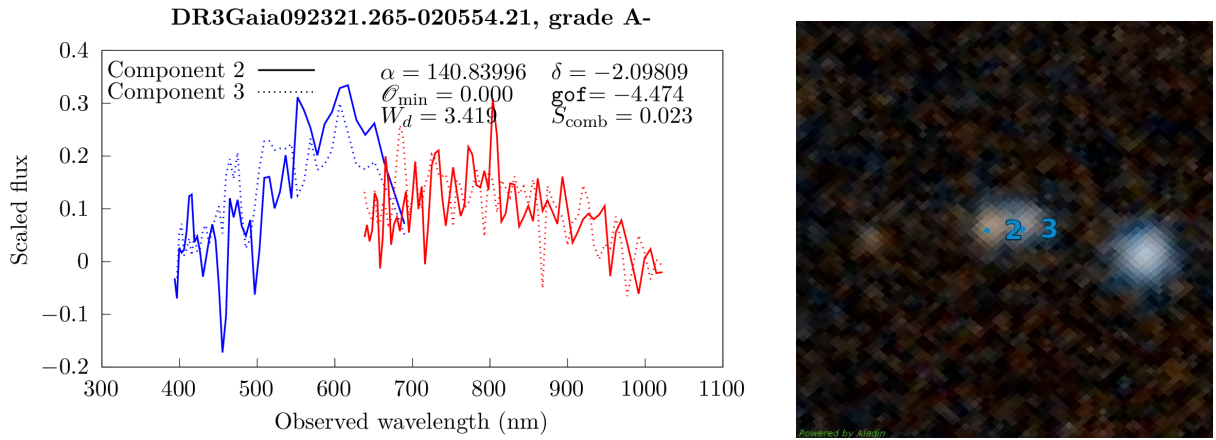


Fig. B.16. Comparison of the resampled spectra of the DR3Gaia092321.265-020554.21 multiplet (Left) and associated Pan-STARRS1 image (Right) (Chambers et al. 2016). Blue dots correspond to the GravLens components. Cutout size is $15.0'' \times 15.0''$, north is up, east is left.

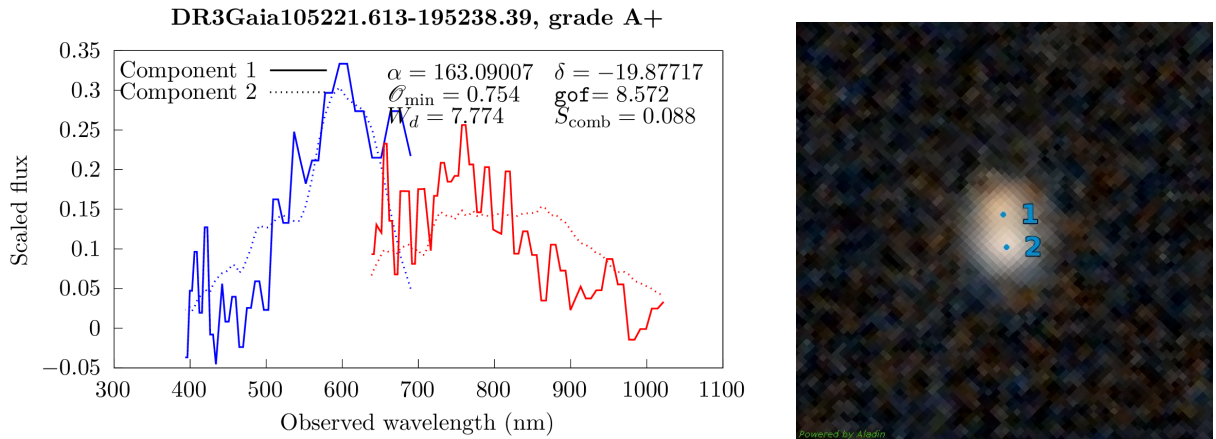


Fig. B.17. Comparison of the resampled spectra of the DR3Gaia105221.613-195238.39 multiplet (Left) and associated Pan-STARRS1 image (Right) (Chambers et al. 2016). Blue dots correspond to the GravLens components. Cutout size is $15.0'' \times 15.0''$, north is up, east is left.

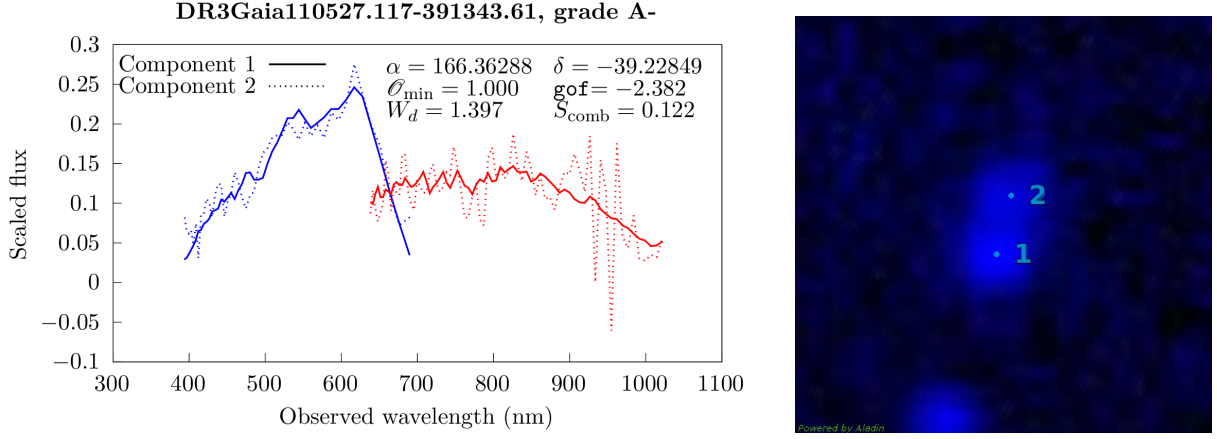


Fig. B.18. Comparison of the resampled spectra of the DR3Gaia110527.117-391343.61 multiplet (Left) and associated Dark Energy Survey image (Right) (Dey et al. 2019). Blue dots correspond to the GravLens components. Cutout size is $15.0'' \times 15.0''$, north is up, east is left.

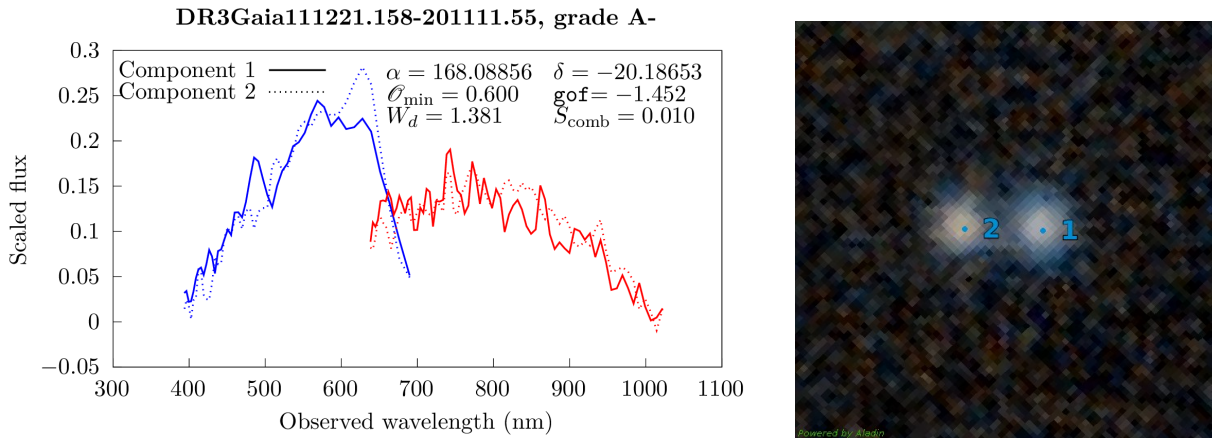


Fig. B.19. Comparison of the resampled spectra of the DR3Gaia11221.158-201111.55 multiplet (Left) and associated Pan-STARRS1 image (Right) (Chambers et al. 2016). Blue dots correspond to the GravLens components. Cutout size is $15.0'' \times 15.0''$, north is up, east is left.

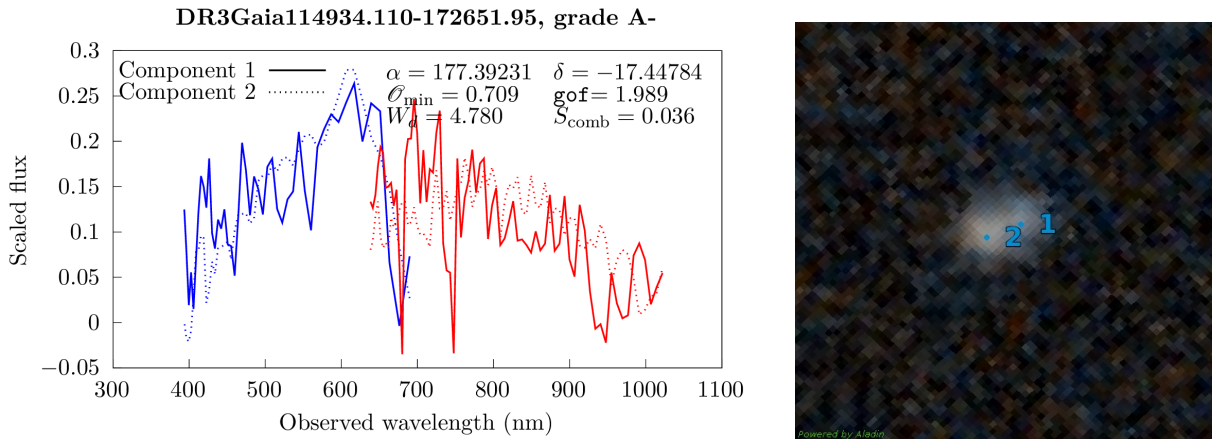


Fig. B.20. Comparison of the resampled spectra of the DR3Gaia114934.110-172651.95 multiplet (Left) and associated Pan-STARRS1 image (Right) (Chambers et al. 2016). Blue dots correspond to the GravLens components. Cutout size is $15.0'' \times 15.0''$, north is up, east is left.

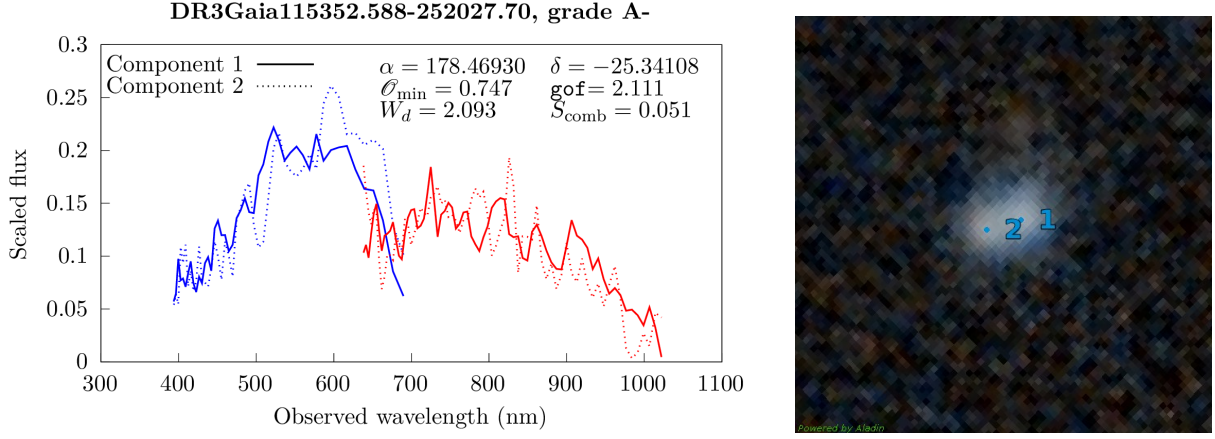


Fig. B.21. Comparison of the resampled spectra of the DR3Gaia115352.588-252027.70 multiplet (Left) and associated Pan-STARRS1 image (Right) (Chambers et al. 2016). Blue dots correspond to the GravLens components. Cutout size is $15.0'' \times 15.0''$, north is up, east is left.

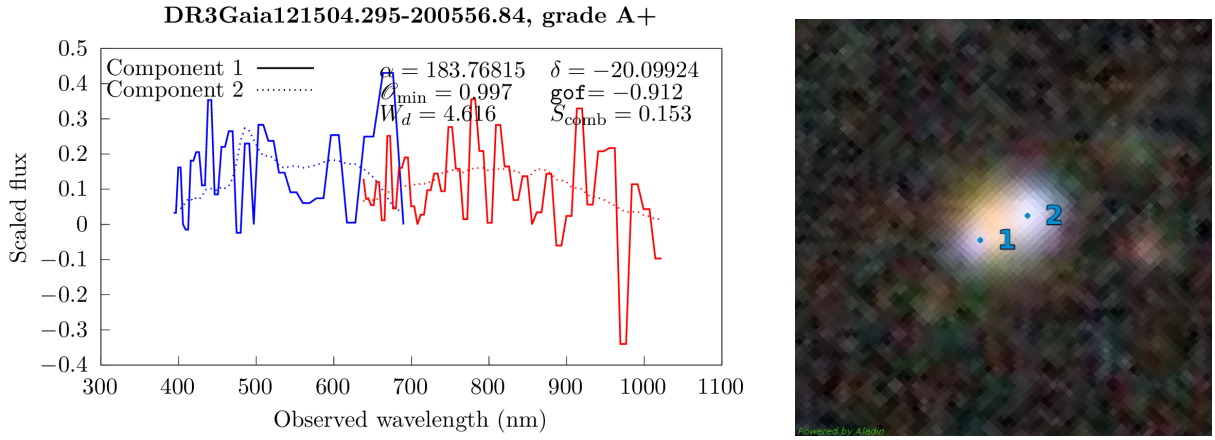


Fig. B.22. Comparison of the resampled spectra of the DR3Gaia121504.295-200556.84 multiplet (Left) and associated Dark Energy Survey image (Right) (Dey et al. 2019). Blue dots correspond to the GravLens components. Cutout size is $15.0'' \times 15.0''$, north is up, east is left.

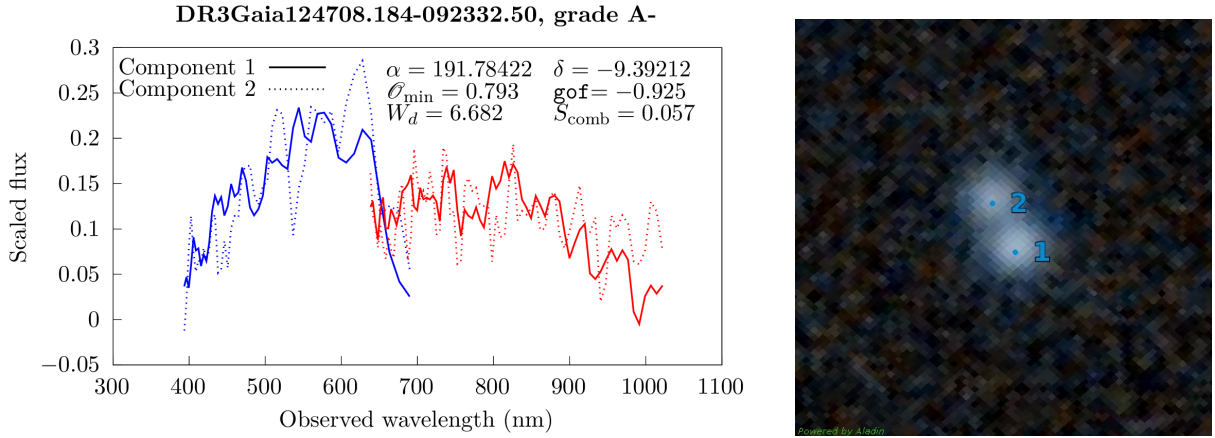


Fig. B.23. Comparison of the resampled spectra of the DR3Gaia124708.184-092332.50 multiplet (Left) and associated Pan-STARRS1 image (Right) (Chambers et al. 2016). Blue dots correspond to the GravLens components. Cutout size is $15.0'' \times 15.0''$, north is up, east is left.

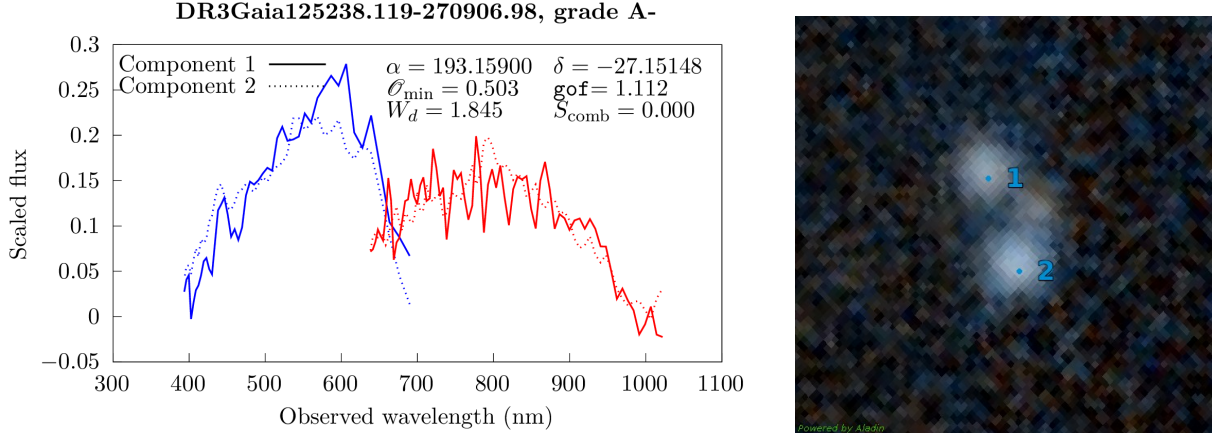


Fig. B.24. Comparison of the resampled spectra of the DR3Gaia125238.119-270906.98 multiplet (Left) and associated Pan-STARRS1 image (Right) (Chambers et al. 2016). Blue dots correspond to the GravLens components. Cutout size is $15.0'' \times 15.0''$, north is up, east is left.

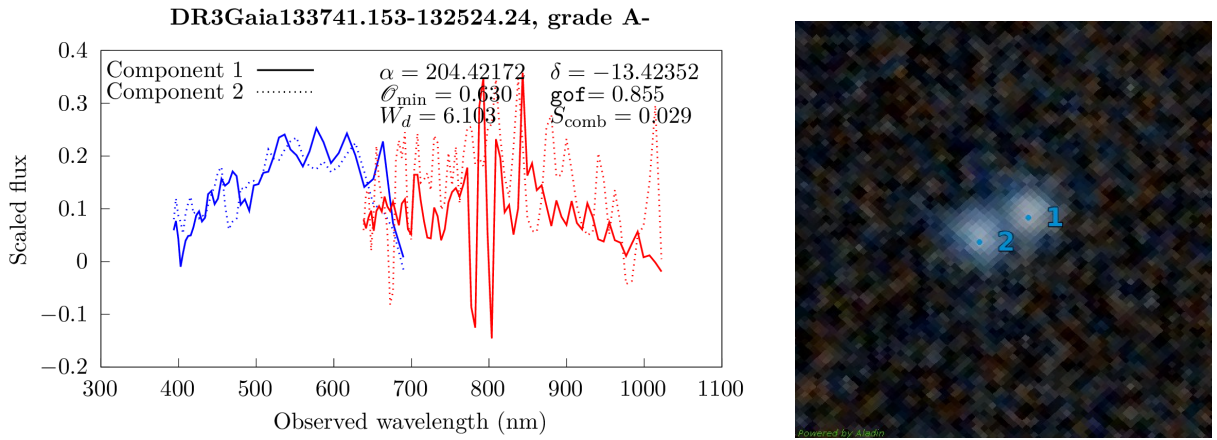


Fig. B.25. Comparison of the resampled spectra of the DR3Gaia133741.153-132524.24 multiplet (Left) and associated Pan-STARRS1 image (Right) (Chambers et al. 2016). Blue dots correspond to the GravLens components. Cutout size is $15.0'' \times 15.0''$, north is up, east is left.

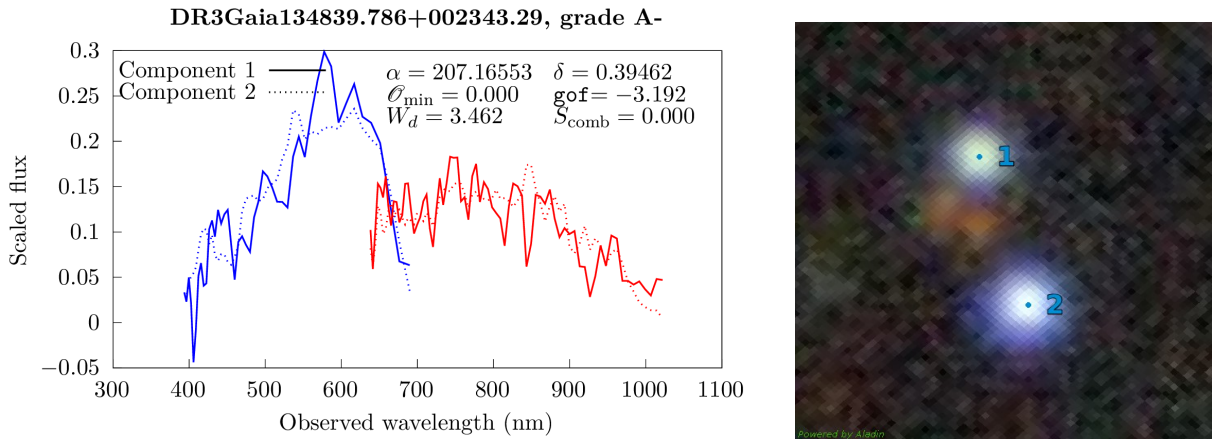


Fig. B.26. Comparison of the resampled spectra of the DR3Gaia134839.786+002343.29 multiplet (Left) and associated Dark Energy Survey image (Right) (Dey et al. 2019). Blue dots correspond to the GravLens components. Cutout size is $15.0'' \times 15.0''$, north is up, east is left.

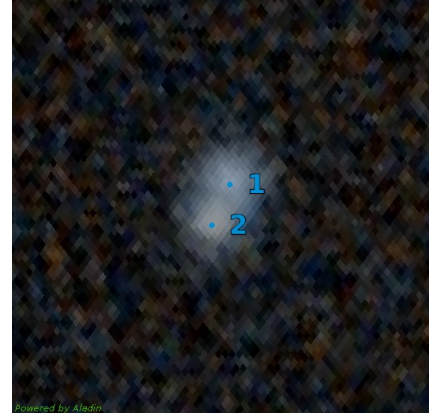
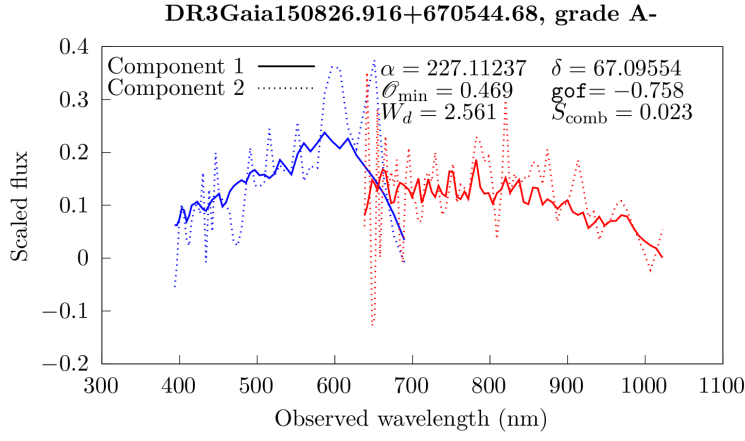


Fig. B.27. Comparison of the resampled spectra of the DR3Gaia150826.916+670544.68 multiplet (Left) and associated Pan-STARRS1 image (Right) (Chambers et al. 2016). Blue dots correspond to the GravLens components. Cutout size is $15.0'' \times 15.0''$, north is up, east is left.

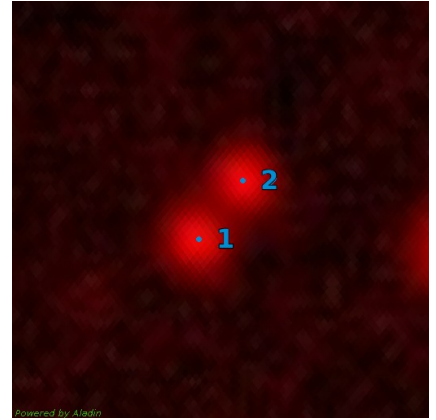
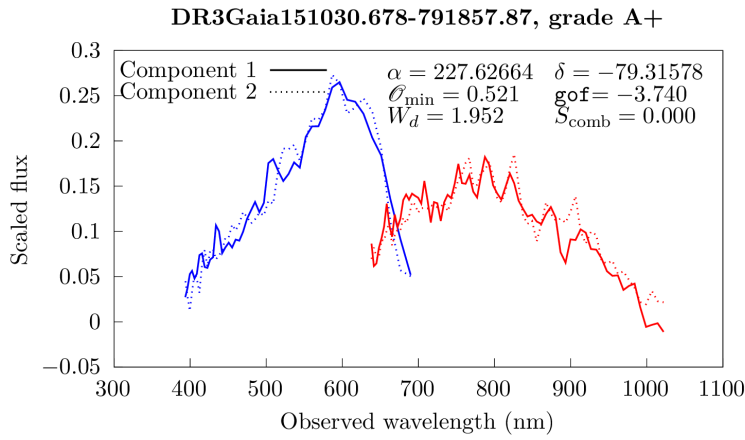


Fig. B.28. Comparison of the resampled spectra of the DR3Gaia151030.678-791857.87 multiplet (Left) and associated Dark Energy Survey image (Right) (Dey et al. 2019). Blue dots correspond to the GravLens components. Cutout size is $15.0'' \times 15.0''$, north is up, east is left.

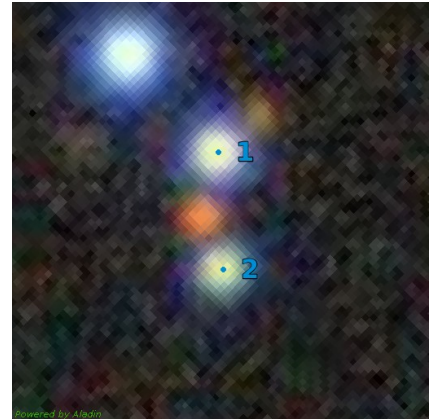
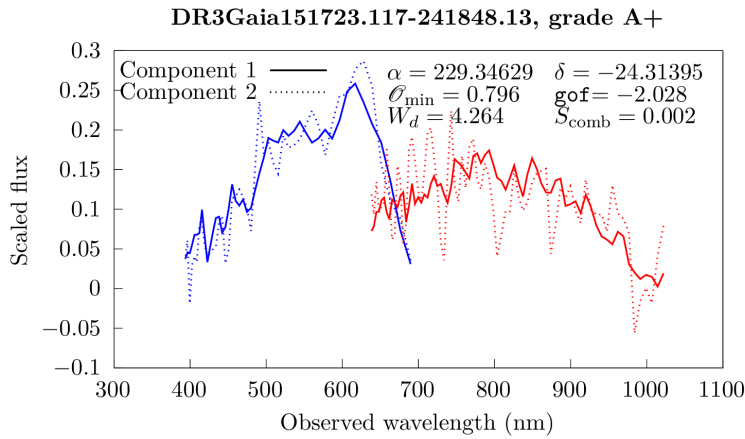


Fig. B.29. Comparison of the resampled spectra of the DR3Gaia151723.117-241848.13 multiplet (Left) and associated Dark Energy Survey image (Right) (Dey et al. 2019). Blue dots correspond to the GravLens components. Cutout size is $15.0'' \times 15.0''$, north is up, east is left.

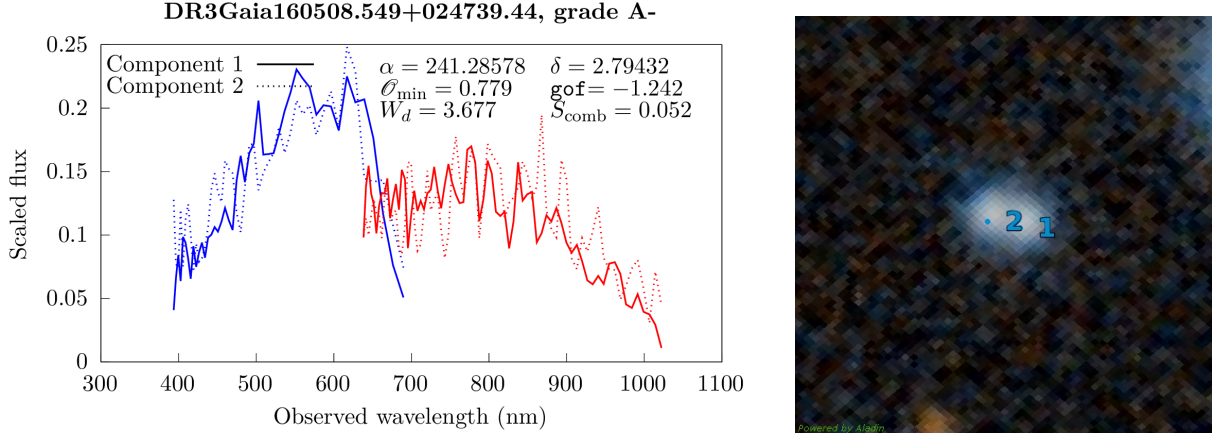


Fig. B.30. Comparison of the resampled spectra of the DR3Gaia160508.549+024739.44 multiplet (Left) and associated Pan-STARRS1 image (Right) (Chambers et al. 2016). Blue dots correspond to the GravLens components. Cutout size is $15.0'' \times 15.0''$, north is up, east is left.

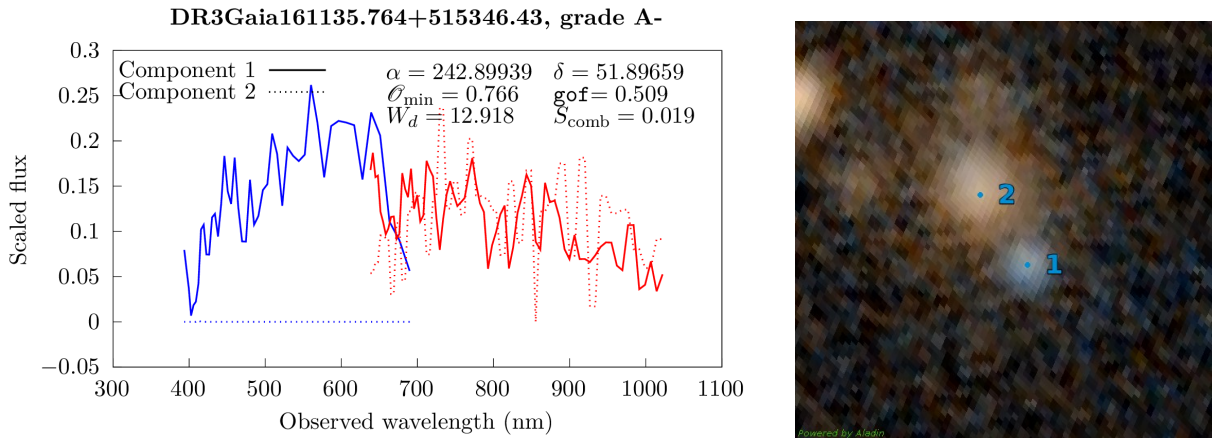


Fig. B.31. Comparison of the resampled spectra of the DR3Gaia161135.764+515346.43 multiplet (Left) and associated Pan-STARRS1 image (Right) (Chambers et al. 2016). Blue dots correspond to the GravLens components. Cutout size is $15.0'' \times 15.0''$, north is up, east is left.

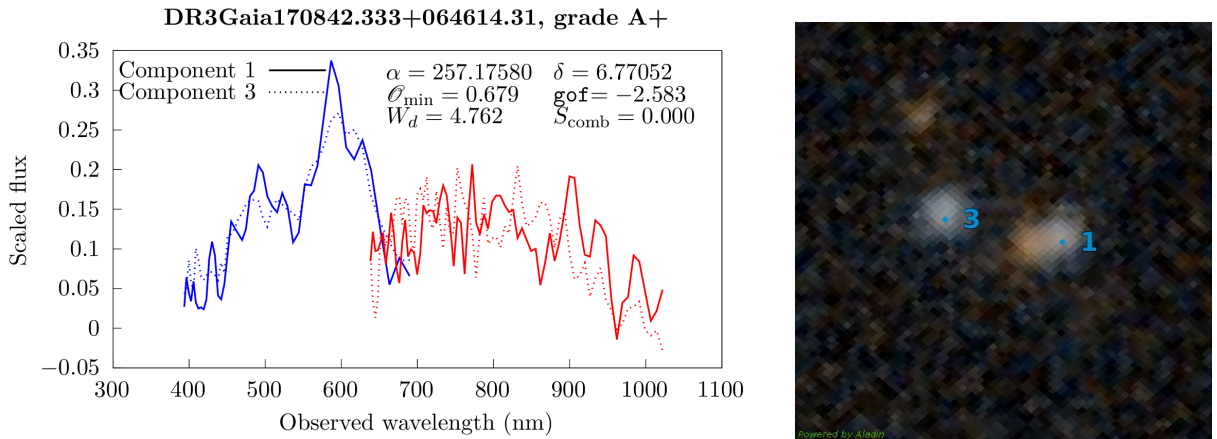


Fig. B.32. Comparison of the resampled spectra of the DR3Gaia170842.333+064614.31 multiplet (Left) and associated Pan-STARRS1 image (Right) (Chambers et al. 2016). Blue dots correspond to the GravLens components. Cutout size is $15.0'' \times 15.0''$, north is up, east is left.

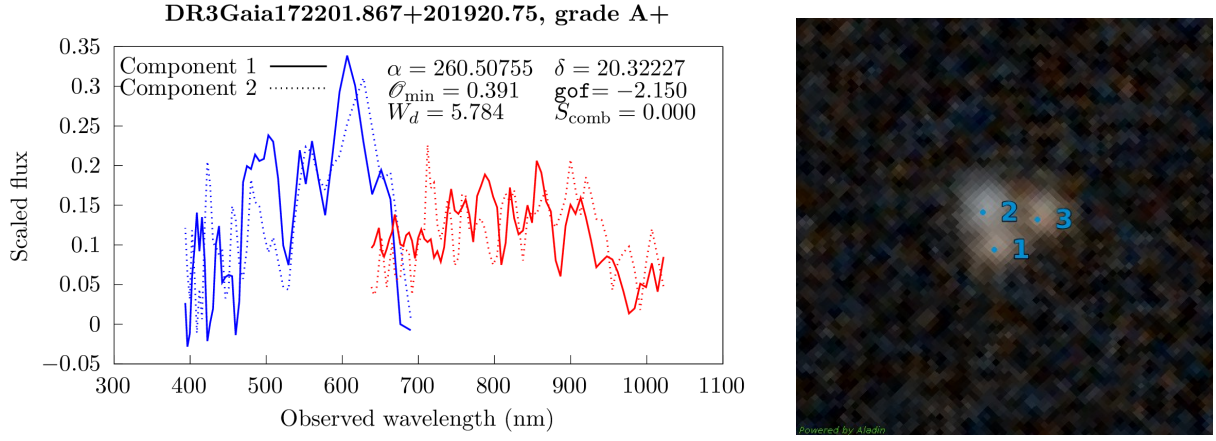


Fig. B.33. Comparison of the resampled spectra of the DR3Gaia172201.867+201920.75 multiplet (Left) and associated Pan-STARRS1 image (Right) (Chambers et al. 2016). Blue dots correspond to the GravLens components. Cutout size is $15.0'' \times 15.0''$, north is up, east is left.

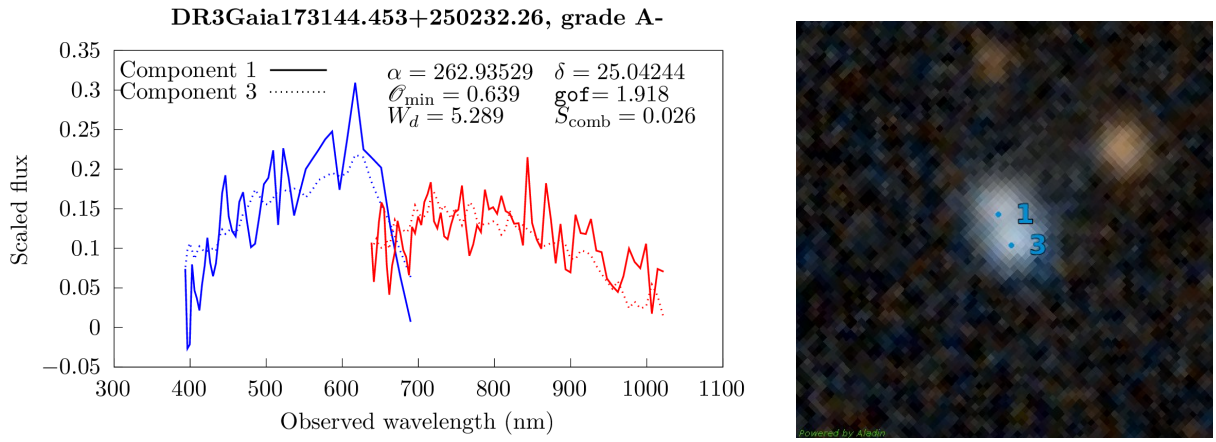


Fig. B.34. Comparison of the resampled spectra of the DR3Gaia173144.453+250232.26 multiplet (Left) and associated Pan-STARRS1 image (Right) (Chambers et al. 2016). Blue dots correspond to the GravLens components. Cutout size is $15.0'' \times 15.0''$, north is up, east is left.

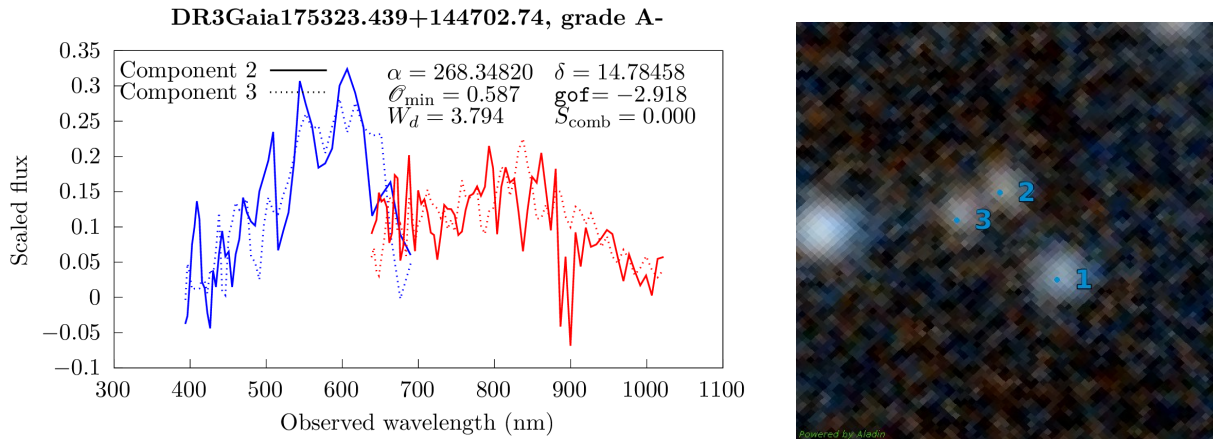


Fig. B.35. Comparison of the resampled spectra of the DR3Gaia175323.439+144702.74 multiplet (Left) and associated Pan-STARRS1 image (Right) (Chambers et al. 2016). Blue dots correspond to the GravLens components. Cutout size is $15.0'' \times 15.0''$, north is up, east is left.

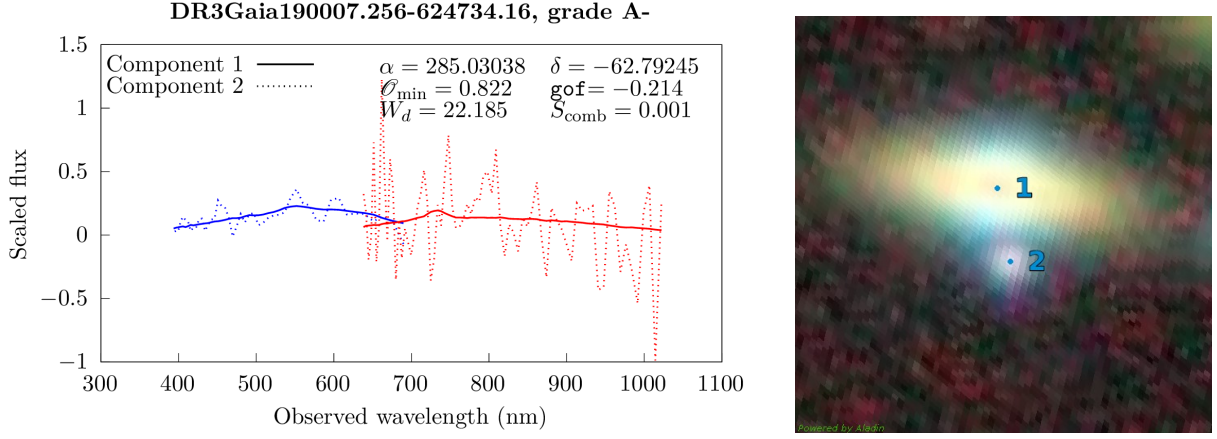


Fig. B.36. Comparison of the resampled spectra of the DR3Gaia190007.256-624734.16 multiplet (Left) and associated Dark Energy Survey image (Right) (Dey et al. 2019). Blue dots correspond to the GravLens components. Cutout size is $15.0'' \times 15.0''$, north is up, east is left. **Component 2 is presumably a contaminating source.**

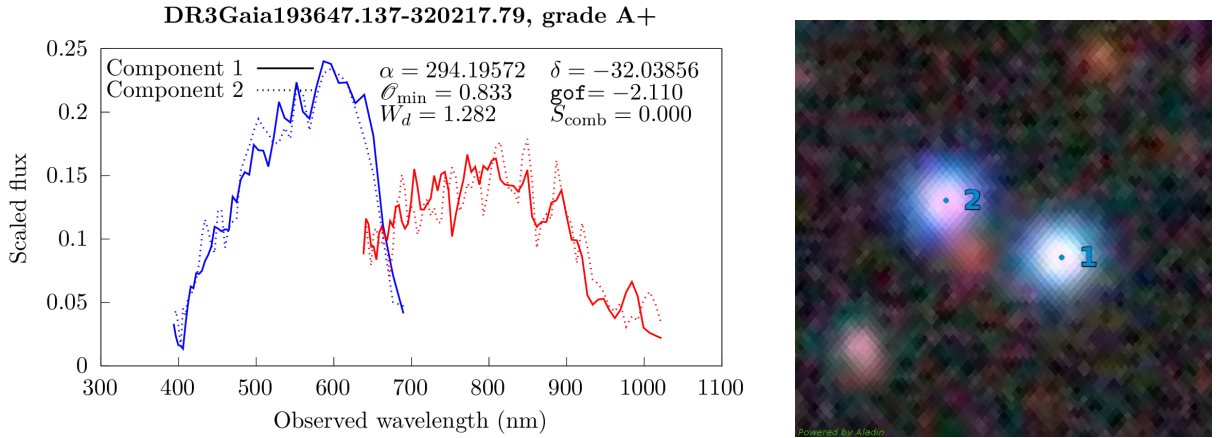


Fig. B.37. Comparison of the resampled spectra of the DR3Gaia193647.137-320217.79 multiplet (Left) and associated Dark Energy Survey image (Right) (Dey et al. 2019). Blue dots correspond to the GravLens components. Cutout size is $15.0'' \times 15.0''$, north is up, east is left.

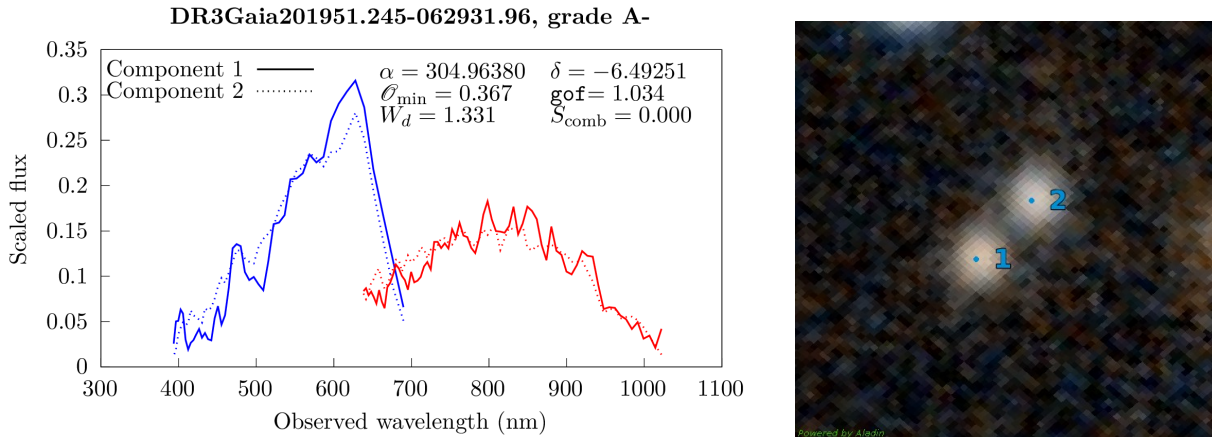


Fig. B.38. Comparison of the resampled spectra of the DR3Gaia201951.245-062931.96 multiplet (Left) and associated Pan-STARRS1 image (Right) (Chambers et al. 2016). Blue dots correspond to the GravLens components. Cutout size is $15.0'' \times 15.0''$, north is up, east is left.

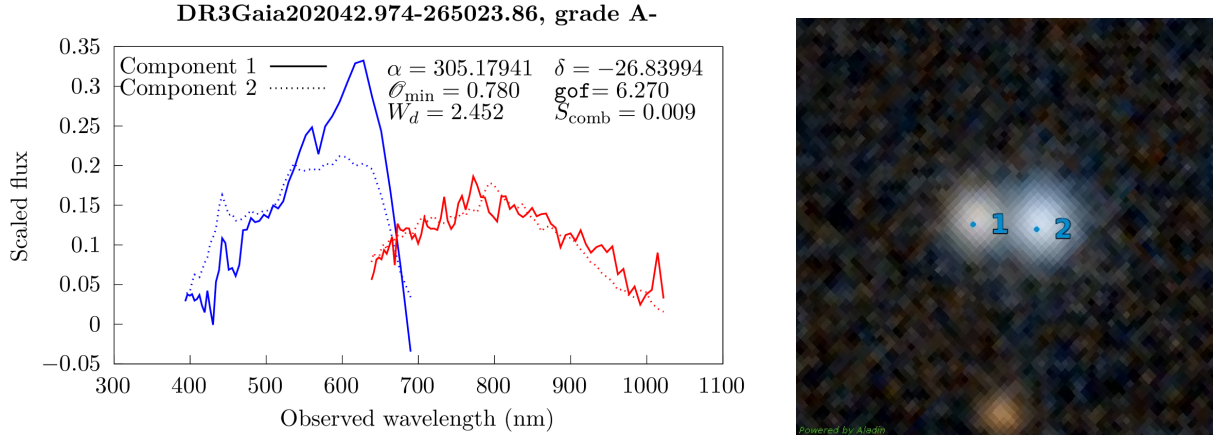


Fig. B.39. Comparison of the resampled spectra of the DR3Gaia202042.974-265023.86 multiplet (Left) and associated Pan-STARRS1 image (Right) (Chambers et al. 2016). Blue dots correspond to the GravLens components. Cutout size is $15.0'' \times 15.0''$, north is up, east is left.

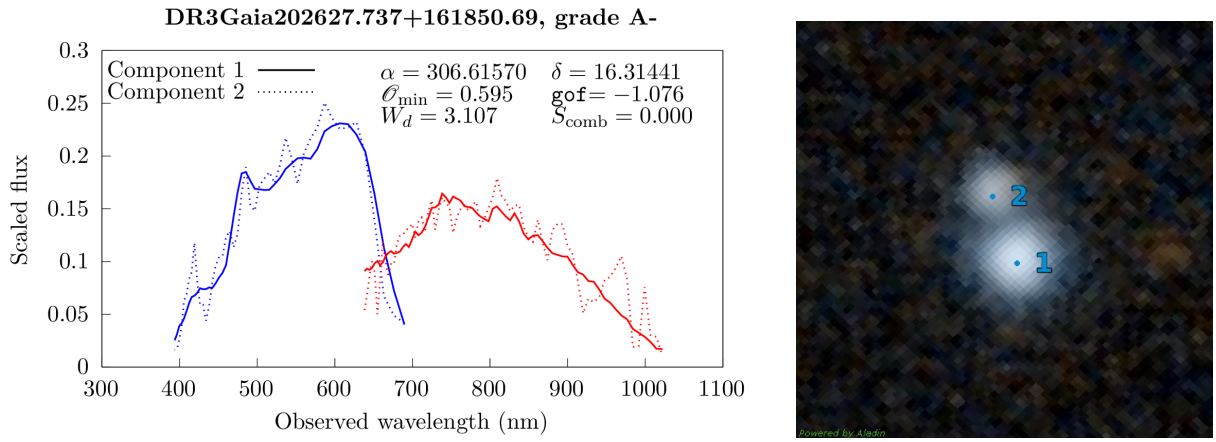


Fig. B.40. Comparison of the resampled spectra of the DR3Gaia202627.737+161850.69 multiplet (Left) and associated Pan-STARRS1 image (Right) (Chambers et al. 2016). Blue dots correspond to the GravLens components. Cutout size is $15.0'' \times 15.0''$, north is up, east is left.

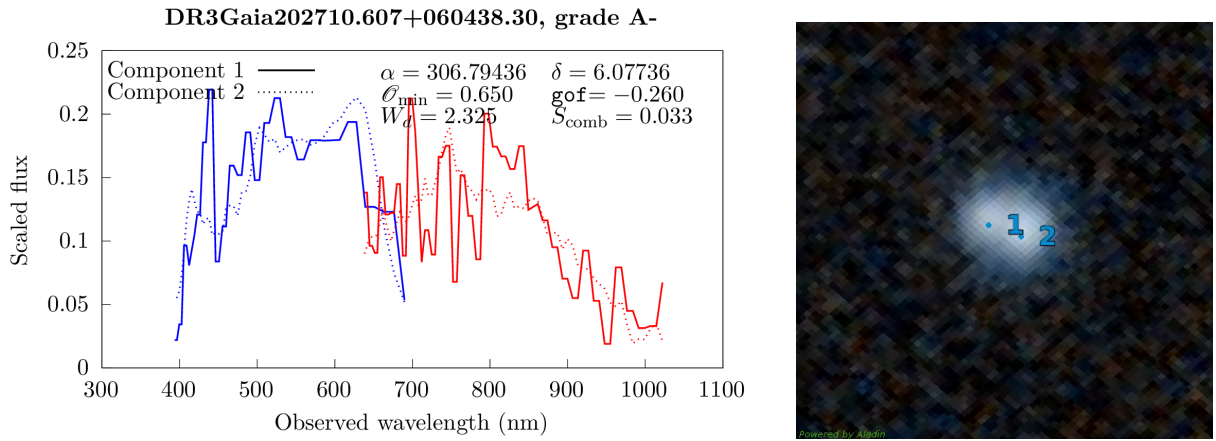


Fig. B.41. Comparison of the resampled spectra of the DR3Gaia202710.607+060438.30 multiplet (Left) and associated Pan-STARRS1 image (Right) (Chambers et al. 2016). Blue dots correspond to the GravLens components. Cutout size is $15.0'' \times 15.0''$, north is up, east is left.

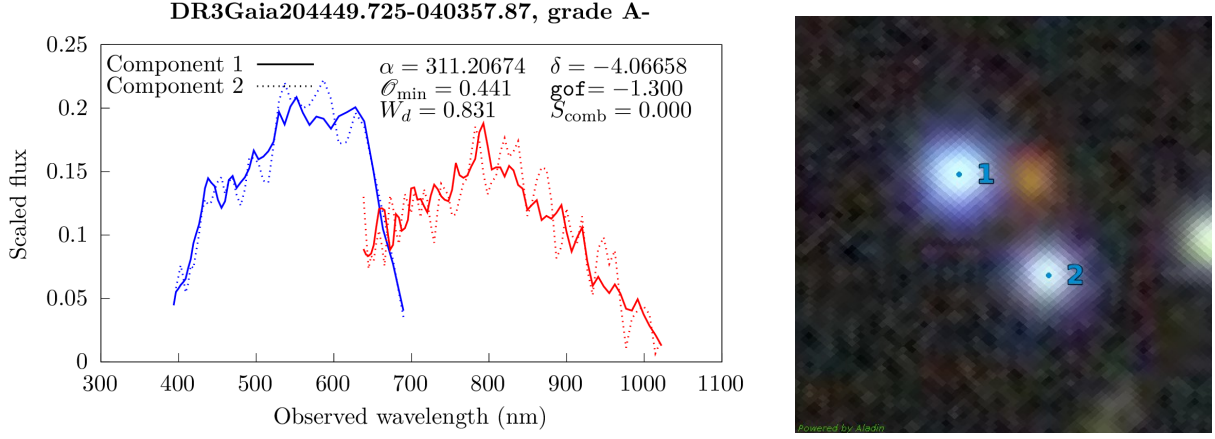


Fig. B.42. Comparison of the resampled spectra of the DR3Gaia204449.725-040357.87 multiplet (Left) and associated Dark Energy Survey image (Right) (Dey et al. 2019). Blue dots correspond to the GravLens components. Cutout size is $15.0'' \times 15.0''$, north is up, east is left.

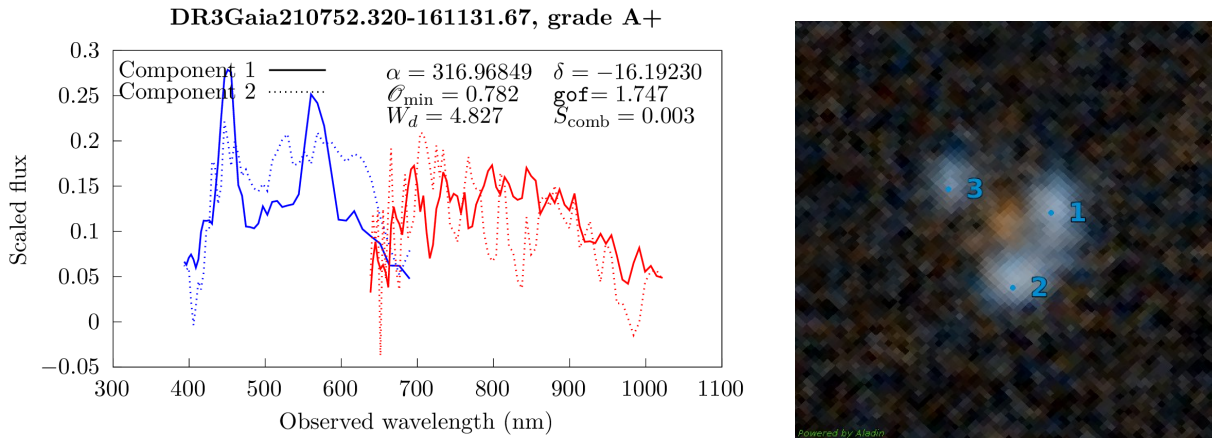


Fig. B.43. Comparison of the resampled spectra of the DR3Gaia210752.320-161131.67 multiplet (Left) and associated Pan-STARRS1 image (Right) (Chambers et al. 2016). Blue dots correspond to the GravLens components. Cutout size is $15.0'' \times 15.0''$, north is up, east is left.

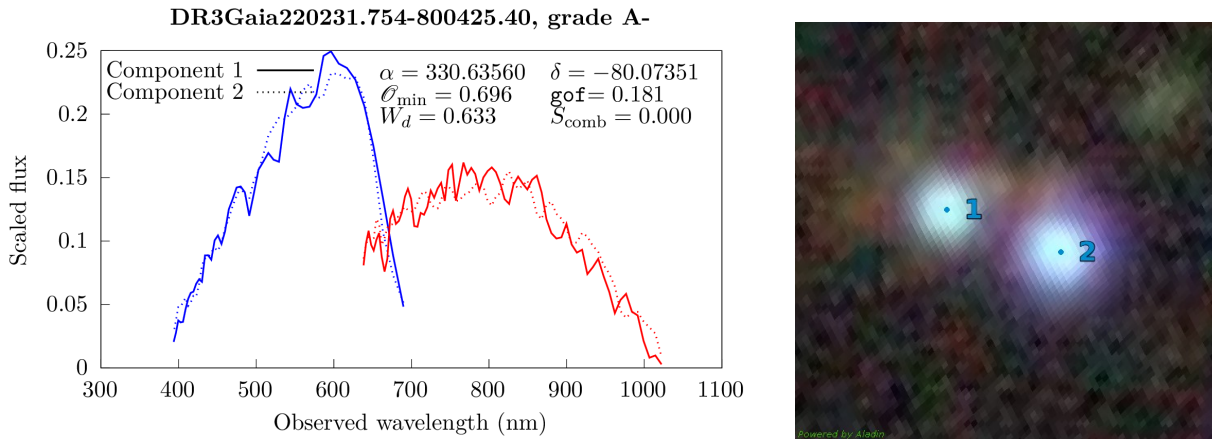


Fig. B.44. Comparison of the resampled spectra of the DR3Gaia220231.754-800425.40 multiplet (Left) and associated Dark Energy Survey image (Right) (Dey et al. 2019). Blue dots correspond to the GravLens components. Cutout size is $15.0'' \times 15.0''$, north is up, east is left.

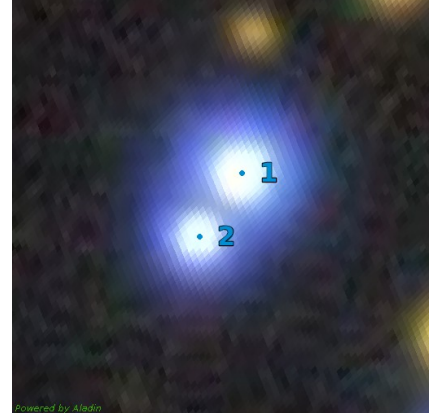
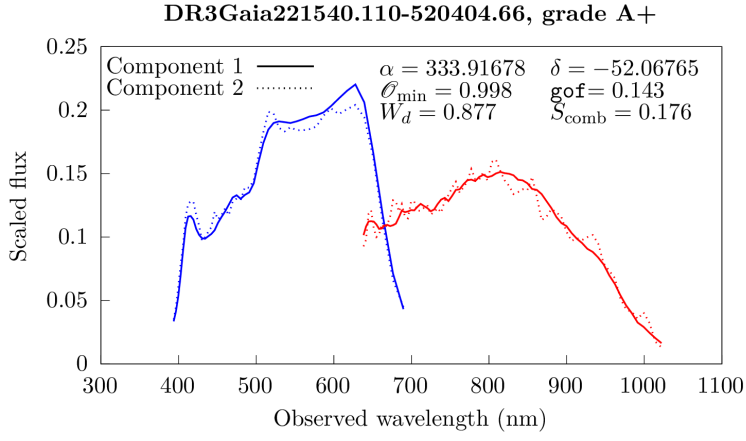


Fig. B.45. Comparison of the resampled spectra of the DR3Gaia221540.110-520404.66 multiplet (Left) and associated Dark Energy Survey image (Right) (Dey et al. 2019). Blue dots correspond to the GravLens components. Cutout size is $15.0'' \times 15.0''$, north is up, east is left.

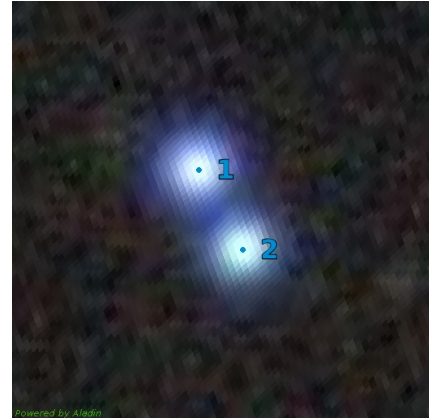
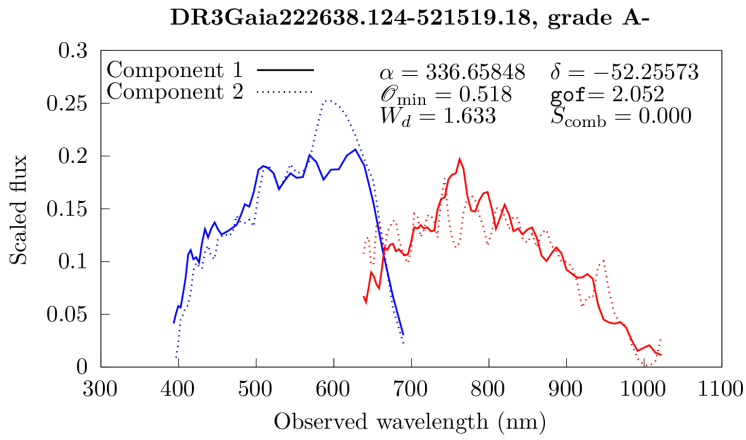


Fig. B.46. Comparison of the resampled spectra of the DR3Gaia222638.124-521519.18 multiplet (Left) and associated Dark Energy Survey image (Right) (Dey et al. 2019). Blue dots correspond to the GravLens components. Cutout size is $15.0'' \times 15.0''$, north is up, east is left.

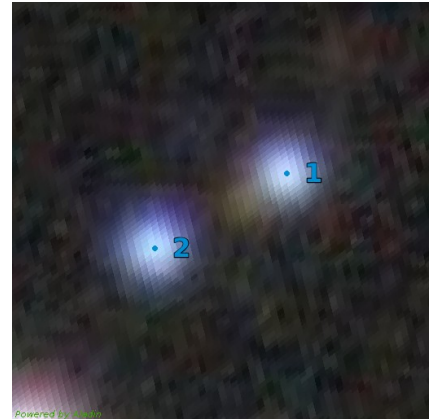
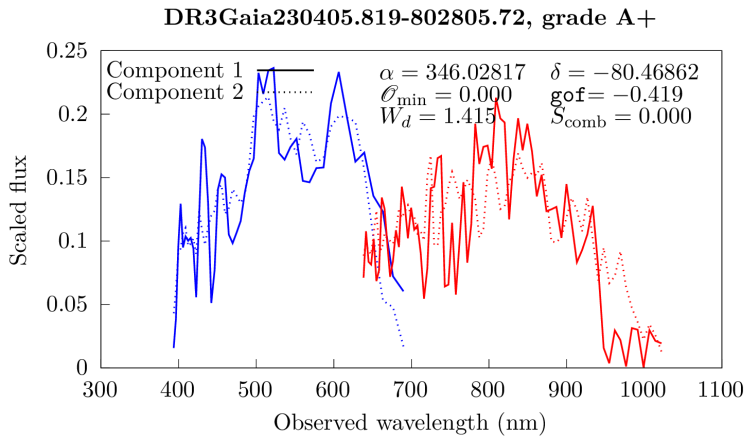


Fig. B.47. Comparison of the resampled spectra of the DR3Gaia230405.819-802805.72 multiplet (Left) and associated Dark Energy Survey image (Right) (Dey et al. 2019). Blue dots correspond to the GravLens components. Cutout size is $15.0'' \times 15.0''$, north is up, east is left.

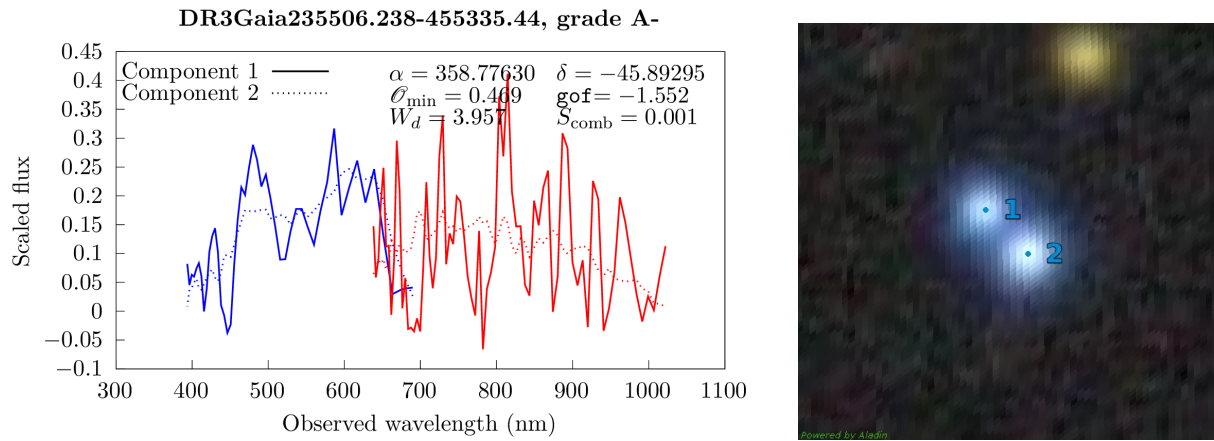


Fig. B.48. Comparison of the resampled spectra of the DR3Gaia235506.238-455335.44 multiplet (Left) and associated Dark Energy Survey image (Right) (Dey et al. 2019). Blue dots correspond to the GravLens components. Cutout size is $15.0'' \times 15.0''$, north is up, east is left.